Chaos in Stellar Dynamics

Outcomes of Binary-Single Interactions in Globular Clusters

Lucas Hellström

Lund Observatory
Lund University

2020-EXA157

Degree project of 60 higher education credits (for a degree of Master)
May 2020

Supervisor: Abbas Askar

Lund Observatory
Box 43
SE-221 00 Lund
Sweden

Abstract

Gravitational encounters between a single star and a binary system can frequently occur in the cores of dense stellar systems like globular clusters. These three-body scattering encounters can lead to a variety of outcomes since the energy of the binary components can be exchanged with the interacting single star. The outcome of these interactions strongly depend on the initial conditions of the interactions and can result in stellar collisions, exchange encounters and dissolution of binary systems. From an astrophysical point of view, these interactions can lead to the formation of exotic stellar objects and binary systems that include gravitational wave sources, X-ray binaries and blue stragglers. Such interactions involving binary systems also play an important role in preventing the core collapse of globular clusters and can influence their dynamical evolution.

The classical three-body gravitational problem has challenged researchers for many centuries and no general closed-form solution has been found. Therefore, numerical experiments are carried out to compute the outcome of these interactions. The time evolution of such a system is chaotic, this means that even small changes in the initial setup can lead to a completely different outcome. In this study, we explore how the outcome of binary-single encounters can change with the numerical method that is used to solve them. We do this by carrying out a large number of numerical scattering experiments involving combinations of stars and black holes with existing codes designed for small-N gravitational dynamics. We specifically investigate the differences in outcome that can arise from using different regularization schemes and numerical accuracies. We also briefly explore how the outcomes may be influenced by inclusion of additional physical processes such as gravitational wave radiation and tides. Such processes can dissipate energy and angular momentum during these binary-single interactions and their effects are studied in interactions involving black holes and stars.

We find that while there are differences in outcomes of individual interactions, the statistical outcome of an ensemble of these interactions is not significantly influenced by the regularization scheme. We do find that using relatively high numerical accuracy do influence the statistical outcome of the interactions and increases their computational time. However, using too low of a numerical accuracy produces larger differences and can give incorrect results. For our runs with interactions involving black holes, the inclusion of post-Newtonian terms do not result in more mergers or produce more binaries that would merge within a Hubble time. We also find that the binary black holes that do merge within a Hubble time after an encounter have properties similar to the binary black hole mergers that have been detected by gravitational wave observatories. Additionally, we find that the inclusion of tidal effects reduce the number of mergers and increase the number of temporary bound triples and the effect becomes more notable when more stars are included in the interaction.

Acknowledgements

I would first like to thank Abbas Askar for supervising this project for the past year and a half. By introducing me to this field of astronomy and providing excellent guidance throughout the whole project he made this thesis possible. I also wish to thank Alessandro Trani, Mario Spera and Johan Samsing for taking their time to discuss and helping me understand the problems and results that I found. Finally, I want to thank the people behind the Fewbody code for making the code publicly available and the team behind Tsunami for allowing me to use their code.

Popular summary: Chaos in Stellar Dynamics

Dynamics in astronomy is concerned with the causes of motion of objects in space. The dominating force which defines the motions of astronomical objects and governs their dynamical evolution is gravity. This is an attractive force that can act over a long range and influences everything that has mass or energy. In dynamical astronomy, a wide range of scales is investigated, including: how planets orbit stars, how stars move around in multiple systems and star clusters, and how galaxies dynamically evolve and interact with each other. In this project, we study dynamical interactions between stars and black holes in dense star clusters where stars are packed close together.

The magnitude of the gravitational force between two bodies depends strongly on their separation, the force becomes weaker over large distances. Therefore, relatively isolated stars like the Sun are not likely to experience strong dynamical interactions with other stars. However, in the centre of dense clusters of stars such as globular clusters, hundreds of thousands of stars can be tightly packed together in the same volume of space as between the Sun and its nearest neighbour. In these dense environments, stars interact more frequently and are likely to experience close encounters that are interesting as they can lead to the formation of exotic stellar objects like mass transferring binary systems, and it can also result in collisions between stars. These tightly packed star clusters can also contain stellar remnants like black holes which can dynamically interact with each other or with surrounding stars, which can lead to the formation of black hole binaries. These objects may merge by emitting gravitational waves, ripples in the fabric of spacetime, that can now be directly detected with ground based detectors like LIGO and Virgo. Dynamical interactions are also important for the overall evolution of globular clusters where binary systems in the centre of the cluster frequently interact with nearby stars and act as an energy source to counteract gravitational collapse of the star cluster, similar to how nuclear reactions in a star generate energy to support it from collapsing.

This project focuses on investigating the outcome of hundreds of thousands of strong dynamical encounters between a binary system and a single object, involving both stars and black holes. Such interactions can result in diverse outcomes. For instance, the binary can be slightly perturbed by the single, one of the binary components gets exchanged with the single or objects get close enough during the interaction that they merge. These 3-body interactions can be very chaotic which means that a small change in the initial parameters can affect the outcome drastically and numerical simulation tools are required to predict the outcomes of these interactions. The problem with these simulation tools is that there are a wide variety of codes that seek to solve these problems and one can obtain different outcomes for the same interactions due to differences in the numerical methods used in these codes as well as the chaotic nature of these interactions.

The primary goal of this project is to check how using different numerical methods and settings in simulation codes changes the outcome of a variety of binary-single interactions on a statistical scale. We also investigate how this may change specific properties of objects after the interaction. We find that the distribution of outcomes differs slightly between settings, but statistically the differences are negligible. We also specifically investigated how computation of such interactions could influence merger times for binary black holes. We find that the problem is complicated and whether an interaction will result in an increase or decrease in the binary merger time depends on the initial configuration, and does not strongly depend on the used simulation tools or settings.

Contents

Chapter 1

Introduction

Close encounters between stars and binaries are important for the evolution of certain stellar systems, e.g. open and globular clusters. The motion of two stars that are gravitationally interacting is relatively easy to predict since there exists a closed form analytical solution to the gravitational 2-body problem. For three bodies it is much more difficult since, 1) no closed form analytical solution exists and 2) the interactions can be very chaotic and small changes in the initial conditions may change the outcome drastically.

In this project, we investigate chaotic binary–single star interactions by systematically simulating a large number of these encounters with different regularization schemes, additional physical processes and integrator settings, such as the accuracy of the integration, to investigate how these changes may affect the statistical outcome of these kinds of interactions. Initial conditions for the binary-single encounters that are studied in this project were either manually setup to allow for better control over the input parameters or they were obtained from stellar cluster simulations carried out using the MOCCA Monte Carlo code for star cluster evolution (see section 1.5). These simulated binary-single interactions include encounters involving either three main sequence stars, three black holes, two black holes and a star, or a black hole and two stars. We also discuss the astrophysical importance of these interactions, particularly in the context of producing gravitational wave sources.

This chapter is structured as follows: section 1.1 introduces dynamics in general and dynamics in astronomy, section 1.2 introduces dense stellar systems with a focus on globular clusters in section 1.2.1, we also briefly introduce nuclear stellar clusters in section 1.2.2. In section 1.3 we discuss the dynamical processes which occur in dense stellar environments and the Newtonian equations used to solve these problems. Section 1.3.1 introduces binary-single interactions while section 1.3.2 shortly introduces binary-binary interactions. In 1.3.3 we discuss additional processes which may affect the outcome of dynamical interactions; Post-Newtonian terms (section 1.3.3.1) and Tidal effects (1.3.3.2). In section 1.4 we discuss the astrophysical importance behind this project and in 1.5 we describe the aim of the project. The structure of this thesis is explained in section 1.6.

1.1 Dynamics in astronomy

The goal of dynamics in general is finding and understanding the cause behind the relative motions of bodies, which in astronomy is, in most cases, gravity. Why exoplanets move around their host star, why stars and black holes can form binary, triple or higher hierarchical systems, how stellar clusters form and evolve and how galaxies dynamically evolve and move around in intergalactic space are some of the questions asked in dynamical *astronomy*.

Strong dynamical interactions are not the primary driver in the evolution of galaxies, instead

their evolution is driven by e.g. star formation and the feedback from stars. The evolution of clusters, on the other hand, is driven by distant 2-body encounters and strong dynamical interactions. Open clusters are relatively small irregular concentrations of 10^2 to 10^4 stars that are loosely bound system with typical densities of the order 10^1 to 10^2 $M_\odot/pc^3$ (Binney & Tremaine, 1987). Since they are not so strongly bound they can be disrupted by external processes such as interactions with giant molecular clouds and other clusters. Furthermore, they may disrupt through internal processes, such as close encounters between stars in central regions of the cluster which may accelerate a star to a velocity larger than the escape velocity of the cluster resulting in its evaporation from the cluster. In order to study dynamical interactions, we focus on old dense stellar systems where the central density is large and this increases the rate of interactions to the point where they become an important driver for the dynamical evolution of the system.

1.2 Dense stellar systems

Since the gravitational force decreases rapidly with increasing distance, stars need to get close for dynamical interactions to occur. Therefore we focus on dense stellar environments, e.g. Globular Clusters (GCs) or Nuclear Star Clusters (NSCs) since stars in their central regions (core) are much closer together and will therefore experience far more interactions over a set period than, for example, a field star like the Sun would during the same time period. Dynamical interactions can occur between stars in less dense systems and affect the evolution, such as in open clusters, however, for systems with high mass and low density, such as the discs in galaxies, the timescale for the dynamical interactions is long enough that the interactions are negligible for the evolution of the system. A star in a cluster will eventually experience either a large number of weak encounters or a smaller number stronger encounters such that the orbit of the star is vastly different from the original orbit. The timescale over which this occurs on is called *relaxation* time and is defined as the time it takes for a star to "forget" its original orbit through dynamical interactions. Stars on the edges of a cluster have a much longer encounter timescale than stars in the core, due to the lower density. Therefore the half-mass relaxation time is often used and can be approximated by (Spitzer, 1987):

$$t_{rh} \approx \frac{0.138 N^{1/2} r_h^{3/2}}{(\langle m_\star \rangle G)^{1/2} \ \ln(\gamma N)} \tag{1.1}$$

where r_h is the half-mass radius, $\langle m_\star \rangle$ is the average mass of stars and N is the total number of stars. $\ln(\gamma N)$ is the Coulomb logarithm (Spitzer, 1987; Benacquista & Downing, 2013) which describes the relative effectiveness of weak and strong interactions.

Using this relaxation time, we can divide dynamical systems into two groups: collisional and collisionless. A collisional system is a system where interactions between particles occur on relatively short timescales and are important for the dynamical evolution of the system, which occurs when the relaxation time is short with respect to the lifetime of the system. If the relaxation time is long with respect to the lifetime of the system, it is a collisionless system and the contribution from interactions between particles are negligible for the dynamical evolution of the system. The relaxation time can also be compared to the crossing time, t_c, the time it takes for an average star to cross the system, and the evolution time, t_e of the system. The typical crossing and relaxation time for open clusters, globular clusters and elliptical galaxies are shown in table 1.1 (Djorgovski, 2004).
For an open cluster we have

$$t_c \sim t_{rh} < t_e \tag{1.2}$$

where the evolution time is dependent on the properties of the cluster and is in the range of a few hundred million years. Due to this, an open cluster will dissolve on its own. For globular clusters we have

$$t_c \ll t_{rh} \ll t_e \tag{1.3}$$

	t_c [yr]	t_{rh} [yr]
Open cluster	$4 \cdot 10^6$	$8 \cdot 10^6$
Globular cluster	$0.4 \cdot 10^6$	$4 \cdot 10^8$
Elliptical galaxy	$2 \cdot 10^6$	10^{17}

Table 1.1: Typical timescales for open clusters, globular clusters and elliptical galaxies (Djorgovski, 2004).

where the evolution time is approximately 10^{10} years and several different dynamical evolution states can be present. Now for an elliptical galaxy we have

$$t_c \ll t_{rh} \sim t_e \tag{1.4}$$

where the evolution time is almost equal to the relaxation time and far longer than a Hubble time. Thus the dynamical evolution is not driven by 2-body relaxation.

1.2.1 Globular clusters

An example of a dense collisional stellar environment is globular clusters (GCs). These are spherical collections of 10^4 to 10^6 stars with central densities of up to $\sim 10^5$ stars/pc^3. This can be compared to the stellar density in the Solar neighbourhood which is estimated to be $\sim 10^{-1}$ stars/pc^3. They are found spherically distributed in the halos of galaxies and have been found in almost all large galaxies surveyed. There are about 150-200 known GCs in the Milky Way (Harris, 1996; Chaisson & McMillan, 2011) most of which have a high relative velocity to the Sun since they do not orbit with the galactic disc. There are however, a small number of so-called disc globulars which have orbital properties similar to that of the disc. Typically, GCs contain metal poor stars and are estimated to be 10 to 13 billion years old (Krauss & Chaboyer, 2003).

Due to the relatively short relaxation time of GCs, they can be found in several different dynamical states which is useful when studying their evolution. A GC is supported by the velocity dispersion of stars counteracting gravitational collapse. The structural evolution of GCs begin with interactions between bodies producing spatial granularities due to the exchange of energy which leads to a local change in the magnitude of the velocities of stars. These fluctuations may lead to the ejection of stars from the cluster, which is called evaporation. Since these encounters try to equalise kinetic energy, a more massive star often losses energy after an encounter with a lighter star and sinks to the center of the cluster. On the other hand, the lighter star acquires energy and moves outwards, creating a mass segregation where heavy stars are most often found in the core of the cluster while lighter stars are found in the outer regions.

As stars evaporate from the core to the halo, the GC core loses both mass and kinetic energy and since faster stars are more easily ejected from the core, the velocity dispersion also decreases. Due to this, the core contracts and since the heat capacity in a gravitationally dominated system is negative this leads to an increase in kinetic energy of the stars. This increase in kinetic energy and the higher density means that the rate of encounters increases and the stars become dynamically hotter and the rate of evaporation increases. As the rate of evaporation increases, the core further contracts which leads to a runaway collapse, schematically illustrated in figure 1.1. However, if we investigate the GCs in the Milky Way today, we find a mixture of collapsed and non-collapsed clusters. This is also true for the extragalactic GCs that have been surveyed, which means that there must be some process which counteracts the gravitational pull and stops the core collapse. One process that halts core collapse is the dynamical formation of binary systems (Aarseth, 1971; Heggie & Hut, 2003) which behave like batteries, this is discussed more in section 1.3.1.

Another possible process to delay or stop the core collapse of GCs is mass loss by stellar winds

and supernovae which removes mass from the system without changing the kinetic energy of the other stars. However, this is only possible if the massive star evolution timescale is similar to the core collapse timescale (Lamers et al., 2010).

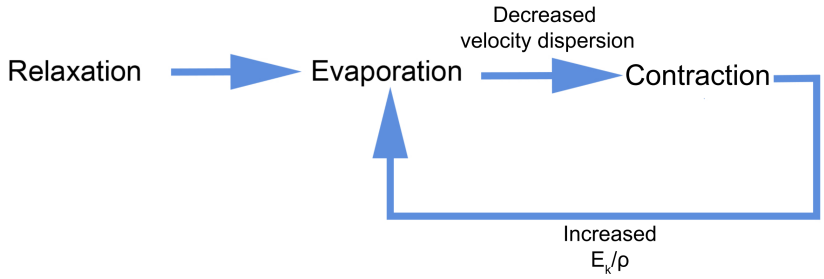

Figure 1.1: Diagram of the runaway core collapse in a globular cluster

The retention of black holes in GCs is uncertain to this day and even though we have indirectly observed candidate black holes in GCs (Strader et al., 2012; Giesers et al., 2018) their exact number and retention fraction are unknown. The reason for this uncertainty is linked to the question of whether black holes receive a high kick at birth (natal kick). The most massive stars in GCs should have evolved to form black holes. However, if the black hole received a natal kick with a velocity that was higher than the escape velocity of the cluster then it would escape the GC. When a massive star in its final stages of evolution undergoes a supernova explosion and collapses into a compact object then the newly formed compact object can receive a natal kick. Observations of proper motions of pulsars in our Galaxy indicate that their natal kick velocities are typically in the range of 200-500 km/s but velocities over 1000 km/s have been observed (Cordes et al., 1993; Hansen & Phinney, 1997; Hobbs et al., 2005; Faucher-Giguere & Kaspi, 2006). The origin of this kick is not completely understood but theories point towards asymmetries in the supernova ejecta or neutrino emission as being the cause of the kick (Janka, 2013; Wongwathanarat et al., 2013; Janka, 2017). If the natal kicks of black holes have the same magnitude as neutron stars (Repetto et al., 2012) then most of them would be ejected out of their host cluster at birth. However, it has been argued that black hole natal kicks could be lower due to fallback of material during a supernova explosion (Fryer et al., 2012; Belczynski et al., 2016; Chan et al., 2018) or by direct collapse of a star into a black hole without a supernova (Fryer, 1999; Adams et al., 2017).

By assuming that black holes do not receive a substantial natal kick and are retained in the cluster after birth, it is expected that black holes would segregate to the core of the cluster due to dynamical friction. Since the core of a GC is a very dense environment, the objects in it are likely to dynamically interact. These interactions can lead to the ejection of the black holes from the cluster or harden binaries which may lead to mergers and over time, the cluster is depleted of black holes (Kulkarni et al., 1993; Sigurdsson & Hernquist, 1993; Portegies Zwart & McMillan, 2000). The number of black holes that are retained after a given time depends strongly on the initial conditions of the cluster (Breen & Heggie, 2013a,b) and has been investigated using numerical simulations (Morscher et al., 2013; Wang et al., 2016; Askar et al., 2018; Arca Sedda et al., 2018; Hong et al., 2018; Kremer et al., 2019).

1.2.2 Nuclear star clusters

Nuclear star clusters (NSCs) are dense stellar environments located close to the center of galaxies. Most NSCs contain a mix of old and young stars and show signs of star formation, however their origin is unclear. Two scenarios are often discussed; the NSCs are built up by consecutive infall of stellar clusters (Tremaine et al., 1975; Antonini, 2013) or there exists some form of continuous in-situ star formation (Loose et al., 1982; Aharon & Perets, 2015). NSCs are often found in galaxies

where the stellar mass is in the range $M_\star < 10^{10}$ $M_\odot$ (Neumayer et al., 2020), and can exist alone or together with a supermassive black hole (SMBH) e.g. in the Milky Way (MW), however in high-mass galaxies, where the stellar mass is $M_\star > 10^{10} - 10^{11}$ $M_\odot$ there is usually only a SMBH with no clear observations of NSCs.

NSCs can be both collisional and collisionless systems, depending on the existence of a SMBH and the mass of it. Without the presence of a SMBH, a NSC is collisional however, in the presence of a SMBH the cluster is only collisional outside the influence radius of the SMBH (Antonini et al., 2012; Mapelli, 2017b). This is different from other star clusters without a single massive object where two-body relaxation is the most important dynamical process since in NSCs other effects, such as the influence from a SMBH, are also important. The central velocity dispersion is much higher in NSCs, where it is a few hundred km/s, than in GCs, where it is around 10 km/s. Because of this higher velocity dispersion, gravitational focusing has a lesser effect on the dynamical interactions in NSCs as compared to GCs (Davies, 2013).

As previously mentioned, the MW hosts a NSC around its SMBH and even though NSCs are seen in a significant fraction of galaxies, they are very difficult to observe in detail and there are only a few cases where a NSC has been confirmed in the presence of a SMBH Schödel et al. (2008, 2009). The NSC in the Milky Way is an interesting case since it is possible to resolve individual stars which makes it possible to determine their orbital path, proper motion and mass (Shahzamanian et al., 2019).

1.3 Dynamical processes

Dynamical processes are most important in dense environments since the timescale for these close encounters is low enough for them to be important for the dynamical evolution of the system. These encounters are generally very chaotic and small changes in the initial parameters can drastically change the outcome of the interaction. The dominating force in these encounters is the gravitational force:

$$F = G\frac{m_1 m_2}{r^2} \tag{1.5}$$

where G is the gravitational constant, $m_{1,2}$ is the mass of object 1 and 2 respectively and r is the distance between the objects. For a star in a cluster, i, the total acceleration from all other objects, j, in the cluster is

$$m_i \frac{\mathrm{d}^2\mathbf{r}_i}{\mathrm{d}t^2} = -\sum_{\substack{j=1 \\ j\neq i}}^{N} \frac{G m_i m_j (\mathbf{r}_j - \mathbf{r}_i)}{|\mathbf{r}_j - \mathbf{r}_i|^3} \tag{1.6}$$

where N is the total number of objects in the cluster and $r_j - r_i$ is the distance between stars i and j. To introduce the direction of the force, an additional term in the form of the unit vector from i towards j is included in the equation. Dynamical interactions are important for the evolution of collisional system as previously discussed but they can also be important for the formation of exotic stellar objects, e.g. black hole binaries, blue stragglers, X-ray binaries, cataclysmic variables and millisecond pulsars (Davies, 2002), see section 1.4.

The encounter timescale, τ_{enc}, for any given star in a system with low velocity dispersion is given by (Davies, 2013):

$$\tau_{\mathrm{enc}} = 7 \cdot 10^{10} \text{ year} \left(\frac{10^5 \text{ pc}^{-3}}{n}\right) \left(\frac{v_\infty}{10 \text{ km/s}}\right) \left(\frac{R_\odot}{R_{\mathrm{min}}}\right) \left(\frac{M_\odot}{m}\right) \tag{1.7}$$

where n is the number density of single stars of mass m, v_∞ is the relative velocity at infinite separation and R_{min} is the minimum separation between the objects. For an interaction between two single objects, R_{min} is typically relatively small, however, for a binary-single interaction, R_{min} is roughly equal to the semi-major axis of the binary which can greatly increase the encounter rate.

Since these encounters generally cannot be observed and no analytical solution exists for encounters with more than 2 objects we have to rely on numerical simulations. A simple and efficient approach is the N-body simulation, where each object is represented as a particle and all forces between the particles are calculated, this will be discussed in further detail in chapter 2.

1.3.1 Binary-Single interactions

In GCs, the interaction between binaries and single stars or other binaries are important for reversing the process of core collapse, however, these interactions are chaotic and no analytical solution exists to predict the outcomes of these interactions. A binary system has an internal energy (Binney & Tremaine, 1987; Mapelli, 2017a):

$$E_{int} = \frac{1}{2}\mu v^2 - \frac{Gm_1m_2}{r} \tag{1.8}$$

where m_1 and m_2 is the mass of the binary objects, $\mu = m_1m_2/(m_1 + m_2)$ is the reduced mass and r and v are the relative separation and velocity. For a bound system this internal energy is negative and a larger negative value means that the binary is more bound. This energy can be exchanged with other stars such as single stars via close encounters. In a close encounter, the transfer of energy can occur in two ways; either the binary transfers some of its internal energy to the single star, causing the binary to become more bound and the single acquires kinetic energy. The single star may also transfer energy to the binary causing the binary to become less bound or even ionized/unbound if $E_{int} > 0$ after the encounter and the single star loses kinetic energy. In order to ionize the binary, the single star must have a velocity at infinity, v_∞, the velocity of the single star when it is far away from the binary, greater than the critical velocity, v_c, which for a binary-single interaction is:

$$v_c = \left(\frac{Gm_1m_2(m_1 + m_2 + m_3)}{m_3(m_1 + m_2)\, a}\right)^{1/2} \tag{1.9}$$

Where the subscript 1 and 2 corresponds to the binary and 3 to the single (Hut & Bahcall, 1983).

To determine if a binary will lose or acquire energy we classify binaries as hard or soft binaries. A binary with semi-major axis, a, and masses m_1, m_2 is said to be hard if

$$\frac{Gm_1m_2}{2a} > \frac{1}{2}\langle m\rangle\sigma^2 \tag{1.10}$$

and soft if

$$\frac{Gm_1m_2}{2a} < \frac{1}{2}\langle m\rangle\sigma^2 \tag{1.11}$$

where $\langle m\rangle$ is the average stellar mass in the system and σ is the velocity dispersion. On average this leads to hard binaries getting harder while soft binaries gets softer, this is often referred to as Heggie-Hills law (Heggie, 1975; Hills, 1975; Binney & Tremaine, 1987) .

The likelihood of a 3-body interaction to occur can be expressed as a cross-section (Mapelli, 2017a):

$$\Sigma = \pi b_{max}^2 \tag{1.12}$$

where b_{max} is the maximum impact parameter for a non-zero energy exchange between a binary and a single to occur. This can be seen as a cylinder with radius b_{max} that is expanding with time along the binary's line of motion, see figure 1.2 where a binary with velocity V is illustrated. The cross-section is the area of the base of this cylinder. Without gravity the maximum impact parameter would simply be the separation of the binary stars, however, if the total mass of the binary is greater than that of the single star, the trajectory of the single will be deflected when it approaches. This is called gravitational focusing and increases the cross-section for 3-body

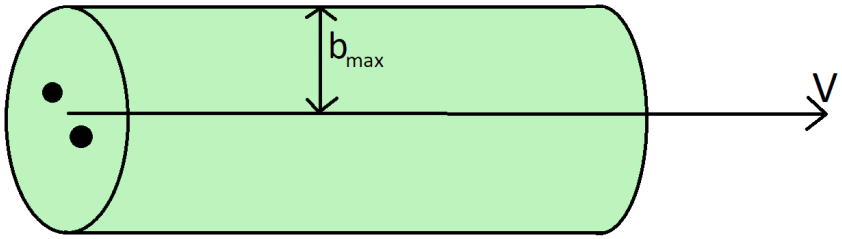

Figure 1.2: Illustration of the cross-section of a binary

encounters significantly and changes the cross section equation to:

$$\Sigma = \pi b_{max}^2 \left(1 + \frac{v^2}{v_\infty^2}\right) \tag{1.13}$$

where v is the relative velocity of the objects at closest approach and v_∞ is the relative velocity between the stars when they are at infinite separation, i.e. before any energy has been exchanged.

The outcome of a binary-single interaction can be any of the following:

- Flyby where there is some energy exchange but the initial configuration is conserved.
- Exchange where one of the initial binary stars is replaced by the initial single. This is favourable if the mass of the initial single is higher than the mass of any of the initial binary stars.
- Ionization (binary dissolution) which can occur when v_∞ is higher than v_c, see equation 1.9.
- Binary containing a two-star merger, here two of the stars merge and the merger product forms a bound binary with the remaining star.
- Two-star merger and a single, same case as above but the merger product does not form a bound binary with the remaining star.
- Stable hierarchical triple, although rare, it is possible to form a metastable triple which will eventually dissolve but the timescale for this is long. Triples are, however, generally easy to dissolve via encounters with other stars.
- Three-star merger where all three stars merge to form a single object.

1.3.2 Binary-Binary interactions

Interactions between two binary systems are, similarly to binary-single interactions, highly chaotic and the outcome can change drastically if the initial input is slightly changed, it is therefore often very hard to predict the outcome of a binary-binary interaction. If the two binaries pass at sufficient distance they will see each other as a single object and the same hardening or softening as discussed in the previous section can occur. If the binaries interact on a short distance there are many different outcomes; if one of the binaries is harder than the other, it may "steal" one of the stars from the softer binary and form a hierarchical triple. One of the binaries may also be ionized by the other, for this to occur v_∞ has to be larger than the critical velocity as in the binary-single case, however, for a binary-binary interaction the v_c is given by:

$$v_c = \left[\frac{G}{\mu}\left(\frac{m_{00}m_{01}}{a_0} + \frac{m_{10}m_{11}}{a_1}\right)\right]^{1/2} \tag{1.14}$$

where subscript 00 corresponds to the first object in the first binary, 01 to the second object in the first binary, 10 to the first object in the second binary and 11 to the second object in the second binary. $a_{0,1}$ is the semi-major axis of the first and second binary respectively and μ is the reduced mass:

$$\mu = \frac{(m_{00} + m_{01})(m_{10} + m_{11})}{m_{00} + m_{01} + m_{10} + m_{11}} \tag{1.15}$$

There exists a large number of different outcomes which will not be discussed here, see e.g. Fregeau et al. (2004) or Benacquista (2013).

1.3.3 Additional Processes

In addition to the Newtonian equation of motion there exists other effects which needs to be taken into consideration when looking at certain dynamical interactions. For most cases, the Newtonian approximation works well, however, for a few cases there are additional processes which may change the outcome of the interaction; Post-Newtonian dynamics is needed when relativistic effects are non-negligible and general relativity is not the preferred way to go. This is especially important when black holes are included. Tidal effects are also important for dynamical interactions, especially for interactions including stars which will get stretched by the tidal forces from the other bodies in the interaction. Both of these effects introduce dissipation of energy and are discussed in the following sections.

1.3.3.1 Post-Newtonian dynamics

Around massive objects, spacetime is curved and our Newtonian equations of motion are not enough to explain the motion of bodies traveling very close to them (e.g. precession of the perihelion of Mercury). This can be solved with general relativity, however, this is usually very complicated and hard to implement. Due to this, extensions to the Newtonian equations have been developed to account for the relativistic effects (Fackerell, 1968). These extensions, called Post-Newtonian (PN) terms, are named such that every PN followed by an integer, e.g. PN 1,2,3 are conservative terms, for example, PN 1 and 2 relate to the perihelion shift that we can see in Mercury's orbit. The PN terms followed by half an integer, e.g. PN 2.5, 3.5 are dissipative terms and relate to, for example, the emission of energy in gravitational waves or emission of linear momentum in the unequal mass case. The PN 3.5 term is also related to the Spin-Spin and Spin-Orbit-Couplings (Spurzem, 2007).

Spurzem (2007) give an for the total acceleration of an object including the first 2.5 PN terms:

$$a = a_0 + c^{-2}a_2 + c^{-4}a_4 + c^{-5}a_5 + \mathcal{O}(c^{-6}) \tag{1.16}$$

where c is the speed of light in a vacuum, a is the total acceleration, a_0 is the Newtonian component, $c^{-2}a_2$ and $c^{-4}a_4$ is the first and second PN term which relates to the periastron shift and $c^{-5}a_5$ is the 2.5 PN term which relates to the emission of gravitational waves. The equations for a_n are not included here as they are extensive and complicated, for more information and the complete equation for a_n see e.g. Blanchet (2014). The inclusion of relativistic corrections are important during interactions involving black holes and may lead to different outcomes than if these effects are neglected (Samsing, 2018; Rodriguez et al., 2018).

1.3.3.2 Tidal effects

When a star passes close to a massive object it can be partially or fully disrupted (Perets et al., 2016) and if the massive object is massive enough, e.g. a SMBH, the star may experience spaghettification and form an accretion disk around the massive object (Vinkó et al., 2014). For less massive objects in close encounters, the stars are most likely not fully tidally disrupted and instead lose orbital energy due to the tidal effects which can lead to formation of binaries (Press & Teukolsky, 1977; Lee & Ostriker, 1993). These tidal captures may be important for the formation of exotic binary

systems in GCs and may influence its evolution. However, tides are poorly understood and generally accounting for them can be computationally heavy which makes large scale surveys not possible at the present time (Samsing et al., 2018).

1.4 Astrophysical importance

Proper treatment of binary-single interactions are important for the formation of certain exotic objects such as x-ray binaries, relativistic binaries, blue stragglers, cataclysmic variables and millisecond pulsars (Davies, 2002). Certain exotic objects seem to be over-represented in GCs compared to the field, in particular x-ray binaries (Pooley, 2010) and millisecond pulsars (Ransom, 2008). Blue stragglers cannot be explained by single star evolution and require interactions with additional objects and/or a collision with another star to explain their population.

Other interesting objects that are observed or can theoretically exist in GCs are compact object binaries. These binaries consists of two very compact objects such as two black holes, two neutron stars, two white dwarfs or a mix of two different compact objects. These objects may have formed when their progenitor stars evolved, however, they may also have been formed from dynamical interactions. Since these objects are massive compared to the luminous stars in the cluster they will be segregated to the center of the cluster where the high density will lead to a large number of interactions with other single and binary objects which may harden the binary and increase its eccentricity. If the orbit becomes very eccentric the objects may lose orbital energy from emitting gravitational wave (GW) radiation at the closest approach, this loss of energy may eventually lead to a merger between the objects (Samsing, 2018; Rodriguez et al., 2018). GWs from merging black holes or neutron stars have been detected by the ground based detectors LIGO (Laser Interferometer Gravitational-Wave Observatory) and Virgo (Abbott et al., 2016a,b; Abbott et al., 2019) and in the future they may also be detected by space based detectors such as LISA (Amaro-Seoane et al., 2013; Sesana, 2016; Samsing et al., 2018b; Sesana et al., 2019). The astrophysical origin of these GW sources is currently unknown and it is possible to form such merging binary systems from both isolated binary evolution or through dynamical channels in dense environments. Dynamical interactions in a dense stellar environment, such as GCs, can harden existing compact object binaries or dynamically create eccentric binaries. Therefore, these dense environments could be potential sites to form such GW sources (Portegies Zwart & McMillan, 2000; Downing et al., 2010; Rodriguez et al., 2016; Askar et al., 2017; Hong et al., 2018).

As discussed in section 1.2.1, the long-term evolution of GCs depends mainly on distant dynamical interactions between stars. Additionally, close interactions involving binary systems are also important in generating energy and forming exotic stellar systems in GCs. Therefore, a proper treatment for such encounters is needed when evolving realistic stellar clusters. However, current GC simulations, such as MOCCA Monte Carlo simulations (Giersz et al., 2013), do not account for Post-Newtonian terms or tidal effects when solving these interactions. The inclusion of these additional processes may change the outcomes of certain individual interactions, however, if they change the outcomes on a statistical scale is uncertain.

1.5 Aim of the project

The main aim of this project is to investigate how the statistical outcome of binary-single encounters depends on the way these interactions are numerically solved and whether inclusion of additional physical processes such as those discussed in Section 1.3.3 can significantly change outcome of these interactions.

Simulating the long-term evolution of a GC is a computationally expensive task. The traditional approach is using a pure N-body code which while very accurate and reliable, is slow since the computation time is of the order $O\left(N^2\right)$ (where N is the number of stars in the cluster). Therefore,

evolving a GC with a million stars up to a Hubble time can take several months up to a year (Wang et al., 2016). To speed up these simulations different approaches have been developed. An example of this are simulation codes based on Hénon's Monte Carlo method (Hénon, 1971b,a) such as the MOnte Carlo Cluster simulAtor (MOCCA) (Hypki & Giersz, 2013) or the Cluster Monte Carlo (CMC) (Pattabiraman et al., 2013) codes. The MOCCA code is able to simulate the evolution of a realistic GC up to a Hubble time within a week while still showing good agreement wtih direct N-body results (Giersz et al., 2013; Wang et al., 2016). To solve binary-single and binary-binary interactions, MOCCA and CMC codes uses the Fewbody code by Fregeau et al. (2004) (see section 2.3). The choice of integrator scheme or kind of regularization used can change the outcome of such individual interactions, however, whether the outcomes change on a statistical scale is not certain. The accuracy of the integrator, i.e. the number of digits saved for each variable can also have an impact on the outcomes. Boekholt & Portegies Zwart (2014) and Portegies Zwart & Boekholt (2014) predict that on a large enough scale where the energy conservation is better than 10%, the accuracy does not matter. This project aims to investigate how a change in integration scheme or increase/decrease of accuracy will affect the outcomes of binary-single interactions on a statistical scale.

In addition to this, the Fewbody code does not include additional processes such as PN terms or tidal effects when computing the outcomes of binary-single and binary-binary interactions. These additional processes are added in the standalone extension to Fewbody called Tsunami by Trani et al. (2016) and may change the outcomes of certain interactions, however, if they change the outcomes on a statistical scale is uncertain and will be investigated for binary-single interactions in this project.

This can be summarised to: Which regularization methods, additional processes and how low/high integrator accuracy should be included/used when solving binary-single interactions to accurately simulate the evolution of dense systems where these chaotic interactions are the main driver, such as in globular clusters?

1.6 Structure of the thesis

In this chapter, the astrophysical context and main aims of this work are provided. The rest of the thesis is organized as follows:

- In chapter 2, we describe how binary-singe encounters are numerically integrated and describe the simulation codes that were used to carry out this study in sections 2.3 and 2.4. This includes a brief introduction to the regularization schemes they use and how additional physical processes are implemented within them. In section 2.5, we explain the initial conditions for the different data sets that we simulated.

- In chapter 3, we show the results for outcomes of the different data sets (sections 3.3,3.4,3.5) and discuss the similarities and differences between using different regularization schemes, numerical accuracies and physical processes. In section 3.1, we show examples of a couple of astrophysically interesting interactions and in section 3.2, we compare results from our simulation codes with a previous study.

- In chapter 4, we summarize and discuss the key results presented in chapter 3. We also briefly discuss the influence of accuracy on our results for computation time in section 4.2.1 and discuss the results of binary-single interactions involving black holes and their implications for gravitational wave defections in section 4.3.3.

- In chapter 5, we briefly summarize the thesis and provide the main conclusions of this work.

Chapter 2

Method: Simulation techniques, codes and setups

This chapter describes the simulation codes used in the project as well as initial conditions for different data sets that were simulated. Section 2.1 introduces integrating the Newtonian equation for a gravitationally dominated system to obtain the dynamical evolution of the system, this section also shortly describes a few common integration methods. In section 2.2 we describe the need for regularization when dealing with close encounters between objects. The two codes that are used in this project to simulate the binary-single interactions are discussed in the sections; The N-body code Fewbody in section 2.3 where we also introduce Kustaanheimo-Stiefel regularization (section 2.3.1). The standalone extension to Fewbody, Tsunami, is described in section 2.4 where we also discuss Algorithmic regularization (section 2.4.1), Post-Newtonian dynamics (section 2.4.2) and tidal effects (section 2.4.3). In section 2.5 and its subsections we describe the different data sets that we have created or extracted from the MOCCA Survey Database I (Askar et al., 2017). In section 2.6 we describe the framework created to run Fewbody and Tsunami automatically with different data sets and settings, save the results and extract the relevant results.

2.1 Integration

The N-body problem, where N relates to the number of bodies in the system, can be simple or complicated depending on the value of N. For $N = 1$, $N = 2$ and $N \to \infty$ analytical solutions exists but for all N in between, computer simulations are required. For astronomy problems the dominating force is gravity and as such we use the equation

$$\mathbf{a}_i(t) = -\sum_{j \neq i}^{N} \frac{G m_j (\mathbf{r}_j - \mathbf{r}_i)}{|\mathbf{r}_j - \mathbf{r}_i|^3} \tag{2.1}$$

to calculate the acceleration on a body, i, caused by the other bodies in the system, j. Where m_j is the mass of the other body and $r_{i,j}$ are the positions of the bodies. To calculate the position and velocity of a body after a certain time, Δt, the following equations are used

$$\mathbf{r}_i(t + \Delta t) = \mathbf{r}_i(t) + \Delta t \mathbf{v}_i(t) \tag{2.2}$$

$$\mathbf{v}_i(t + \Delta t) = \mathbf{v}_i(t) + \Delta t \mathbf{a}_i(t) \tag{2.3}$$

These equations are only dependent on mass, position and velocity and should not be too tricky to solve, however, as the number of objects in the system increases the number of calculations

required at each time step increases as N^2 which can quickly lead to unreasonable computation times. In addition to this, the choice of time step (Δt) can be tricky since it needs to be small enough such that the objects does not move too far in relation to their separation in one time step but large enough such that not too many unnecessary steps are taken which increases round-off errors.

The most simple integration method is called the Euler method where the change in a parameter is applied to the value of the parameter for every time step. For example a 1-D problem with starting position y_0 and change in position y', will, after one time step, have the position $y_1 = y_0 + y'$ and so on. This is easy to use and implement but is not commonly used due to the very small time steps required to obtain a good accuracy.

The Runge-Kutta method (Runge, 1895; Kutta, 1901) is another integration method with much higher accuracy than the Euler method which takes a number of increments, n, in between every time step. The number of increments can be chosen depending on the required accuracy of the problem. For a 1-D problem with $y' = f(t, y)$, where $f(t, y)$ is some function that is dependent on time and position y, the initial position $y(t_0) = y_0$ and time step h. A common number of increments is 4 since it is fairly accurate, easy to implement and does not introduce an unnecessary amount of calculations, with $n = 4$ the first step is given by

$$y_1 = y_0 + \frac{1}{6}(k_1 + 2k_2 + 2k_3 + k_4) \tag{2.4}$$

where k is given by

$$\begin{aligned} k_1 &= hf(t_0, y_0) \\ k_2 &= hf(t_0 + h/2, y_0 + k_1/2) \\ k_3 &= hf(t_0 + h/2, y_0 + k_2/2) \\ k_4 &= hf(t_0 + h, y_0 + k_3) \end{aligned} \tag{2.5}$$

This is the 4th order Runge-Kutta method which can be expanded to higher order by increasing n which in turn increases the number of different k terms.

Another commonly used 2nd order integration method is the Leapfrog algorithm where the position and velocity is not updated at the same time step but at interleaved time points, e.g. we start at $t = 0$, at $t = 1/2$ the velocity of the particles are updated according to some function. Then at $t = 1$ the positions are updated with the previously obtained velocities. This is more accurate than the Euler method while requiring the same number of calculations per time step. The leapfrog algorithm can also be expanded to higher order by using Yoshida coefficients (Yoshida, 1990).

2.2 Regularization

Since the gravitational force between objects is proportional to the inverse of the distance squared it disappears quickly over longer distance, this also means that it increases quickly for shorter distances. If the distance between two objects becomes very small this force can be unreasonably large since as the distance $r \to 0$ the force $F_{grav} \to \infty$. This is a problem for codes dealing with close encounters since the time steps required to resolve these interactions becomes smaller to the point where the integration is barely moving forward. This problem can be solved via e.g. smoothing (Merritt, 1996) where a smoothing factor is added to the denominator which solves the problem of the force reaching ∞ but may instead increase the error of the calculation. Another solution to this problem is to use some form of regularization where the equations are rewritten to better suit the problem (Heggie, 1974; Mapelli, 2017c). The codes used in this project makes use of Kustaanheimo-Stiefel regularization (see section 2.3.1) and Algorithmic regularization (see section 2.4.1).

2.3 The Fewbody code

Fewbody is a N-body code by Fregeau et al. (2004) which uses an eighth-order Runge-Kutta Dormand-Prince integrator with an adaptive time step to simulate dynamical encounters e.g. binary-single or binary-binary interactions. In order to speed up integration times Fewbody is able to switch between analytical and numerical methods. This is done by ordering the N-body system in a hierarchical tree where if the forces on a bound system from the other objects in the simulation is low enough, the bound system can be replaced by a parent node and treated analytically. For more details see Fregeau et al. (2004). In order to decide if a hierarchy can be treated analytically we first consider the relative force of the binary at apocentre, calculated by

$$F_{rel} = \frac{Gm_0m_1}{[a(1+e)]^2} \tag{2.6}$$

where m_0 and m_1 are the masses of the members of the binary and a and e are the semi-major axis and eccentricity of the binary. This is related to the tidal forces induced by the other objects in the simulation, calculated by

$$F_{tid} = \sum_i \frac{2G(m_0+m_1)m_i}{r_i^3} a(1+e) \tag{2.7}$$

If the ratio between these forces are less than a given tidal tolerance, δ, i.e.

$$\frac{F_{tid}}{F_{rel}} < \delta \tag{2.8}$$

the hierarchy can be treated analytically. A higher value on the tidal tolerance allows the code to treat the hierarchy analytically more frequently but decreases the energy accuracy, on the other hand, a lower value yields better energy conservation but increases the computation time. Fewbody is able to handle collisions between stars although in a fairly simplistic way; stars are treated as spheres equal to the given radii and whenever two stars overlap they are instantly merged with no loss in mass and linear angular momentum conserved, this is called the sticky star approximation. The radius of the merger product is given by

$$R_{merger} = f_{exp}(R_1 + R_2) \tag{2.9}$$

where f_{exp} is an expansion factor which SPH simulations have shown should be in between 2 and 30 (Lombardi et al., 2003).

Fewbody is easy to use and does not require the user to specify any angles of how the system is oriented. Instead the semi-major axis and eccentricity is specified and the orientation of the system is randomised using the four angles $\theta = \cos^{-1}(2X-1)$, $\phi = 2\pi X$, $\omega = 2\pi X$ and $\eta = 2\pi X$ where θ is the polar angle, ϕ is the azimuthal angle, ω is the angle between the binary Runge-Lenz vector and some fiducial vector perpendicular to the angular momentum vector, η is the mean anomaly and X is some value between 0 and 1, chosen randomly from a uniform distribution, see figure 2.1 for an illustration of the angle that can be used to describe the orientation of a binary star system.

The number of digits saved for each parameter is called accuracy and can change the outcome if chosen poorly. If the accuracy is set too low, small amounts of information will be lost in every time step, these small losses will accumulate over several time steps and introduce inaccurate results. A too high accuracy, on the other hand, will introduce unnecessary computation time. Fewbody uses two parameters for the accuracy; Absolute accuracy given in absolute units (km/s, AU etc.) and relative accuracy (unit less, accuracy relative to the calculated value). On the scale of individual interactions the accuracy may change the outcome, however, on a larger statistical scale, it has

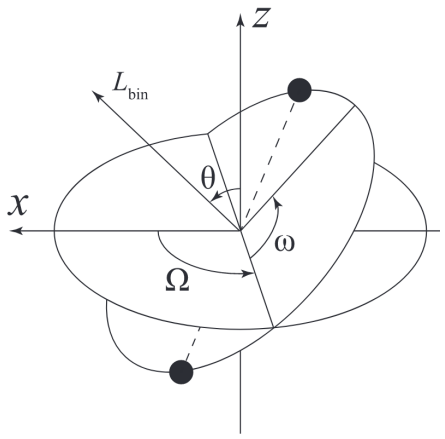

Figure 2.1: Illustration of the angles used to describe the orientation of a binary star system where θ is the inclination, Ω is the longitude of the ascending node, ω is the argument of periapsis and L_{bin} is the angular momentum vector.
Source: Rasskazov & Merritt (2017)

been postulated that as long as the energy conservation is better than 10% for all encounters, the accuracy should not make a difference to the statistical outcome (Portegies Zwart & Boekholt, 2014; Boekholt & Portegies Zwart, 2014).

2.3.1 Kustaanheimo-Stiefel regularization

Fewbody includes the option to use the Kustaanheimo-Stiefel (KS) transform to regularise the encounter (Kustaanheimo & Stiefel, 1965). The KS transform is a coordinate transformation designed to remove singularities from the equations of motion by turning the gravitational problem into a harmonic oscillator which is done by introducing a fourth dimension (Saha, 2009). This is very useful for close encounters since the forces between bodies can become very large for small separations which drives down the time step and slows down the integration.

2.4 The Tsunami code

Tsunami is a standalone extension to Fewbody by Trani et al. (2016); Trani et al. (2019), in addition to the pure N-body code of Fewbody, Tsunami introduces the option to use an algorithmic regularization chain (ARChain) instead of KS regularization. Tsunami also includes PN terms up to the 2.5 term as well as energy loses through tidal forces.

2.4.1 Algorithmic regularization

Another form of regularization is the so called Algorithmic regularization (AR) which introduces a Hamiltonian function in the extended phase space. This form of regularization is useful since a logarithmic Hamiltonian leapfrog function can be used without any kind of coordinate transformation (Mikkola & Aarseth, 1993; Mikkola & Tanikawa, 1999). In order to improve AR, work has been done on a "chain concept" where every particle in the system is ordered by distance to the particle under consideration and then the system is integrated along this chain, see fig 2.2 for an illustration of this chain. This chain helps to reduce round off error which normally accumulates and may lead to incorrect results.

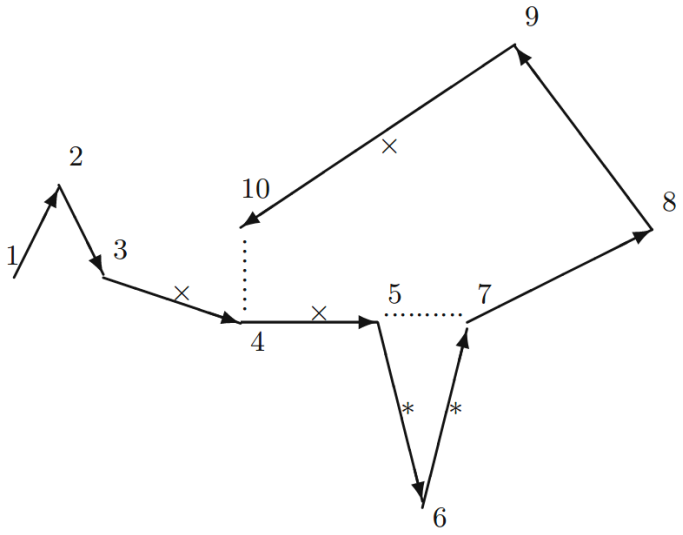

Figure 2.2: Illustration of the chain method used in the ARChain, here for 10 particles. Source: Mikkola (2008)

2.4.2 Post-Newtonian dynamics

As discussed in section 1.3.3.1, Post-Newtonian (PN) terms are used to include relativistic effects without using general relativity. Tsunami includes the option to use the first 3 PN terms (1,2 and 2.5) which may be especially important when considering heavy and dense objects, e.g. neutron stars or black holes. Thanks to the development of the PN terms, effects such as gravitational wave emission are not difficult to implement into a N-body code.

2.4.3 Tidal effects

The addition of tidal effects are much more complicated than that of gravitational wave emission since our understanding of stellar structure and the mechanisms behind how tides are excited and dissipated are limited. Tidal effects are also quite computationally heavy and thus large scale studies are not yet possible. For more information about tides see section 1.3.3.2

Energy loss through tidal effects are added to Tsunami with a drag force model (Samsing et al., 2018) which works by introducing a drag force that act against the relative motion of the objects in the system. This drag force is simply calculated by

$$\mathbf{F} = -\mathcal{E}\frac{v}{\overline{\boldsymbol{r}}^n} \times \frac{\overline{\boldsymbol{v}}}{v} \tag{2.10}$$

where $\mathcal{E}$ is normalisation factor that depends on the orbital parameters and v is the relative velocity between the two interacting objects, $\overline{\boldsymbol{v}}$ is the velocity vector, $\overline{\boldsymbol{r}}$ is the position vector and n is a constant which in Tsunami is set to $n = 4$. The normalisation factor can be calculated if the theoretical energy loss per orbit is known. By considering a tidal object, t, and a perturber, p, this can be approximated as (Press & Teukolsky, 1977):

$$\Delta E \approx \left(\frac{GM_t^2}{R_t}\right)\left(\frac{M_p}{M_t}\right)^2\left(\frac{R_t}{r_p}\right)^6 \times T(\eta) \tag{2.11}$$

where r_p is the initial orbital pericentre distance, $T(\eta)$ is a function that depends on the internal structure of the tidal object with no analytical solution and is instead approximated by the use of

fitting functions (Giersz, 1985; Portegies Zwart & Meinen, 1993). η is a parameter given by

$$\eta = \left(\frac{M_t}{M_t + M_p}\right)^{1/2} \left(\frac{r_p}{R_t}\right)^{3/2} \tag{2.12}$$

With the energy loss per orbit known, the normalisation factor can be calculated by

$$\mathcal{E} = \Delta E \times \frac{1}{2} \frac{[a(1-e^2)]^{n-1/2}}{(GM)^{1/2}\, \mathscr{F}(e,n)} \tag{2.13}$$

where e is the initial eccentricity and $\mathscr{F}$ is the solution to the integral

$$\mathscr{F}(e,n) = \int_{-\theta_0}^{+\theta_0} \frac{(1+e\cos\theta) - (1-e^2)/2}{(1+e\cos\theta)^{2-n}} \tag{2.14}$$

where θ_0 is the initial true anomaly and assumed to be $\theta = \pi$. For $n = 4$ this evaluates to

$$\mathscr{F}(e, n=4) = \frac{\pi}{2}(2 + 7e^2 + e^4) \tag{2.15}$$

2.5 Initial setups

The sections below will describe the different setups that were used to simulate the binary-single encounters. All of these runs were made using a tidal tolerance set to 10^{-7} and relative and absolute accuracy set to 10^{-9} unless stated otherwise. We assume a simple power law for the radii of stars:

$$R_\star = M_\star^\xi \tag{2.16}$$

where $\xi = 0.57$ and we assume that we are only working with main-sequence stars. The parameters used are:

- semi-major axis (a)
- Eccentricity (e)
- Mass of star (m)
- Radius of star (r)
- Impact parameter (b)
- Velocity at infinity (v_∞), defined as the velocity when the objects are at infinite separation, i.e. before any energy has been exchanged.

Subscripts corresponds to the objects where 0 is the initial single, 10 is the first object in the binary and 11 is the second object in the binary. Table 2.1 shows the initial parameters for the tests and comparisons to previous works as well as the two binary star-star interaction sets.

Section 2.5.1 contains a comparison to other cross-section calculations from previous works. Section 2.5.2 introduces the setups used to simulate and later calculate the cross-sections for different outcomes. Section 2.5.3 introduces the dataset extracted from the MOCCA Survey Database I (Askar et al., 2017)

2.5.1 Tests and comparisons

In order to test the N-body codes and the cross-section calculations, we perform comparisons to previous work by Hut & Bahcall (1983) and Fregeau et al. (2004) where the exchange and ionization

Parameter	Tests and comparisons	2a	2b
a	1 AU	1 AU	1 AU
e	0	0 - 0.99	0 - 0.99
m_0	0.5 $M_\odot$	2 $M_\odot$	2 $M_\odot$
m_{10}	0.5 $M_\odot$	1 $M_\odot$	1.2 $M_\odot$
m_{11}	0.5 $M_\odot$	1 $M_\odot$	1 $M_\odot$
r_0	0.674 $R_\odot$	1.48 $R_\odot$	1.48 $R_\odot$
r_{10}	0.674 $R_\odot$	1 $R_\odot$	1.11 $R_\odot$
r_{11}	0.674 $R_\odot$	1 $R_\odot$	1 $R_\odot$
b	0 - b_{max}	0.1a - 10a	0.1a - 20a
v_∞	$1/2v_c$ - $16v_c$	$0.1v_c$ - $1.2v_c$	10 km/s

Table 2.1: Initial setups.

cross-sections were investigated for binary-single interactions. We create a similar dataset where the semi-major axis is set to $a = 1$ AU and the eccentricity is set to $e = 0$. We assume equal mass stars with mass 0.5 $M_\odot$ and radius 0.67 $R_\odot$ from eq. 2.16. The minimum impact parameter, b_{min}, is set to 0 and the maximum impact parameter, b_{max}, is calculated by

$$b_{max}(v_\infty) = (C/v_\infty + D)a \tag{2.17}$$

where v_∞ is the initial relative velocity between the binary and single and C and D are two constants which has to be chosen appropriately. For this test, $C = 4$ and $D = 0.6(1 + e)$ are used since this choice is appropriate for studying ionization cross-sections. The interactions are distributed along this range of impact parameter with a step size of $\Delta b = 0.01$. The velocity at infinity is chosen in the range $v_\infty = (1/2, 16)v_c$ with step size $\Delta v_\infty = 0.1$. This results in a set of approximately 47,000 interactions.

We also include the analytical approximations for the exchange and ionization cross-sections from Hut & Bahcall (1983):

$$\sigma_{ex}(v_\infty, e) = \frac{640}{81}\pi a^2 \frac{1}{v_\infty^6} \tag{2.18}$$

$$\sigma_{ion}(v_\infty, e) = \frac{40}{9}\pi a^2 \frac{1}{v_\infty^2} \tag{2.19}$$

This set was simulated with three different configurations: No regularization, KS regularization and ARChain to observe the impact of the different regularization methods on the exchange and ionization cross-sections. The results from these runs are shown in section 3.2

2.5.2 Binary star-star interactions

We create two sets of interactions which are simulated three times with no regularization, KS regularization and the ARChain where we have a binary consisting of two stars interacting with a star. We name them setup 2a and 2b and the initial parameters are shown in table 2.1 where the largest difference between the sets is that v_∞ is variable for 2a but fixed to 10 km/s for 2b. Setup 2a contains approximately 119,000 interactions and setup 2b contains approximately 20,000 interactions. The results from these runs are shown in sections 3.3 and 3.4.

2.5.2.1 Point-masses

In order to study the interactions without any mergers we create a setup identical to setup 2b in section 2.5.2 but with the radii of the objects set to 0. The objects are then seen as point-masses

and no mergers are possible. This is done to more easily investigate the correlation between flybys and exchanges without any kinds of mergers making the problem more complicated.

2.5.3 Interacting black holes from MOCCA Survey Database I

MOCCA (Giersz et al., 2013) is a Monte Carlo simulation code which can be used to investigate the evolution of GCs. Since the code is built on Monte Carlo approximations it is not as accurate as a pure N-body integrator but it is much quicker and results are in good agreement with direct N-body codes (Giersz et al., 2013; Wang et al., 2016). The code has been used to simulate a large number of star clusters with different initial conditions with results reported in e.g. the MOCCA Survey Database I (Askar et al., 2017). We use results of MOCCA simulations to obtain three sets of 100,000 interactions each: the first set contains 1 black hole and 2 stars, the second set contains 2 black holes and 1 star and the third set contains 3 black holes. These sets are simulated using the input flags: No regularization, KS regularization, ARChain, PN terms, tides and PN terms + tides. However, since tides affects large stars the most and tides on black holes may lead to computational errors we do not include tides in any of the runs with 3 black holes. The results from these runs are shown in section 3.5.

While the MOCCA Survey Database I contains a few million binary-single interactions involving at least one black hole from nearly a thousand simulated cluster models, we restricted ourselves to 100,000 interactions for each set in order to keep a manageable number of interactions. Nearly all of these interactions come from star cluster models in which black hole natal kicks had been lowered based on mass fallback prescriptions of (Belczynski et al., 2002), this leads to a higher initial retention of black holes in the GC model.

2.6 Framework to simulate interactions and analyze results

In order to carry out this project we need to simulate and analyze a large number of interactions. This section will briefly discuss the process that this is done in. We create a script to read and run the interactions that we previously created or obtained from MOCCA, this script also saves all the necessary data from the interaction. We then convert the final state vector of the objects from Cartesian to Keplerian coordinates to find the semi-major axis and eccentricity of the resulting binary if there is one. All of this data is then read into a script which allows us to plot and analyze the parameters of interest.

Chapter 3

Results

The layout of this chapter is: in section 3.1 we give examples of individual interactions where the outcome changes based on the integrator and its settings and show their trajectories. In section 3.2 we perform tests by carrying out binary-single interactions of equal mass stars and calculate cross-sections. These results are compared with previous works including results from Hut & Bahcall (1983). In sections 3.3 and 3.4, we present results from interactions in which we manually setup the initial conditions for the interactions. In section 3.5, we present results from binary-single interactions involving black holes and stars that were extracted from star cluster simulations carried out as part of the MOCCA Survey Database I.

3.1 Example interactions

In this section we present an example of an interaction where the settings of the run changes the outcome and briefly discuss the astrophysical importance of these outcomes. The initial parameters are found in table 3.1 where subscript 0 is the initial single and 1 and 2 are the initial binary components. Object 0 is a black hole of mass 16.84 $M_\odot$, object 1 is a star of mass 1.26 $M_\odot$ and object 2 is a black hole of mass 18.90 $M_\odot$, thus we initially have a black hole-star binary interacting with a single black hole. We present the results of three runs: The first with no regularization, the second with ARChain and the third with ARchain + PN terms. In table 3.2 we list the initial and final semi-major axis and eccentricity. We find that the No regularization and ARChain run resulted in an exchange and thus forms a new binary. This new binary has almost 15 times larger semi-major axis than the initial binary and 55% larger eccentricity. The ARChain + PN run sees a slight increase in both semi-major axis and eccentricity but since we preserve the initial binary the change is not as significant as in the other two runs. The semi-major axis increases by 8.7% and the eccentricity increases by 27%.

a	e	v_∞	b	m_0	m_1	m_2	r_0	r_1	r_2
9.99 AU	0.59	5.09 km/s	1.51 AU	16.84	1.26	18.90	7.14e-5	0.9991	8.44e-5

Table 3.1: Initial configuration of the interaction of section 3.1. Masses are given in $M_\odot$ and radii in $R_\odot$.

	a [AU]	e
initial	9.99	0.59
No reg	147	0.91
ARChain	149	0.89
ARChain + PN	10.86	0.75

Table 3.2: Initial and final binary properties for three runs: No regularization, ARChain and ARChain + PN terms. The No regularization and ARChain runs ended up with an exchange to form a black hole binary and the ARChain + PN run resulted in a flyby which increased both the semi-major axis and eccentricity of the binary.

The trajectories of the three runs are shown in figure 3.1, 3.2 and 3.3. The first two runs both result in an exchange and there are only small differences in the trajectory. The ARChain run is slightly more resonant and the big difference is that binary component 1 is put on a wide orbit before returning and then ejected from the interaction. A resonant encounter is an encounter where a temporary, bound triple system is formed and the objects experiences multiple close encounters during the interaction. The third run is vastly different, the outcome is a flyby and the interaction is much less resonant and we can only see two close interactions before the interaction is finished.

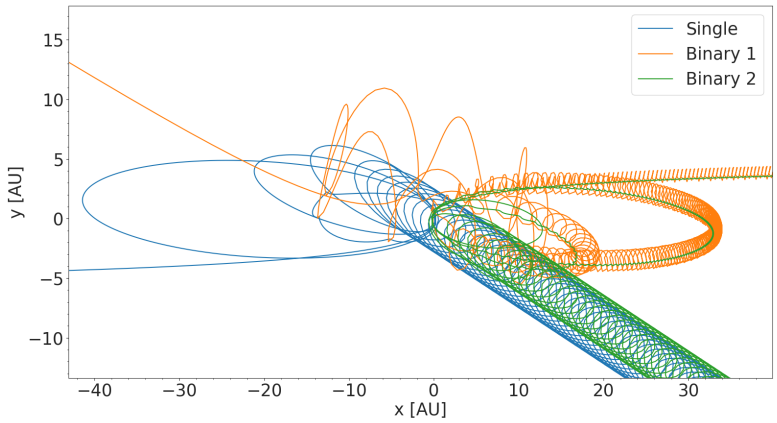

Figure 3.1: Trajectory of the interactions between a black hole-star binary and a single black hole shown in the XY-plane. This plot shows the run with no regularization which results in the formation of a black hole binary.

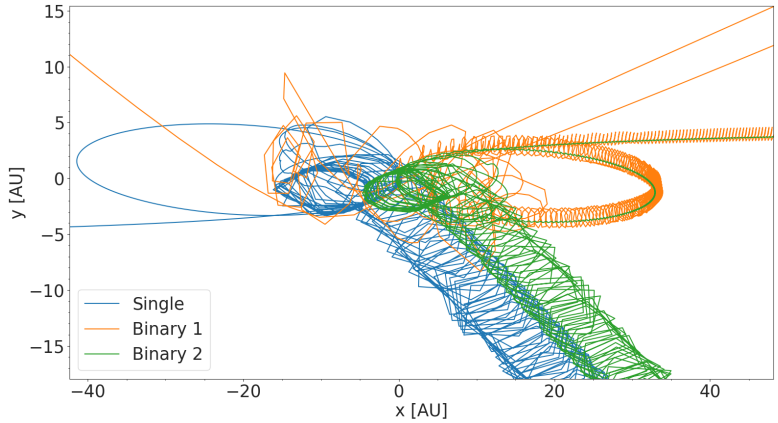

Figure 3.2: Trajectory of the interactions between a black hole-star binary and a single black hole. This plot shows the run with ARChain which results in the formation of a black hole binary.

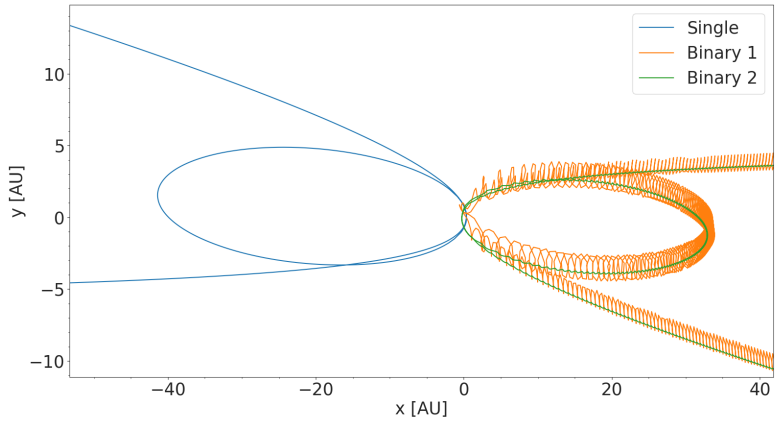

Figure 3.3: Trajectory of the interactions between a black hole-star binary and a single black hole. This plot shows the run with ARChain and PN terms which results in a flyby and an increase in both semi-major axis and eccentricity of the binary.

Here we present another example interaction between a stellar binary and a single star. The binary stars each have masses 1 $M_\odot$ and the single have mass 2 $M_\odot$. The binary properties are $e_{inital} = 0.2$ and $a_{initial} = 1$ AU, the relative velocity is $v_\infty = 0.3 v_c$ and the impact parameter is $b/a = 6.7$. This interaction results in a merger between one of the initial binary components and the single star. A merger like this may produce a blue straggler star.

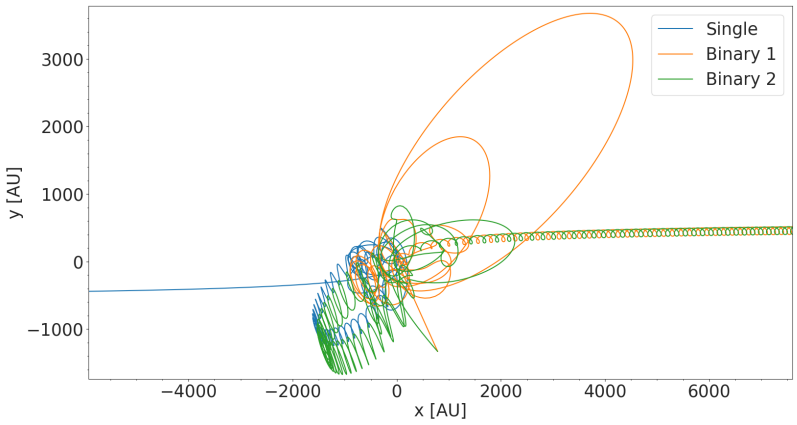

Figure 3.4: Trajectory of an interaction between a stellar binary and a single star where the interaction causes one of the initial binary components and the single star to merge.

3.2 Tests and comparisons

Here we simulated approximately 47,000 encounters between 3 equal mass stars with mass 0.5 $M_\odot$ where the initial binary semi-major axis was fixed to 1 AU, eccentricity to 0, the impact parameters are uniformly distributed within 0 to b_{max} (see eq. 2.17) and the relative velocity is uniformly distributed within $1/2v_c$ to $16v_c$ where v_c is the critical velocity of the binary (see eq. 1.9). These initial conditions were chosen in order to make a comparison with previous works described in section 2.5.1. A cross-section is a measure of the probability that a specific process will happen during or after an interaction. We are interested in the outcomes of binary-single interactions and thus the cross-sections we investigate are related to the probability that an interaction results in a specific outcome (Heggie & Hut, 2003). From Hut & Bahcall (1983), the cross-sections are calculated with

$$\sigma_X(v_\infty) = \pi b_{max}^2 \frac{N_X}{N} \tag{3.1}$$

where b_{max} is the maximum impact parameter, N_X is the number of an outcome X and N is the total number of interactions for a given v_∞. The error is obtained from Poisson counting statistics:

$$\Delta\sigma_X(v_\infty) = \pi b_{max}^2 \frac{\sqrt{N_X}}{N} \tag{3.2}$$

In addition to this error, some triples exist in metastable states that takes a very long to dissociate and leads to unresolved systems. However, Fregeau et al. (2004) finds that the number of unresolved systems is small and does not significantly contribute to the error. For our runs we do not get any bound triples and therefore this error does not exist for our particular data set.

Statistically, all three runs that we perform (No regularization, KS regularization and ARChain) are very similar and the fraction of outcomes differ by less than 1 %. We find approximately 79% flybys, 6% exchanges and 14% ionizations for all three runs. The number of bound mergers, unbound mergers and triple mergers are less than 1 %.

Figure 3.5 shows the exchange and ionization cross-section from the three runs. The orange dotted line is the analytical exchange cross-section and the blue dotted line is the analytical ionization cross-section. These analytical cross-sections are obtained from Hut & Bahcall (1983) and for exchange is given by

$$\sigma_{ex}(v_\infty) = \frac{640}{810}\pi a^2 \frac{1}{v_\infty^6} \tag{3.3}$$

and for ionization by

$$\sigma_{ion}(v_\infty) = \frac{40}{9}\pi a^2 \frac{1}{v_\infty^2} \tag{3.4}$$

The first interaction that results in ionization for all three runs is seen at $v_\infty = v_c$ as expected since the critical velocity is defined as the velocity required to dissolve the system. The No regularization run and KS regularization run are very similar and differences are difficult to find, however, for the ARChain run we see small differences: the velocity at which ionization is more likely than exchange is slightly higher than for the two other runs but the overall shape of the cross-sections are very similar for all three runs. We see that the probability for an ionization is the highest at or close to the point where $v_\infty = v_c$ and then decreases since at higher relative velocity the objects are more likely to fly past each other without any strong interaction. These results are also very similar to the results from Hut & Bahcall (1983); Fregeau et al. (2004), except for the exchange cross-section after the intersection between exchange and ionization. In Hut & Bahcall (1983) the exchange cross-section follows the analytical cross-section better while our results are a bit off. This might be due to sample size, our set consists of approximately 47,000 interactions while the Hut & Bahcall (1983) paper includes 500,000 interactions.

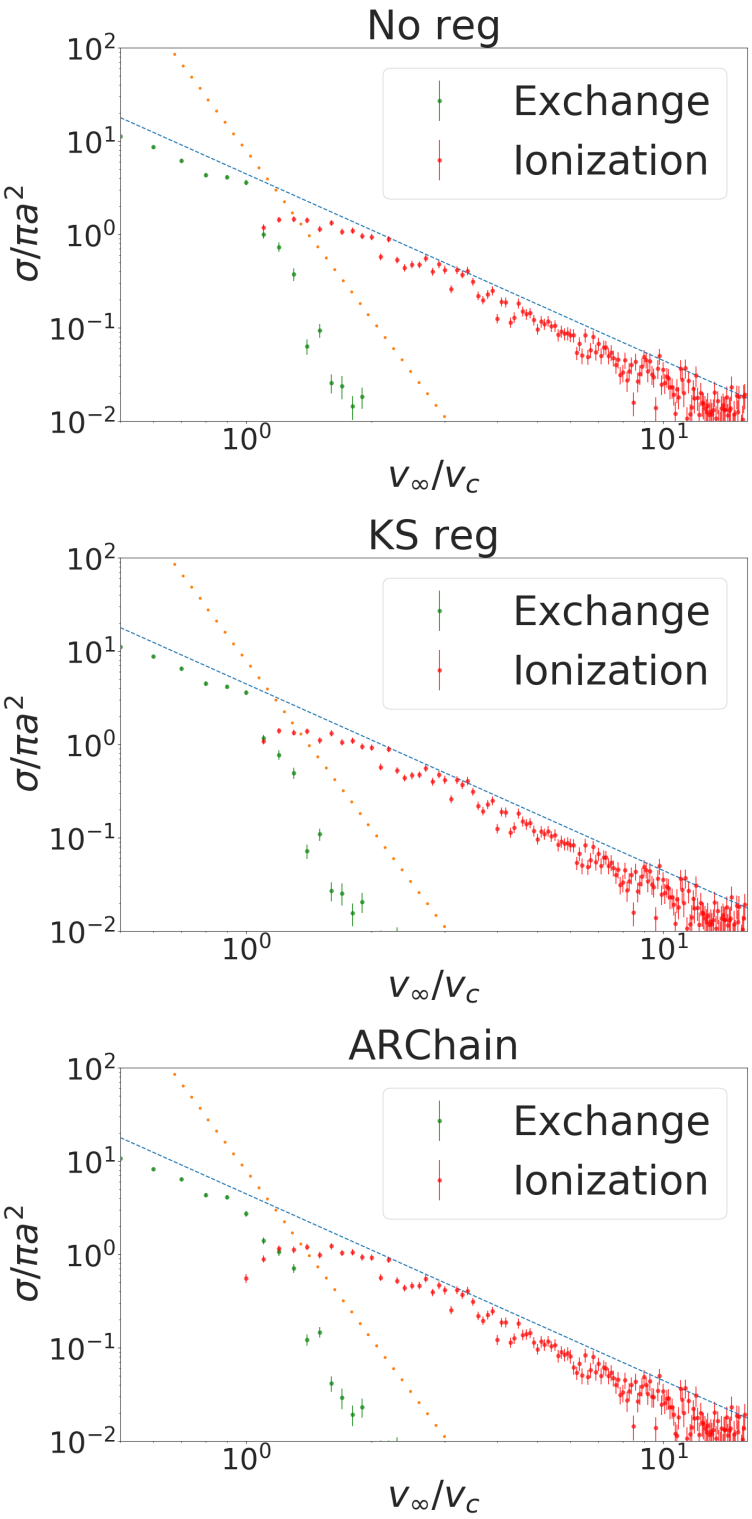

Figure 3.5: Exchange and ionization cross-sections from the tests and comparisons sets for all three runs, No regularization (top), KS regularization (middle) and ARChain (bottom), where the green dots correspond to the exchange cross-section, the red dots to the ionization cross-section, the blue dotted line is the analytical ionization cross-section and the orange dotted line is the analytical exchange cross-section. These plots are compared to figure 5 from Hut & Bahcall (1983)

3.3 Binary star-star interactions (setup 2a)

The results from the runs of setup 2a described in section 2.5.2 are reported in this section. The data set consists of two 1 $M_\odot$ stars in a binary system interacting with a single star of mass 2 $M_\odot$. We fix the semi-major axis to 1 AU and distribute the eccentricity from 0 to 0.99, the impact parameter between 0.1 AU and 10 AU and the relative velocity between $0.1v_c$ and $1.2v_c$, where v_c is the critical velocity (see equation 1.9). This results in a set of approximately 119,000 interactions and the complete initial parameter setup is shown in table 2.1. Figure 3.6 presents the distribution of the final configurations for all three runs. The smaller window shows a zoomed in view on the more rare outcomes. For most outcomes the three runs give similar results, most noticeable is the similarity between no regularization and AR Chain where for most configurations these two runs give very similar results. The run using KS regularization is noticeably different for exchange, where we see an increase of about 3% and bound mergers where we see a decrease of 25%. We also see a decrease in the number of unbound mergers and triple mergers but these differences are smaller than 1%.

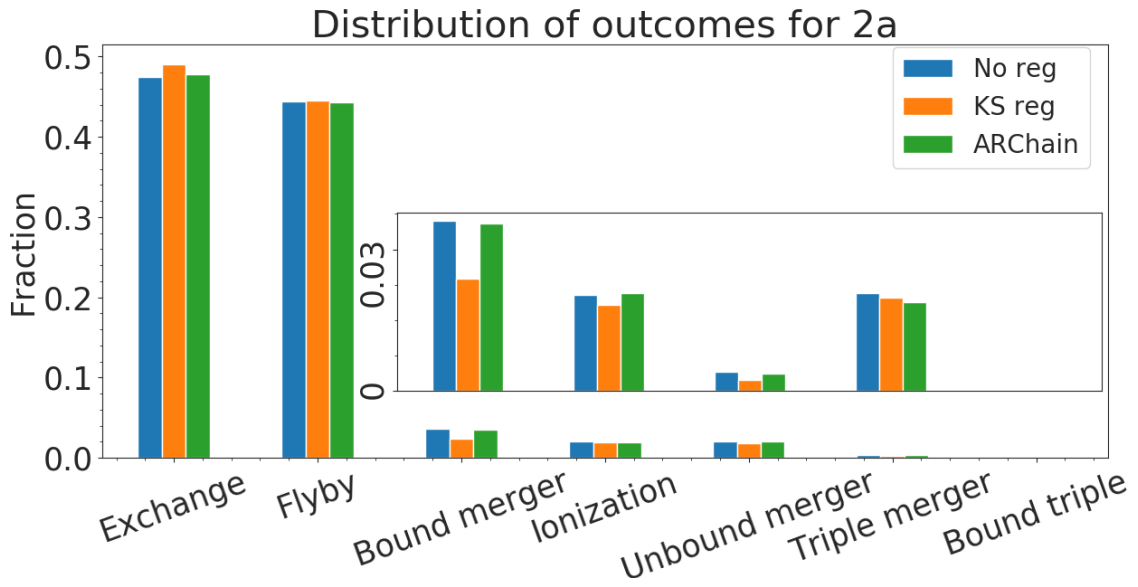

Figure 3.6: Distribution of final configurations for the three different runs of setup 2a. The smaller window shows a zoomed in picture of the distribution of the less likely outcomes: bound merger, ionization, unbound merger, triple merger and bound triple. The set consists of approximately 119,000 binary-single interactions.

3.3.1 Cross-sections

Here we present the cross-sections from the three runs which are calculated using equation 3.1. As previously discussed, a cross-section in this context is a measurement of the probability that an interaction will have a certain outcome. For each run there are two plots: one showing all outcomes and one that is zoomed in on the most likely outcomes. Figure 3.7 shows the run with no regularization, figure 3.8 shows the run with KS regularization and figure 3.9 shows the run with the ARChain. By investigating the velocity at which an interaction is equally likely to result in a flyby as an exchange we find small differences between the runs: the No regularization run and ARChain run are, down to the fourth decimal, the same at $v_\infty/v_c = 0.570$ while for the KS regularization the lines intersect at $v_\infty/v_c = 0.575$. These differences are very small and all three runs are similar and the differences are insignificant for most outcomes. The outcomes that are different are unlikely and the differences may not be statistically significant.

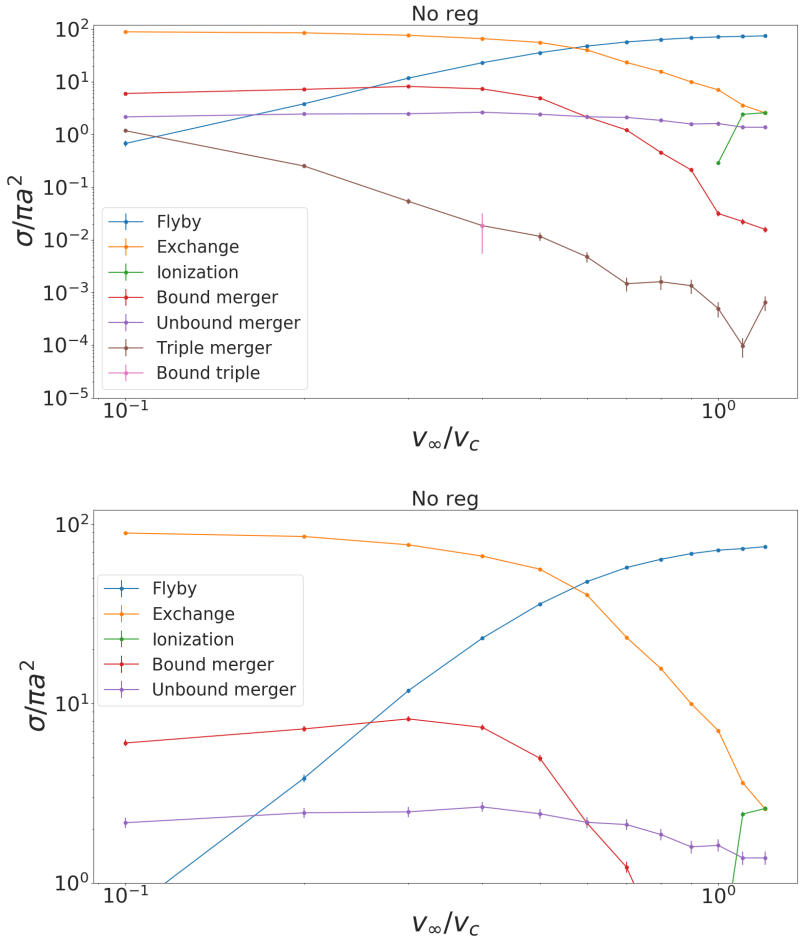

Figure 3.7: Cross-sections for the outcomes from the run with no regularization. The top picture shows the cross-section of all outcomes while the bottom picture is zoomed in on the most probable outcomes.

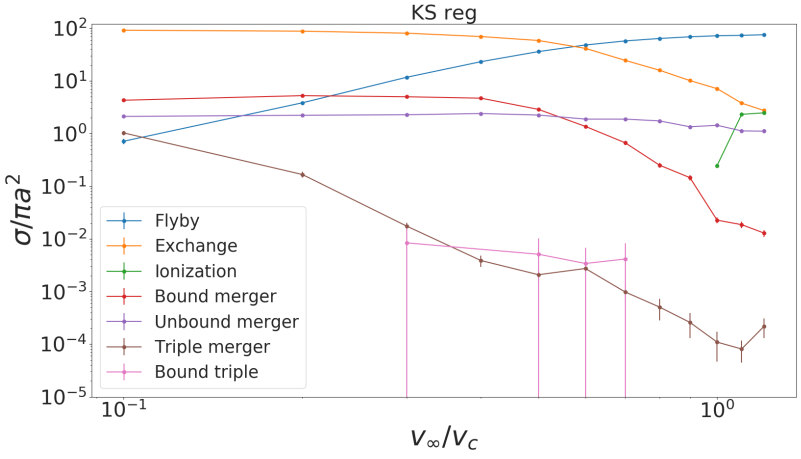

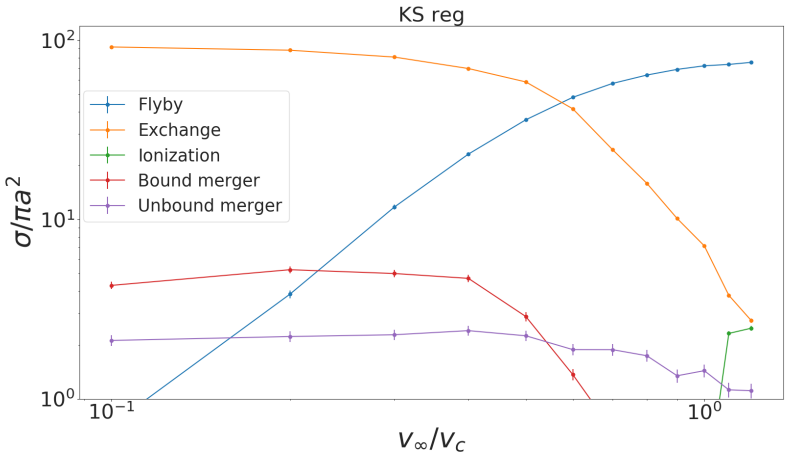

Figure 3.8: Cross-sections for the outcomes from the run with KS regularization. The top picture shows the cross-section of all outcomes while the bottom picture is zoomed in on the most probable outcomes.

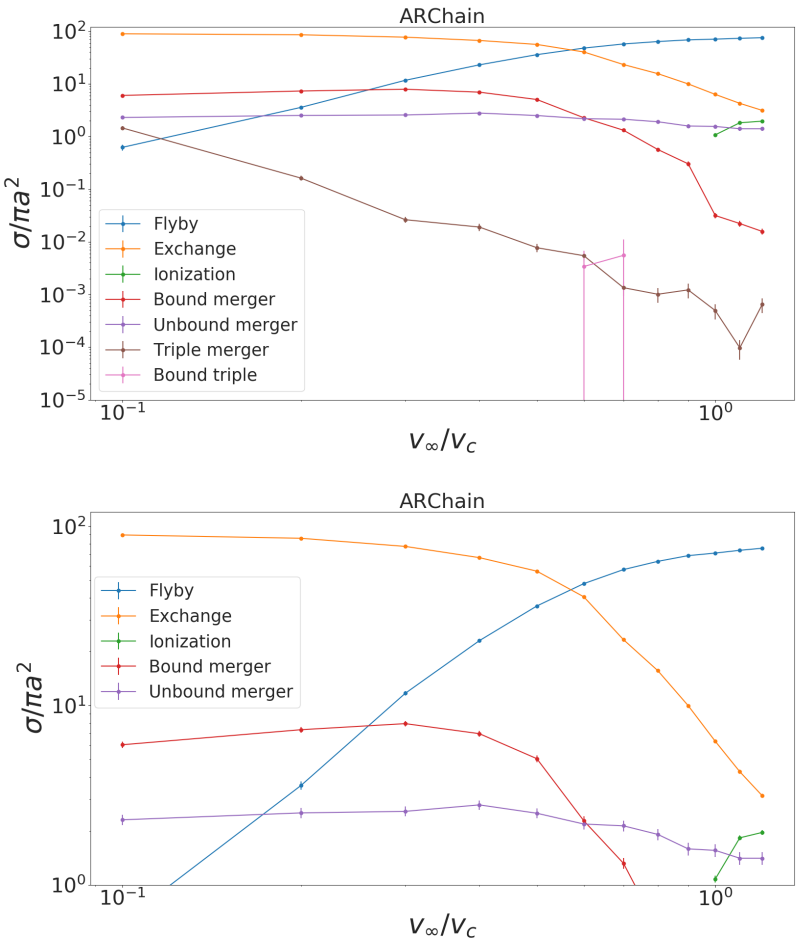

Figure 3.9: Cross-sections for the outcomes from the run with the ARChain. The top picture shows the cross-section of all outcomes while the bottom picture is zoomed in on the most probable outcomes.

3.3.2 Impact parameter

Here we present the distribution of the different outcomes for different impact parameters for all three runs. In figure 3.10 we show the impact parameter distribution for No regularization (top panel), KS regularization (middle panel) and ARChain (bottom panel). The three figures show that there are only slight differences between the three runs, especially in the less likely outcomes, such as ionization. If we look more into the distribution for ionizations we see that the difference between the no regularization run and the KS regularization run is insignificant while for the ARChain run we do not see the initial peak that is visible in the other two runs and we do not have a sharp drop-off at around $b/a = 3$ as in the other two runs. However, the fraction of ionizations is low and this may not be statistically significant. The black dashed line in the plots shows where Flyby and Exchange intersect, i.e. the impact parameter where we have the same number of flybys as exchanges. For the No regularization run and ARChain run this is at $b/a = 4.15$ while for the KS regularization run this is at $b/a = 4.35$.

Figure 3.11 shows the impact parameter distribution for flyby and exchange for all three runs in the same plot. Here the negatively sloped line represents the exchanges and the positively sloped line represents the flybys. We see that all three runs are very similar and the differences are insignificant.

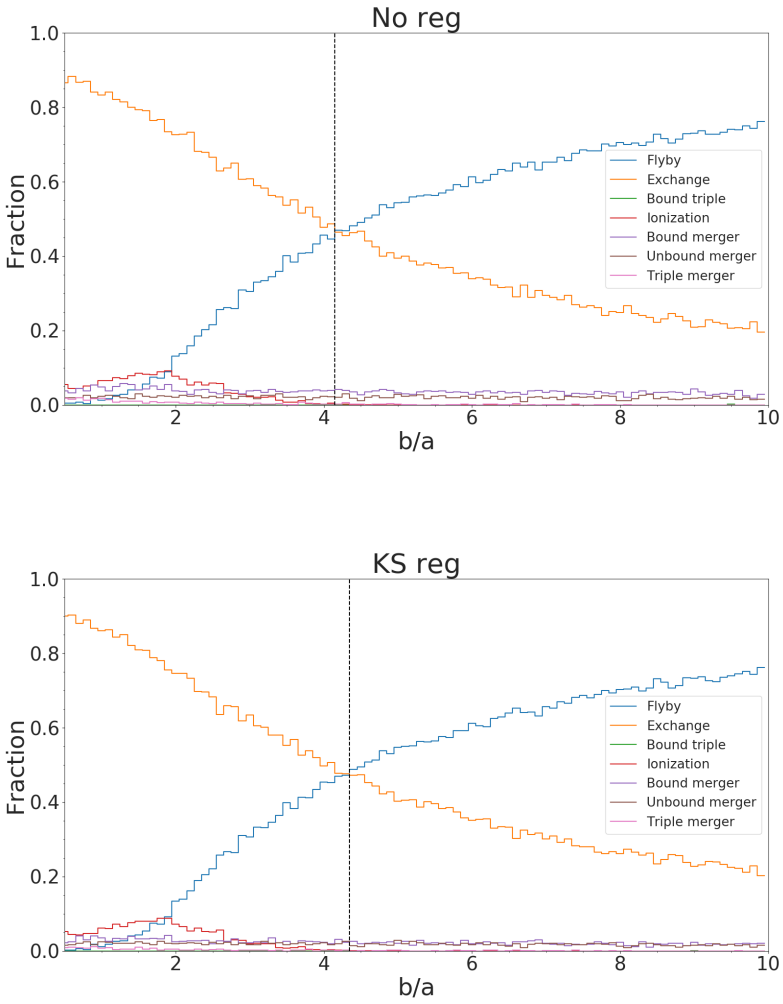

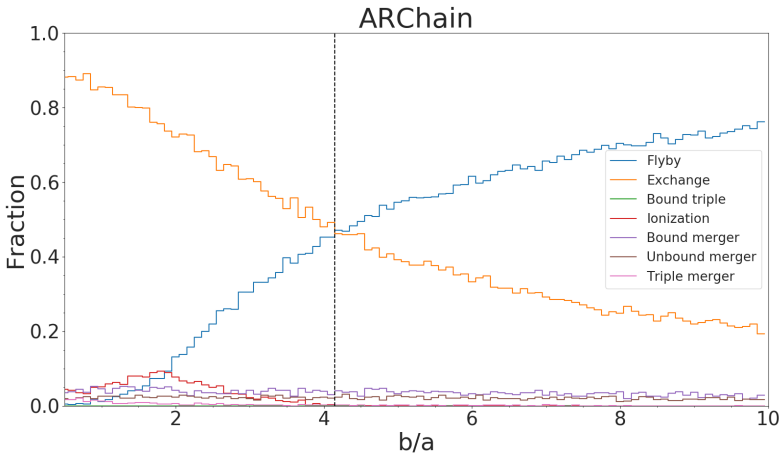

Figure 3.10: Impact parameter distribution for different outcomes from the No regularization run (top panel), KS regularization run (middle panel) and ARChain run (bottom panel). The different coloured, solid lines correspond to a specific outcome and the black dashed line shows at which impact parameter the flybys and exchanges are equally probable.

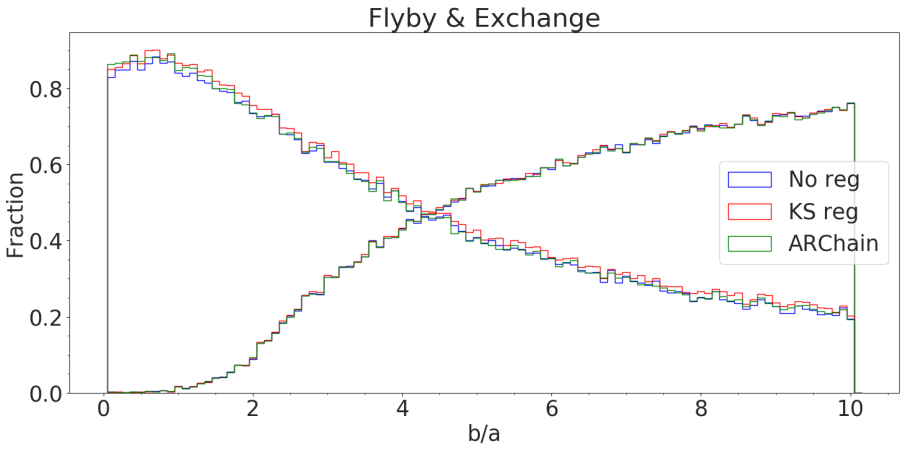

Figure 3.11: Distribution of flybys (increasing line) and exchanges (decreasing line) for all three runs.

3.3.3 Eccentricity distribution

In this section, we show the final eccentricity distribution for all three runs of setup 2a where the eccentricity is given as e^2. In 1919, Jeans found out that if a binary experiences a large number of dynamical encounter where energy is exchanged, the eccentricity distribution can be described as $dN/de = 2e$ (Jeans, 1919). This is now referred to as the thermal eccentricity distribution and is used for initial conditions. However, observations seems to suggest that the distribution is not thermal but is flatter and is more uniformly distributed (Geller et al., 2019). We split the outcomes into separate plots where the left panel of figure 3.12 shows the e^2 distribution for flybys and the right panel for exchanges. We see that there is a clear bias towards low eccentricity for the flybys where for exchanges the curve is fairly flat although low eccentricities are slightly favoured. Disregarding these biases, we have a quite uniform e^2 distribution which relates to a thermal eccentricity distribution. These features are the same for all three runs and we cannot see any clear differences between the runs.

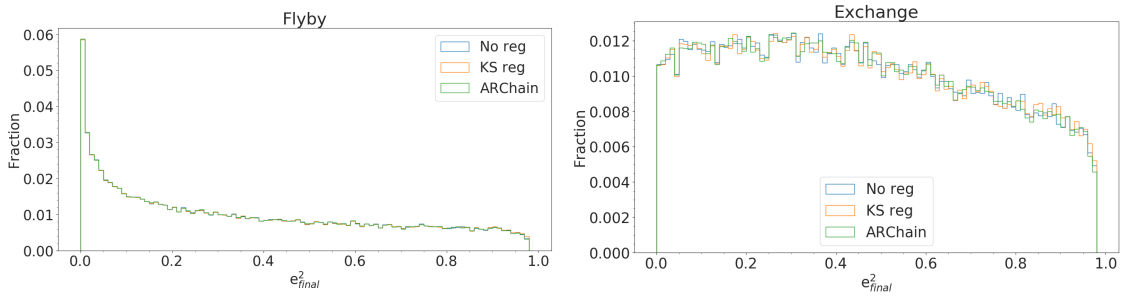

Figure 3.12: Distribution of eccentricity for the three runs for flybys (left panel) and exchanges (right panel).

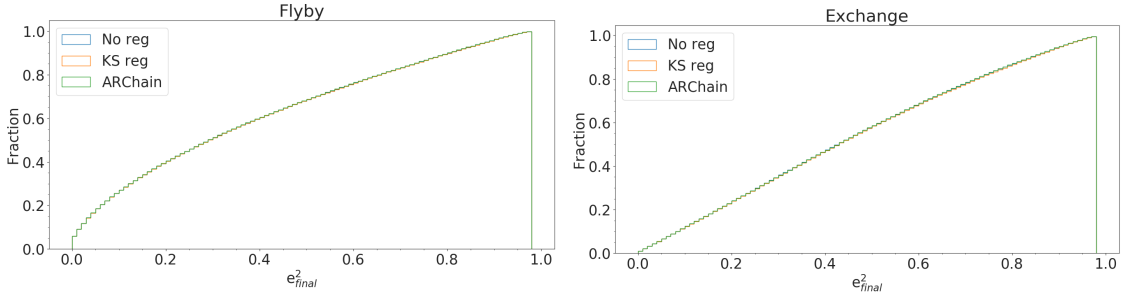

Figure 3.13: Cumulative distribution function for the eccentricity distribution for flybys (left panel) and exchanges (right panel).

We investigate the distribution of eccentricity before and after the interaction by plotting the distribution of both parameters against each other. We split up the outcomes into different figures, flybys are plotted in figure 3.14 where we have plotted the initial eccentricity on the x-axis and the final eccentricity of the y-axis with the colour coding corresponding to the number in each bin. The top left panel corresponds to the no regularization run while the top right panel corresponds to the KS regularization run and the bottom panel corresponds to the ARChain run. For all three runs we see a bias towards $e_{initial} = e_{final}$ where the interaction was quite weak and did not affect the eccentricity binary greatly. There is also a slight bias towards higher final eccentricity which may indicate that our interactions do not circularise our binaries and instead the binaries, on a statistical scale, become more eccentric after the interaction. However, we note very little and insignificant differences between the three runs.

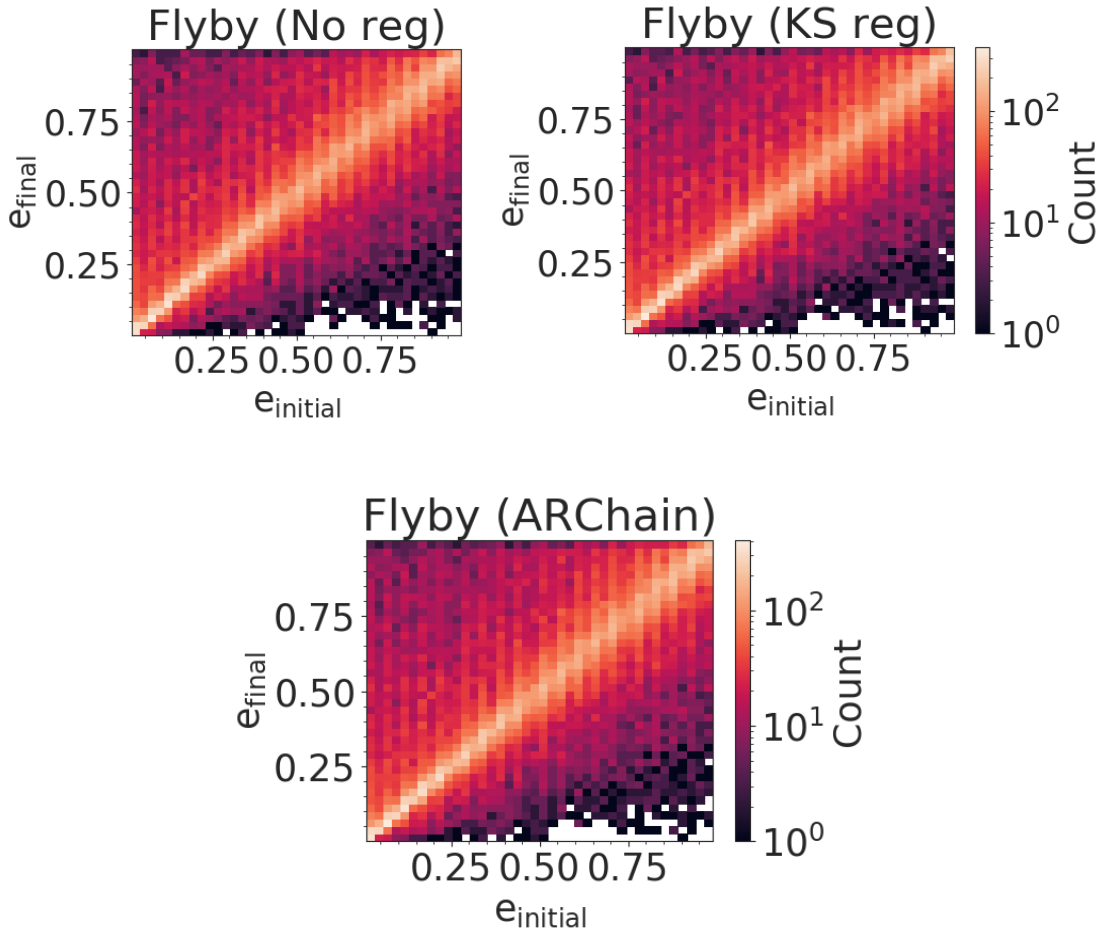

Figure 3.14: The initial and final eccentricity distribution for flybys with the initial eccentricity on the x-axis and the final eccentricity on the y-axis. The three panels show the distribution for flybys from the no regularization run (top left panel), the KS regularization run (right panel) and the ARChain run (bottom panel).

We make the same plots for exchanges which can be seen in figure 3.15. For this outcome we see no clear bias and the distribution is much more uniform than for flybys. We do see a decrease in the number of low eccentricity binaries after the interaction which may indicate that the new binaries that we form are more likely to be eccentric rather than circular.

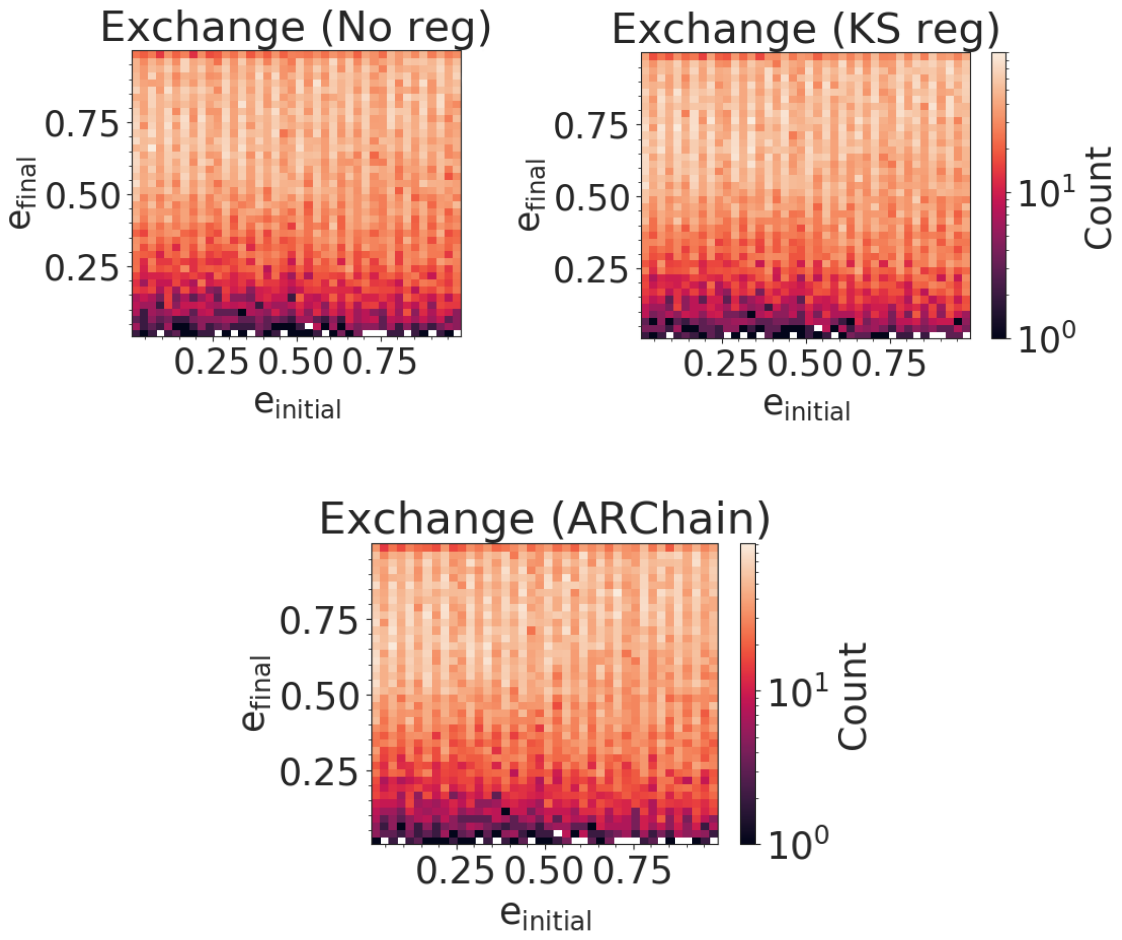

Figure 3.15: The initial and final eccentricity distribution for exchanges with the initial eccentricity on the x-axis and the final eccentricity on the y-axis. The three panels show the distribution for flybys from the no regularization run (top left panel), the KS regularization run (right panel) and the ARChain run (bottom panel).

We also investigate if there is any difference in the final semi-major axis and eccentricity based on the regularization method. We split flybys and exchanges into separate plots and plot the final semi-major axis on the x-axis and the final eccentricity on the y-axis. In figure 3.16 we plot the interactions which results in a flyby for no regularization (top left panel), KS regularization (top right panel) and ARChain (bottom panel). The differences between the two runs are very small with no clear differences in either eccentricity or semi-major axis. The same plots for exchanges are shown in figure 3.17 where, similarly to the flybys, we see no clear differences between the three runs and the three distributions are very similar.

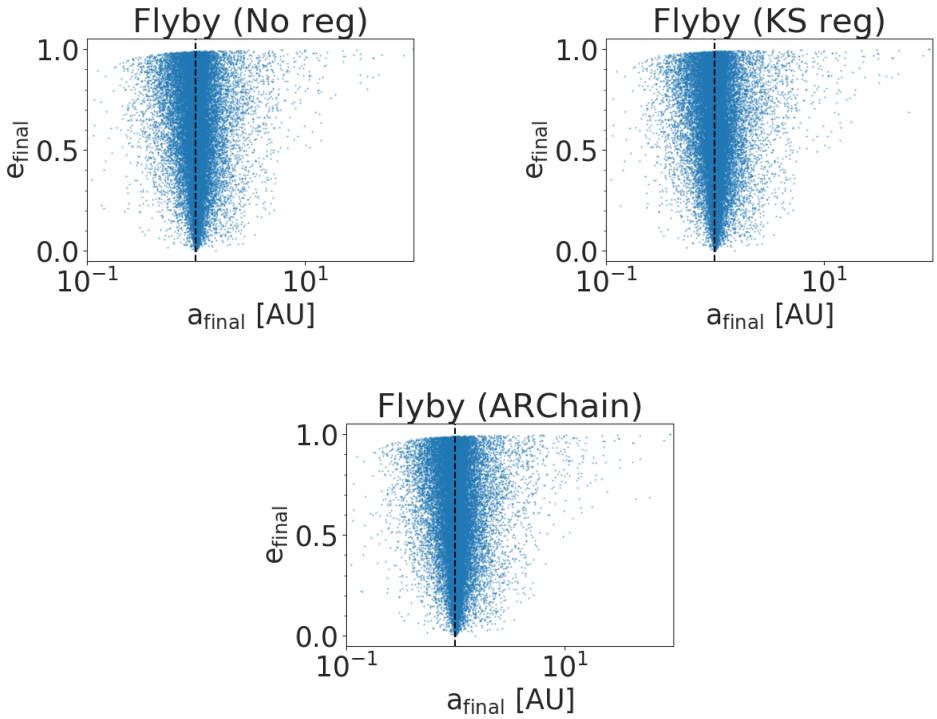

Figure 3.16: The final semi-major axis plotted against the final eccentricity of the binary for flybys. The black line corresponds to the initial semi-major axis of $a = 1$ AU. We find that the distributions of parameters are very similar across all three runs.

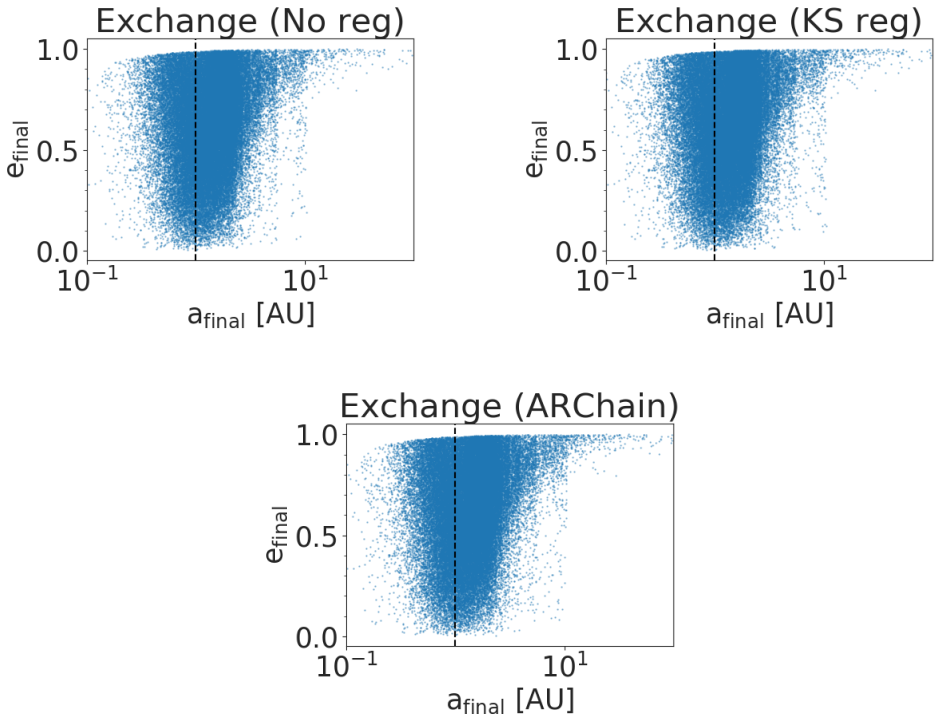

Figure 3.17: The final semi-major axis plotted against the final eccentricity of the binary for exchanges. The black line corresponds to the initial semi-major axis of $a = 1$ AU. We find that the distributions of parameters are very similar across all three runs.

3.3.4 Accuracy

The numerical accuracy of a simulation could potentially change the outcome of an interaction. A higher accuracy leads to more accurate results while the computation time increases, while on the other hand a lower accuracy decreases the computation time but may lead to inaccurate results. Fewbody allows the user to specify the absolute (A_{abs}) and relative accuracy (A_{rel}) which, for simplicity's sake we always keep equal. We investigate how a change in accuracy affects our simulations on a statistical scale for three different values on the accuracy. A lower value on $A_{abs,rel}$ leads to higher accuracy. Since the accuracy of the ARChain runs is not affected by the user settings we limit our runs to No regularization and KS regularization. The default accuracy is $A_{abs,rel} = 1e-9$, for the runs with a lower accuracy we set $A_{abs,rel} = 1e-5$ and for the higher accuracy runs we set $A_{abs,rel} = 1e-15$.

3.3.4.1 Energy and angular momentum conservation

Figures 3.18 and 3.19 show the distribution of energy conservation for the different runs. The plots clearly show that a higher accuracy setting leads to several orders of magnitude better conservation of energy for both the No regularization and KS regularization runs. The angular momentum conservation is shown is figures 3.20 and 3.21 and similarly to the energy conservation we see an improvement of several orders of magnitude with a higher accuracy.

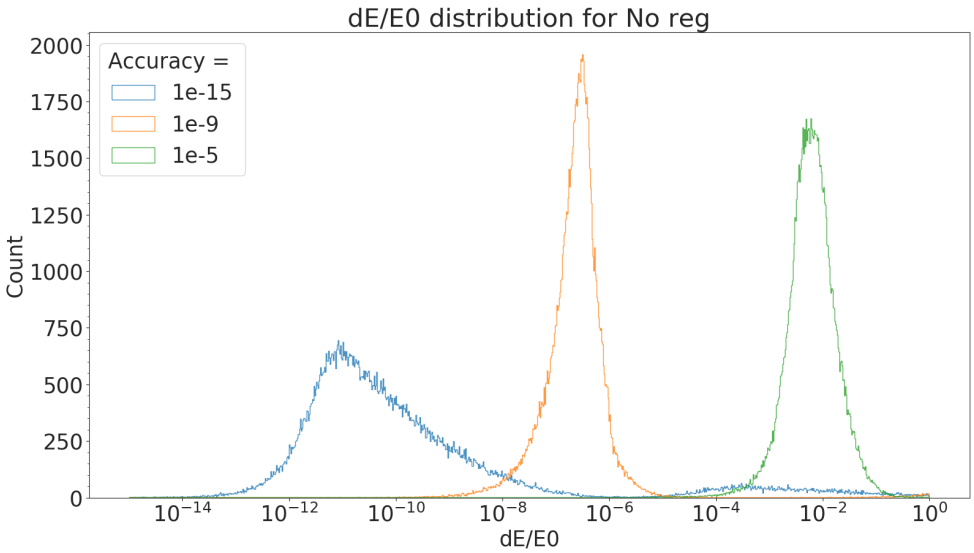

Figure 3.18: Distribution of energy conservation for the No regularization run of setup 2a where dE is the change in energy and $E0$ is the initial energy.

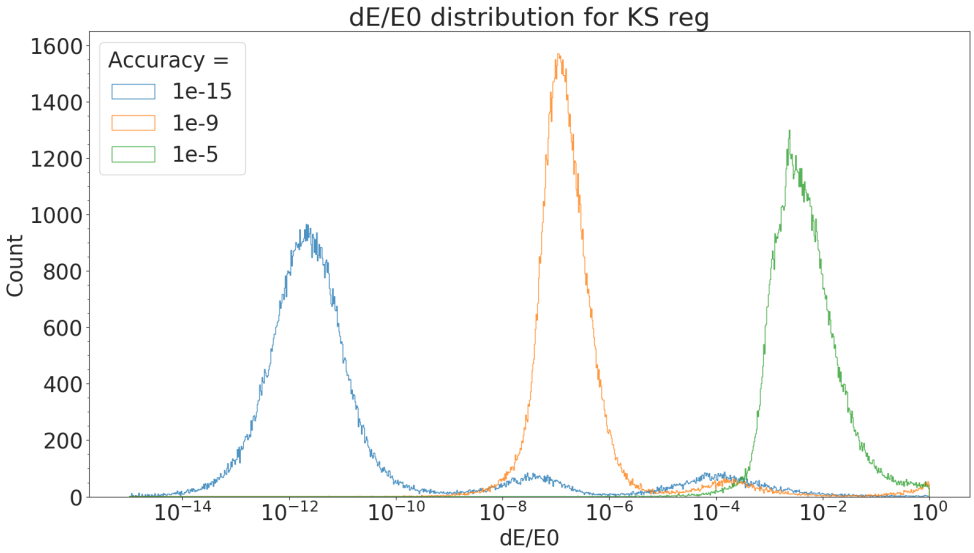

Figure 3.19: Distribution of energy conservation for the KS regularization run of setup 2a where dE is the change in energy and $E0$ is the initial energy.

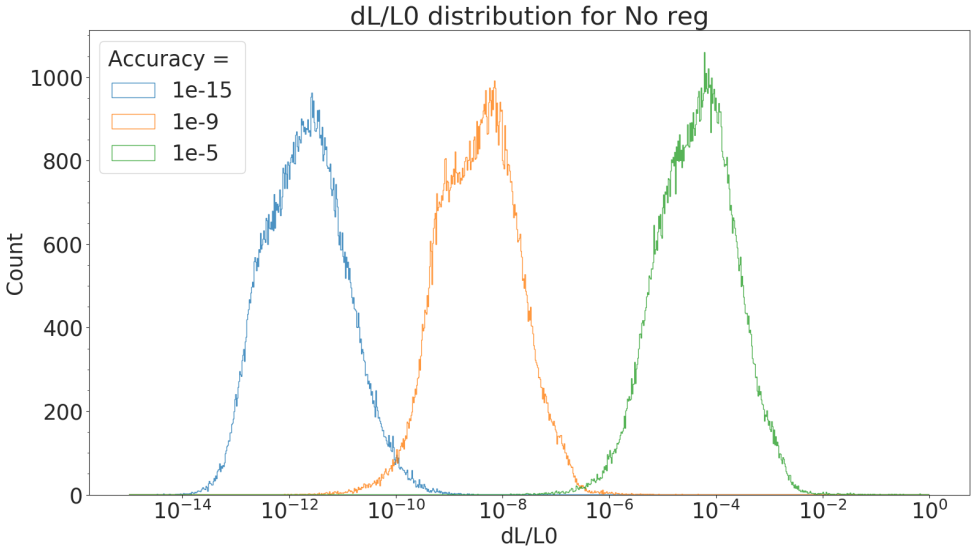

Figure 3.20: Distribution of angular momentum conservation for the No regularization run of setup 2a where dL is the change in angular momentum and $L0$ is the initial angular momentum.

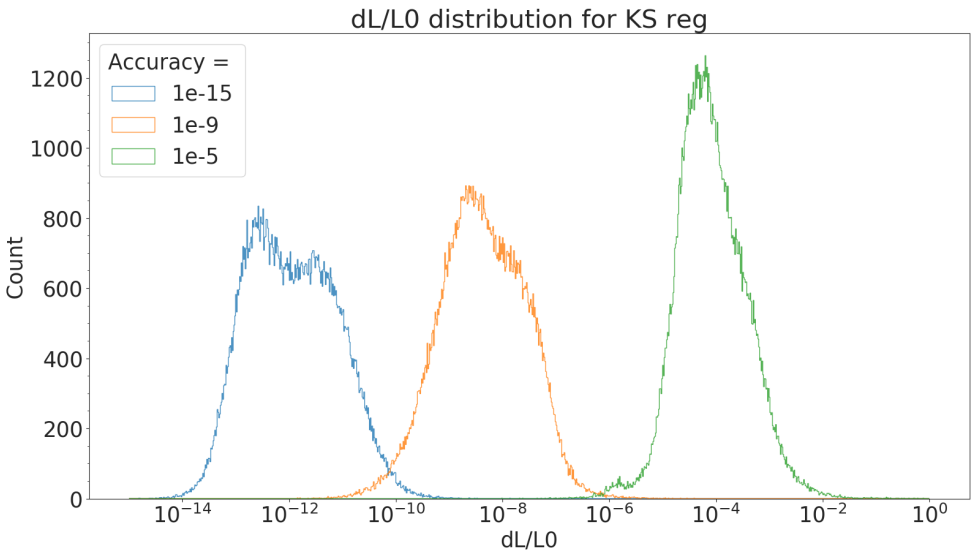

Figure 3.21: Distribution of angular momentum conservation for the KS regularization run of setup 2a where dL is the change in angular momentum and $L0$ is the initial angular momentum.

3.3.4.2 Outcomes

Here we present the distribution of outcomes in figure 3.22 for different accuracy settings. From this plot it seems like a higher/lower accuracy affects the KS regularization runs more than the no regularization runs although this is not the case for all outcomes. The number of bound mergers are even across all No regularization runs while for the KS regularization runs they vary greatly. For ionizations it seems like the accuracy affects both the No regularization and KS regularization runs.

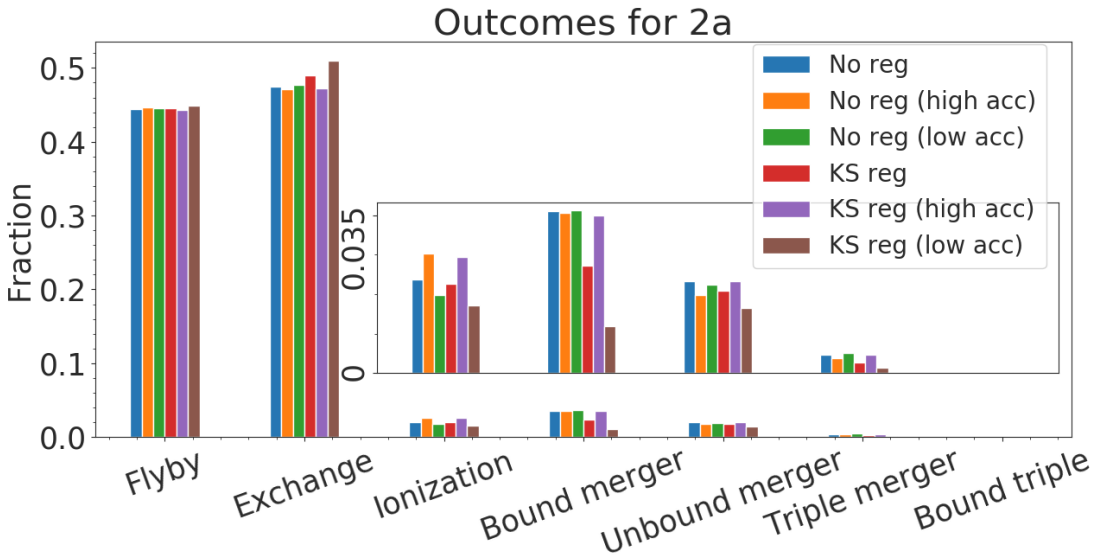

Figure 3.22: Distribution of outcomes for the No regularization and KS regularization runs of the 2a data set with different accuracy settings. The set consists of approximately 117,000 binary-single interactions.

3.4 Binary star-star interactions: fixed relative velocity (setup 2b)

This section and its subsections contains the results from the runs of setup 2b, explained in section 2.5.2 where we include 3 stars of masses 2 $M_\odot$ (single), 1.2 $M_\odot$ and 1 $M_\odot$ (binary components). We fix the semi-major axis to 1 AU and the relative velocity to 10 km/s. This data set, consisting of approximately 20,000 interactions, is simulated in three different runs; No regularization, KS regularization and ARChain. Figure 3.23 shows the distribution of the final configurations for all three runs. The smaller window shows a zoomed in view on the most uncommon outcomes. The No regularization run and the ARChain run are very similar for all outcomes while the KS regularization run differs slightly.

The most notable differences between the KS regularization run and the other two is an increase in exchanges and decrease in bound mergers. The three most unlikely outcomes (unbound mergers, triple mergers and bound triples) also shows a difference between the runs but once again the No regularization run and the ARChain run are very similar and the difference arises for the KS regularization run. However, this is not the case for bound triples where the number of bound triples are significantly lower for the ARChain run than for the No regularization run. The fact that we see this fraction of bound triples is quite interesting since we should not be able to form a stable hierarchical triple system without any process to remove energy from the interaction (e.g. gravitational wave emission or tidal effects, see section 1.3.3). The differences might arise from the differences in terminating the interaction, these triples might be very loosely bound metastable systems which will eventually dissolve on their own but the time this would take is longer than the simulation allows. The addition of these regularization methods might "help" the integrator to recognise these very loosely bound systems and classify them as exchanges or flybys instead of bound triples.

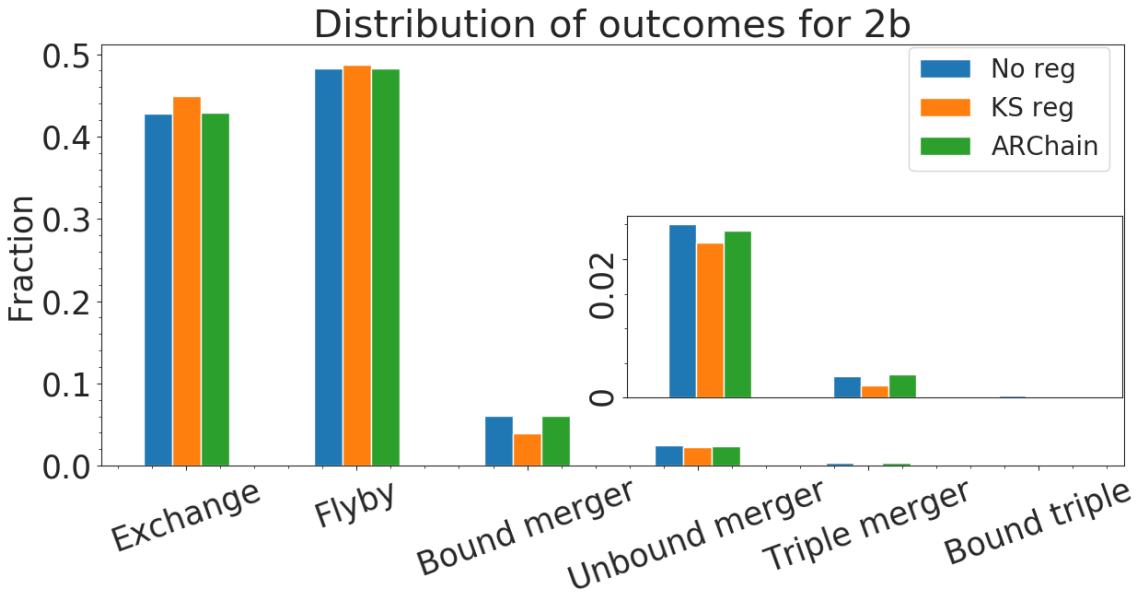

Figure 3.23: Distribution of final configurations for the three different runs of setup 2b. The smaller window shows a zoomed in picture of the distribution of the less likely outcomes.

3.4.1 Impact parameter

This subsection contains the impact parameter distribution for the three runs of setup 2b: figure 3.24 shows the impact parameter distribution for different outcomes from the No regularization

run (top panel), KS regularization run (middle panel) and ARChain run (bottom panel). The impact parameter is given as b/a where b is the impact parameter and a is the initial semi-major axis of the binary. We have split up the outcomes in order to see in which impact parameter range we are most likely to see each outcome. We see no significant differences between the three runs and in all runs we are most likely to get an exchange for low impact parameters while for high impact parameters a flyby is the most likely outcome. In figure 3.25 we only show the exchanges and flybys but we include all three runs in the same plot. The lines that are negatively sloped represent the exchanges while the positively sloped lines represent the flybys. Here we can clearly see the similarities between the runs, the two outcomes cross at approximately the same impact parameter and the number of exchanges drop to 0 while the flybys plateau at the same impact parameter for all three runs.

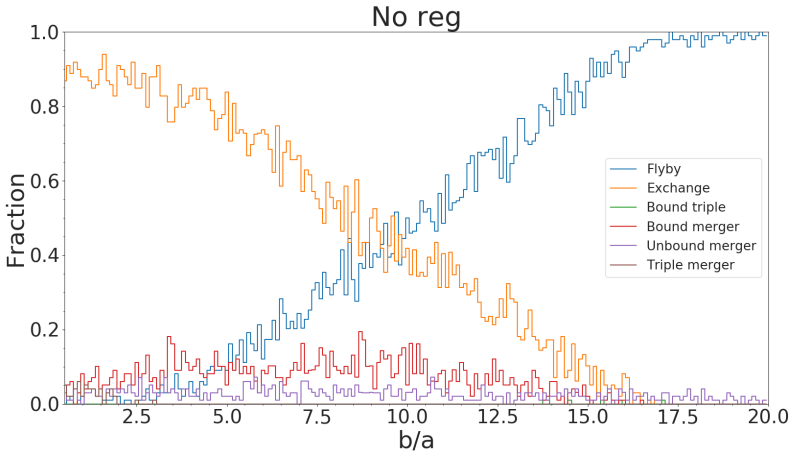

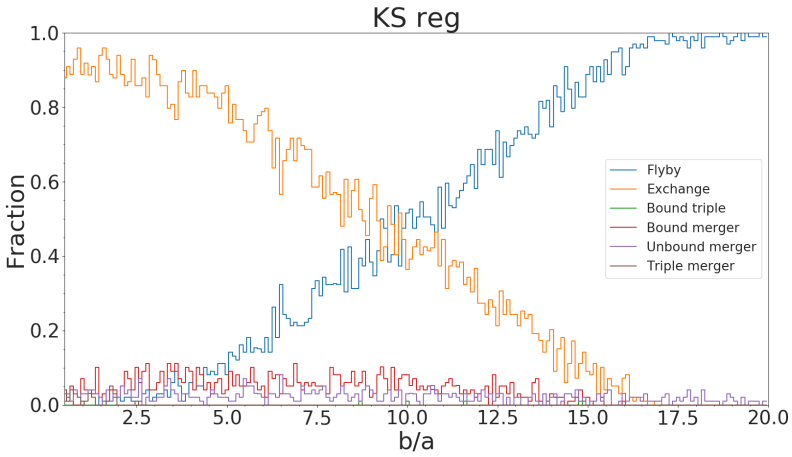

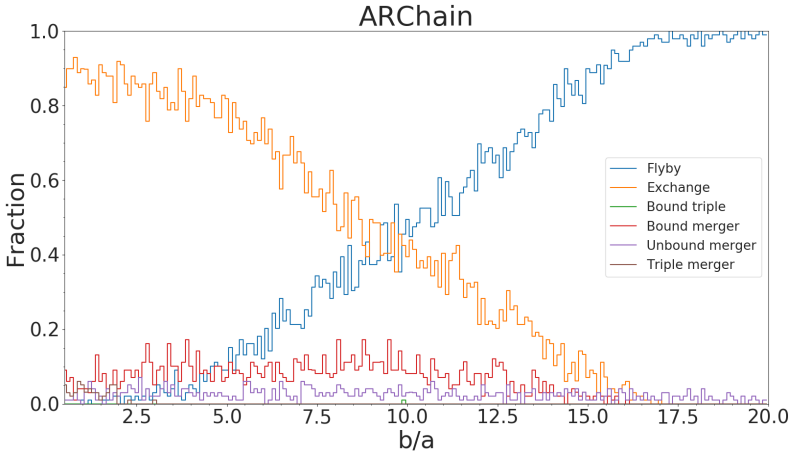

Figure 3.24: Impact parameter distribution for different outcomes from the No regularization run (top panel), KS regularization run (middle panel) and ARChain run (bottom panel). The different coloured, solid lines correspond to a specific outcome and the black dashed line shows at which impact parameter the flybys and exchanges are equally probable.

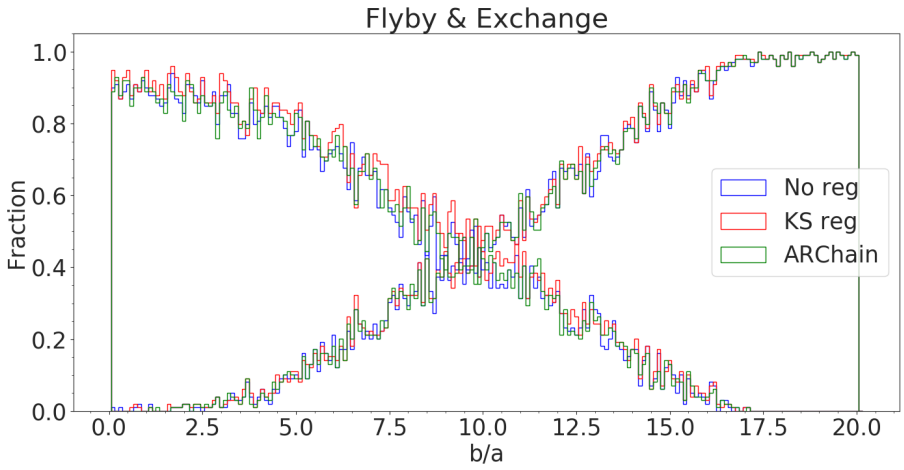

Figure 3.25: Impact parameter distribution for flyby (increasing line) and exchange (decreasing line) for all three runs.

3.4.2 Eccentricity distribution

This section contains the eccentricity distribution for all three runs of setup 2b where the eccentricity is given as e^2. As mentioned in section 3.3.3 the distribution of binary eccentricities in have been believed to follow a thermal distribution if the binary experiences a large number of dynamical interactions. As in section 3.3.3 we split the outcomes into separate plots where the distribution for flybys are shown in figure 3.26 and for exchanges in figure 3.27. We have a bias towards low eccentricity for the flyby case for all three runs and all three runs are in fact very similar with very insignificant differences. For the exchanges we also see a bias towards low eccentricity but to a much lesser degree than for the flybys. Our three runs are also more different for these outcomes but the differences are still quite insignificant.

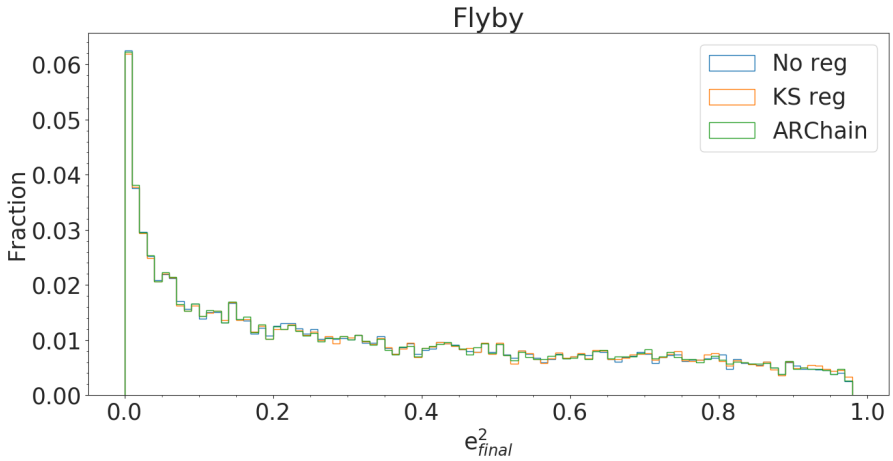

Figure 3.26: e^2 distribution for flyby

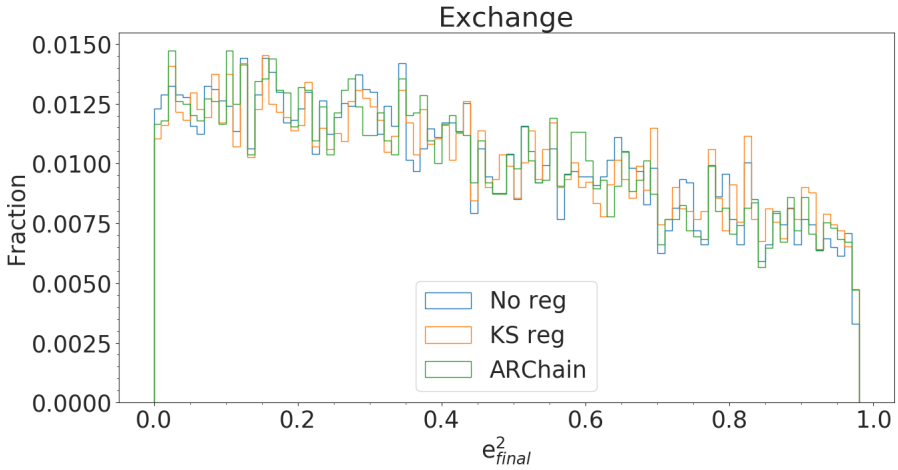

Figure 3.27: e^2 distribution for exchange

We plot the initial versus final eccentricity for flybys and exchanges separately with the number of binaries in each bin colour coded. The flybys are found in figure 3.28 where the top left panel shows the no regularization run, the top right panel shows the KS regularization run and the bottom panel shows the ARChain run. As for setup 2a (section 3.3.3) we have a bias towards $e_{init} = e_{final}$ for flybys where the interaction is weak and the eccentricity of the binary is not significant changed. We also have a bias towards high final eccentricity which indicates that our binaries, on a statistical scale, becomes more eccentric after a flyby.

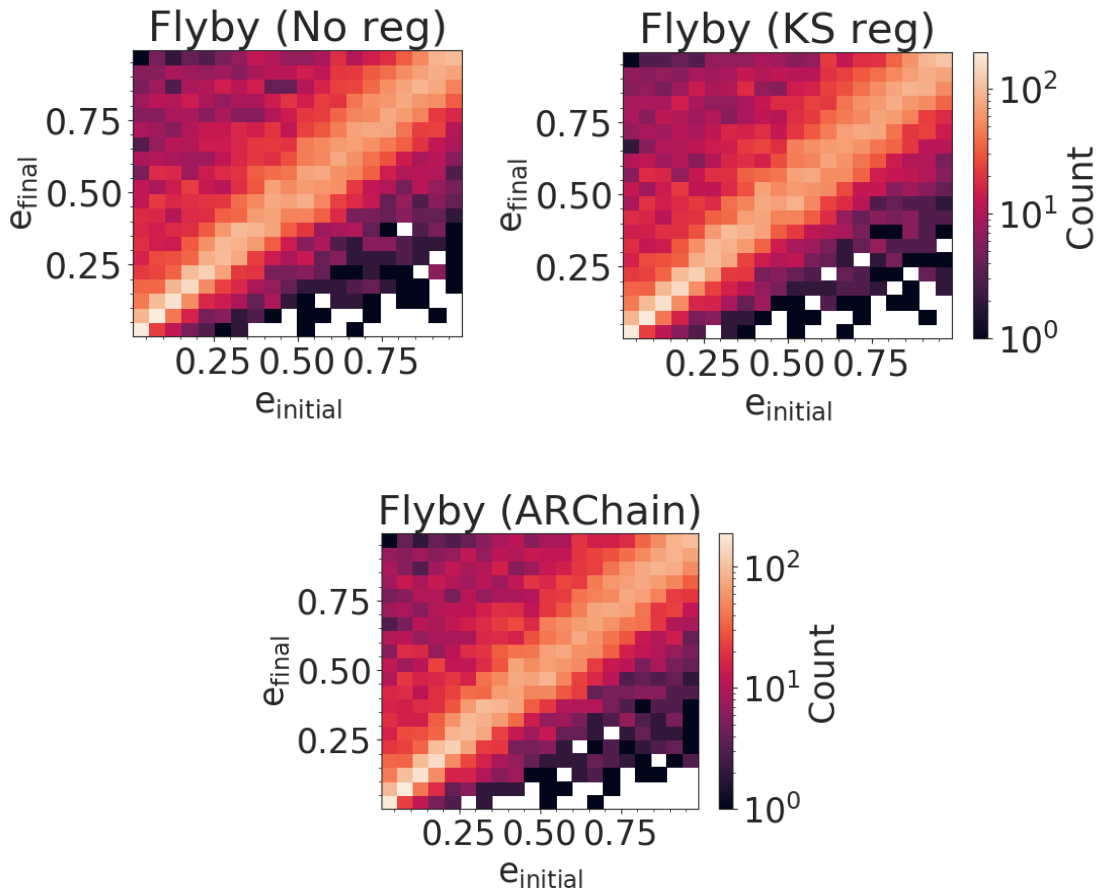

Figure 3.28: The initial and final eccentricity distribution for flybys with the initial eccentricity on the x-axis and the final eccentricity on the y-axis. The three panels show the distribution for flybys from the no regularization run (top left panel), the KS regularization run (top right panel) and the ARChain run (bottom panel)

In figure 3.29 we have the same plot but for exchanges where the top left panel shows the no regularization run, the top right plot shows the KS regularization run and the bottom plot shows the ARChain run. Here we also see the increase in eccentricity but generally the binaries are quite uniformly distributed, expect for low final eccentricities where we only find a small number of binaries. What we have discussed here, for both flybys and exchanges, are true for all three of our runs and we cannot see any significant differences between the runs.

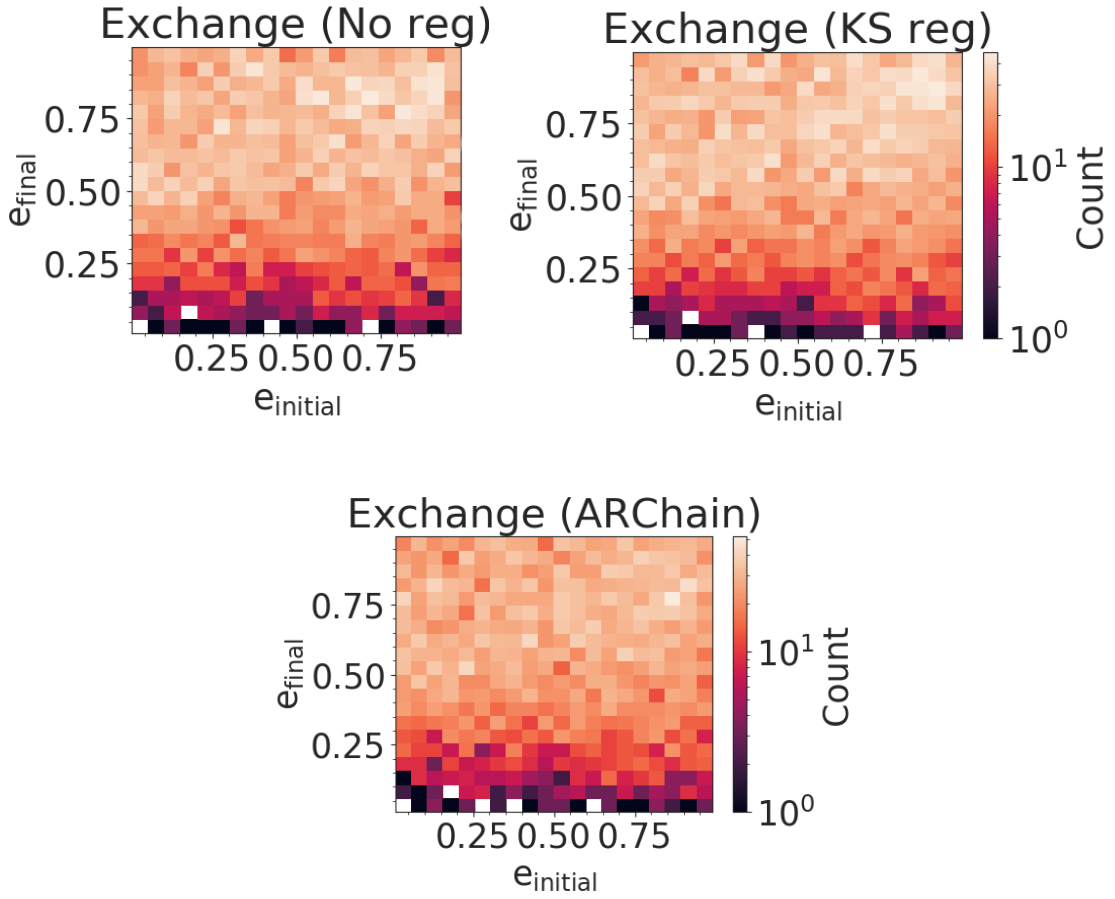

Figure 3.29: The initial and final eccentricity distribution for exchanges with the initial eccentricity on the x-axis and the final eccentricity on the y-axis. The three panels show the distribution for flybys from the no regularization run (top left panel), the KS regularization run (top right panel) and the ARChain run (bottom panel)

The final semi-major axis of the binary is plotted against the final eccentricity in figure 3.30 (for flybys) and figure 3.31 (for exchanges). For both figures we have the no regularization run in the top left panel, the KS regularization run in the top right panel and the ARChain run in the bottom panel. In the figures corresponding to the flybys we see that the semi-major axis of most binaries do not change much from the initial value, shown as a black line in the plots, and there seems to be a sharp upper limit on the semi-major axis at approximately the same value for all three runs. This upper limit can be explained by the fact that due to our fixed initial relative velocity we can only supply energy to widen the binary up to a specific value. For the exchanges we can see a similar upper limit on the semi-major axis but there is a wider spread on the semi-major axis than for the flybys. This is expected since we form a new binary rather than altering an existing one. The upper limit is also higher for the exchange case since we exchange in a 2 $M_\odot$ star which allow the binary to widen more than for a flyby. For all these plots, both for the flybys and exchanges, we see very small and insignificant differences between the three runs.

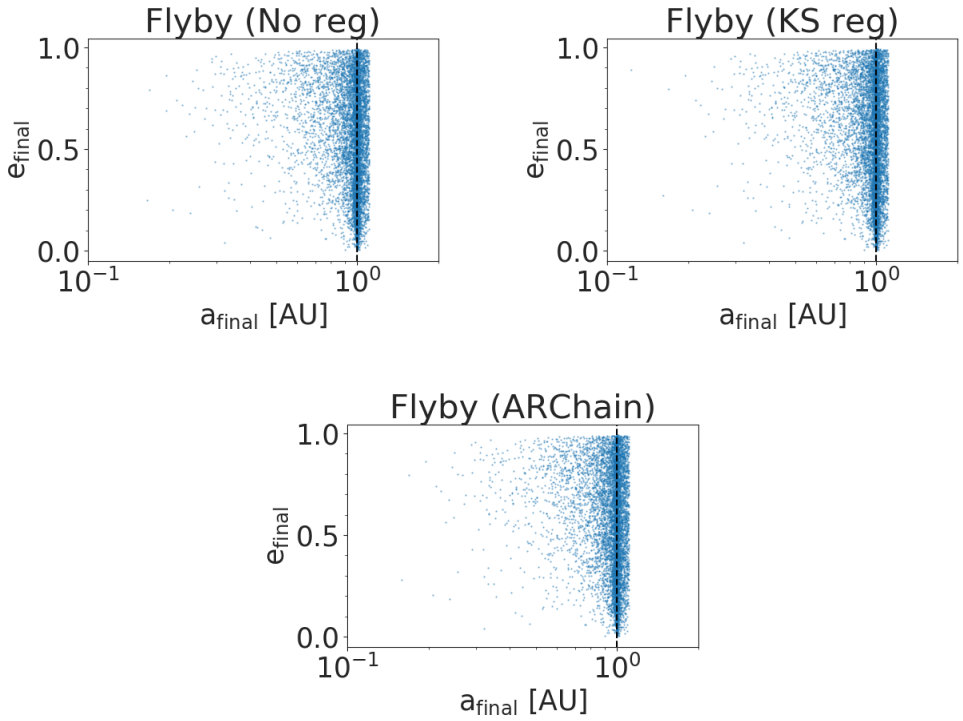

Figure 3.30: The final semi-major axis plotted against the final eccentricity of the binary for flybys. The black line corresponds to the initial semi-major axis of $a = 1$ AU

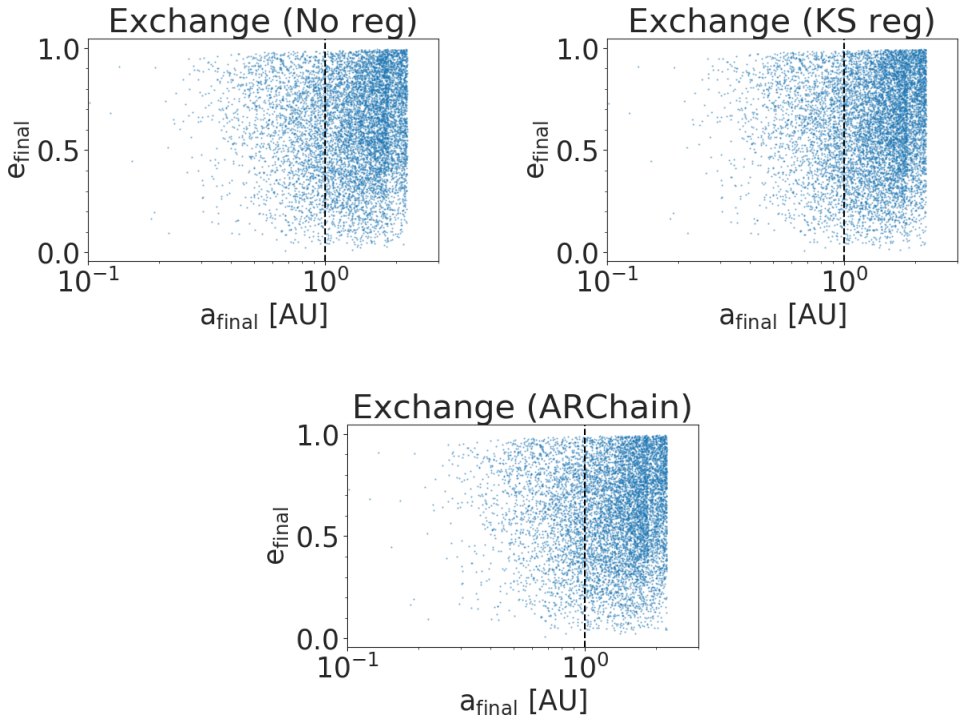

Figure 3.31: The final semi-major axis plotted against the final eccentricity of the binary for exchanges. The black line corresponds to the initial semi-major axis of $a = 1$ AU.

3.4.3 Minimum separation

The minimum separation (R_{min}) between any two objects in the interaction is quite interesting to investigate since we may find differences between how the difference regularization methods deal with very close interactions. We plot the R_{min} distribution for our three runs in figure 3.32 and limit the R_{min} to 10 $R_\odot$. We find no differences in the minimum R_{min} and in fact all three runs seems to cut off at $R_{min} = 2$ $R_\odot$, however, we see peaks in intervals of around 2 $R_\odot$. Due to this we plot our R_{min} up to 100 $R_\odot$ and find these peaks in the whole range. After looking into this we find that these peaks corresponds to the initial pericenter distance (r_{peri}) of the binary and exists due to a sampling issue. Since we set our initial binary semi-major axis to 1 AU and eccentricity in a range between 0 and 0.99 in steps of 0.01 our smallest pericenter distance we can get is:

$$r_{peri} = a(1 - e) = 1(1 - 0.99) = 0.01 \text{ AU} \approx 2.15 \text{ R}_\odot \tag{3.5}$$

and with our step size of 0.01 in the eccentricity, the steps in pericenter distance is 2.15 $R_\odot$. For flybys we expect quite a bit of distant flybys where the smallest distance between two objects will simply be the pericenter distance while for exchanges the stars has to get sufficiently close to each other in order to exchange energy and binary members and here the minimum separation will most likely not be the initial pericenter distance of the binary.

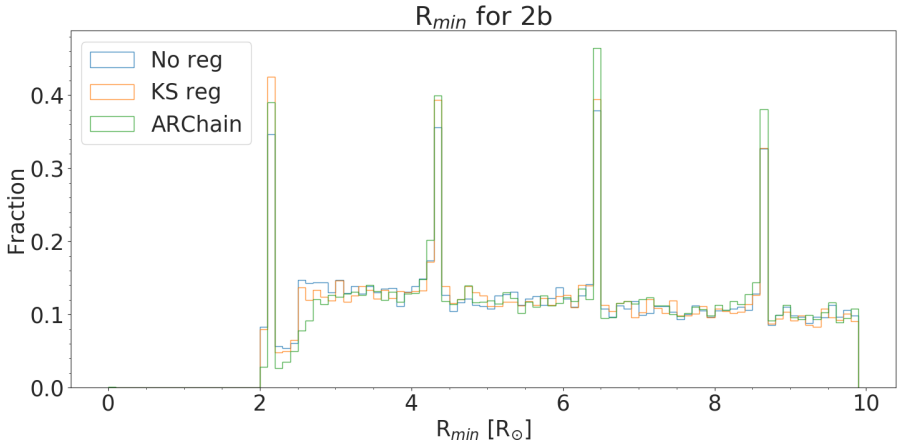

Figure 3.32: The minimum separation (R_{min}) distribution for setup 2b for all three runs between 0 and 10 $R_\odot$

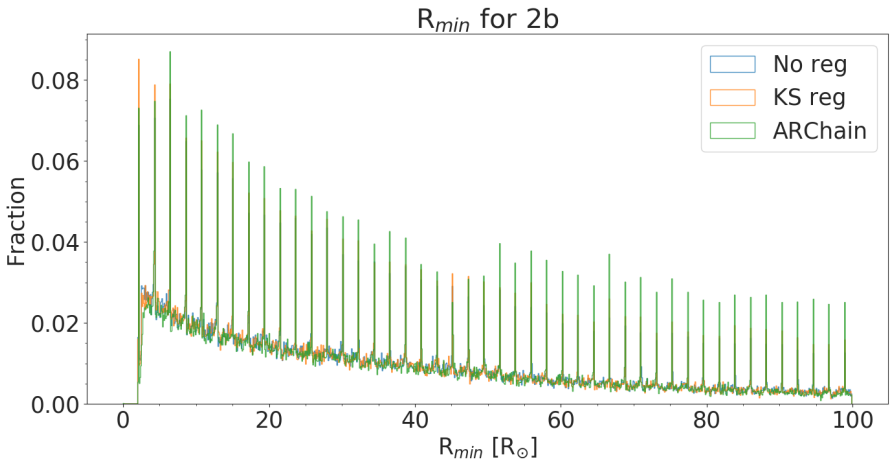

Figure 3.33: The minimum separation (R_{min}) distribution for setup 2b for all three runs between 0 and 100 $R_\odot$

3.4.4 Accuracy

We have previously discussed the impact of accuracy on the outcomes of dynamical interactions, see section 3.3.4 for more information. Since using the ARChain in Tsunami overrides the given accuracy we are only able to use Fewbody for these runs. This limits us to No regularization and KS regularization. For these two runs we set the accuracy to three different values: high accuracy where we set the absolute and relative accuracy to $A_{abs,rel} = 1e-15$, the default accuracy where $A_{abs,rel} = 1e-9$ and low accuracy where $A_{abs,rel} = 1e-5$.

3.4.4.1 Energy and angular momentum conservation

The energy conservation of the No regularization run is presented in figure 3.34 and of the KS regularization run in figure 3.35. The difference between the No regularization and KS regularization runs are quite similar with small differences. As expected we see a better energy conservation for higher accuracy. A study by Portegies Zwart & Boekholt (2014) found that if the energy conservation is better than 10%, the statistical differences between accuracies should be insignificant and from our two energy conservation plots we can see that the low accuracy run returned some interactions with an energy conservation worse than 10% for both the No regularization and KS regularization run. Because of this we remove all interactions where the energy conservation is worse than 10% and plot the distribution of outcomes, this is shown in figure 3.36, however we still see quite big differences between the runs with KS regularization and while there are differences for the no regularization runs they are significantly smaller than for the KS regularization runs which seems to indicate that the statistical distribution of outcomes is more sensitive to accuracy when KS regularization is used than when no regularization is used.

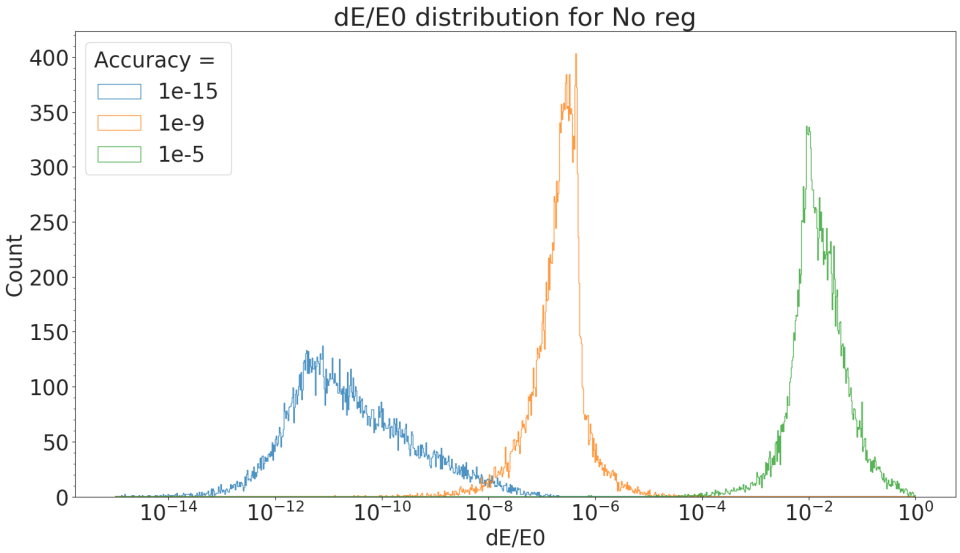

Figure 3.34: Distribution of energy conservation for the No regularization run of setup 2b where dE is the change in energy and $E0$ is the initial energy.

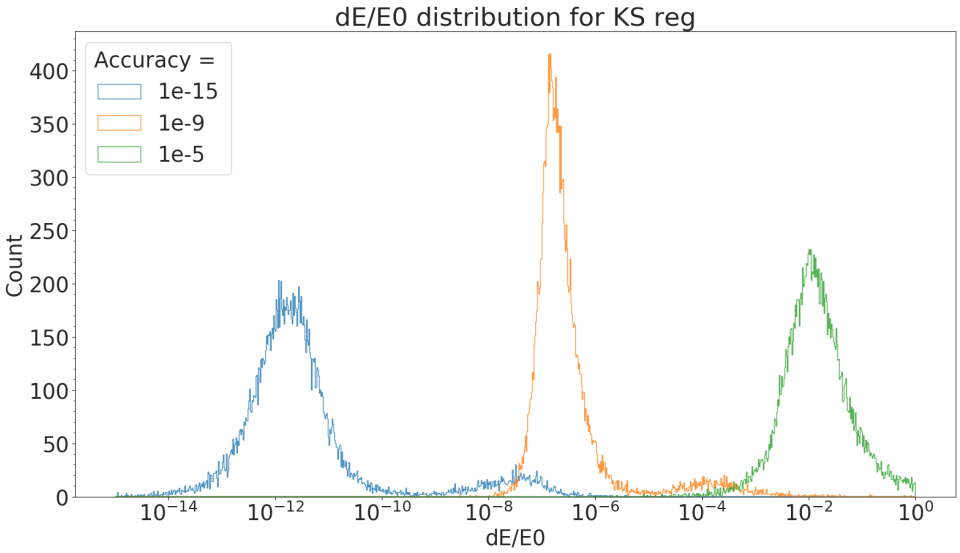

Figure 3.35: Distribution of energy conservation for the KS regularization run of setup 2b where dE is the change in energy and $E0$ is the initial energy.

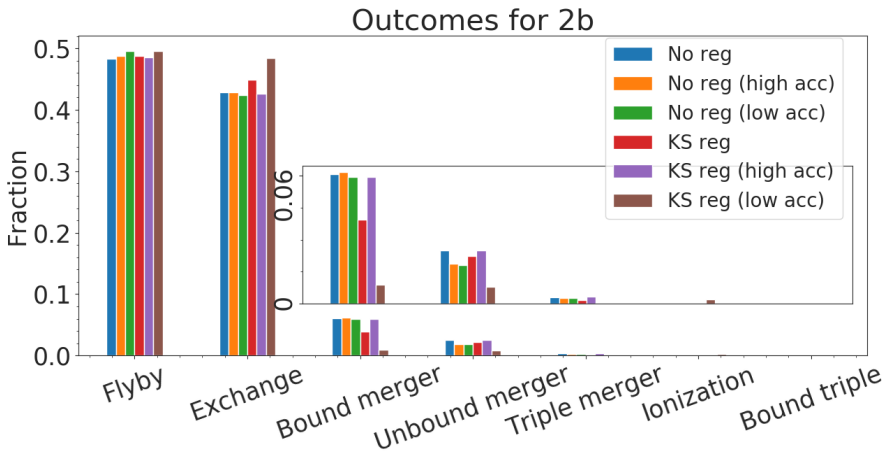

Figure 3.36: Distribution of outcomes for the No regularization and KS regularization runs of the 2b data set with different accuracies where all interactions with $dE/E0 > 0.1$ are removed.

In the Fewbody code, the angular momentum conservation is a measure of how well the integrator works and is obeying the laws of physics, and is therefore also an interesting parameter to look at. We plot the distribution of angular momentum conservation for no regularization and KS regularization for three different accuracies: high accuracy where we set $A_{abs,rel} = 1e-15$, the default accuracy which is $A_{abs,rel} = 1e-9$ and low accuracy where we set $A_{abs,rel} = 1e-5$. These plots are found shown in figure 3.37 for no regularization and figure 3.38 for KS regularization. We see that the angular momentum conservation is, on average, several orders of magnitude lower for a higher accuracy. It is difficult to specify a certain "threshold" where the integration can be considered incorrect or inaccurate since if only the outcome is observed the integrator may return the correct outcome even though the angular momentum conservation is bad and further analysis of both the energy and angular momentum conservation is needed.

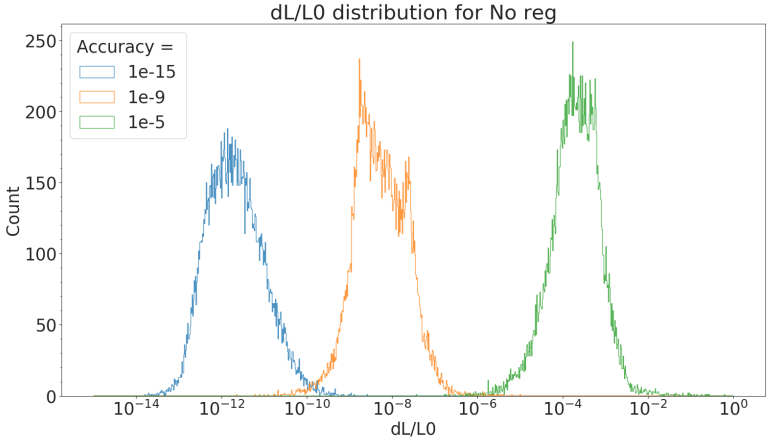

Figure 3.37: Distribution of angular momentum conservation for the No regularization run of setup 2b where dL is the change in angular momentum and $L0$ is the initial angular momentum.

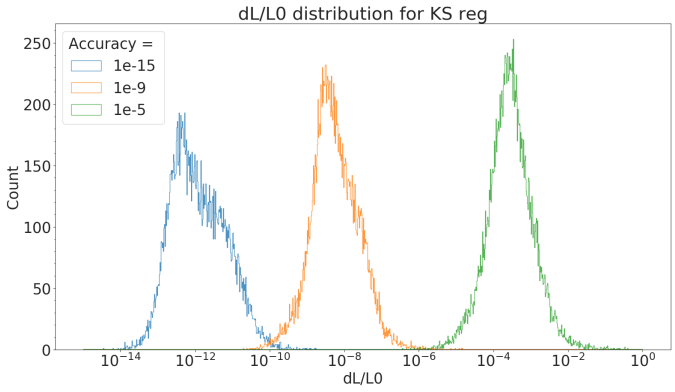

Figure 3.38: Distribution of angular momentum conservation for the KS regularization run of setup 2b where dL is the change in angular momentum and $L0$ is the initial angular momentum.

3.4.4.2 Outcomes

In figure 3.39 we show the distribution of outcomes of our different regularization methods and accuracies. We note that with no regularization for many outcomes we do not see a significant difference between the default, low and high accuracy runs, e.g. flybys and exchanges and for the outcomes where we do see a difference it is generally quite small. However, when using KS regularization the outcomes seems to be more affected by a change in accuracy. Looking at exchanges, we have fewer exchanges with a higher accuracy than default but more exchanges with a lower accuracy, and the opposite is true for bound mergers. We also see a small fraction of ionizations when using KS regularization and low accuracy. This is a problem since our relative velocity is fixed to 10 km/s which is not high enough to ionize the binary. Since we do not see any ionizations in another run we can link this to a too low value on the accuracy to get realistic and correct results. For the runs with low accuracy, for both no regularization and KS regularization, we get a few bound triples. These are probably also a result of too low accuracy and the code terminating the interaction too early and returning an incorrect outcome.

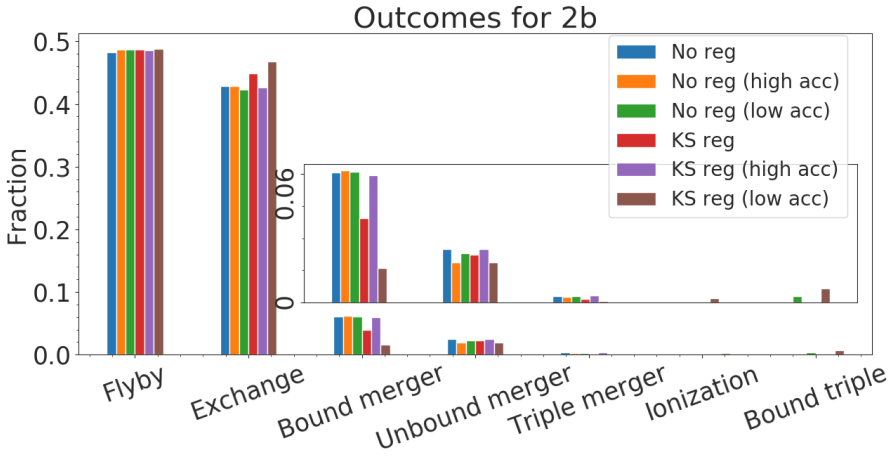

Figure 3.39: Distribution of outcomes for the No regularization and KS regularization runs of the 2b data set with different accuracies.

3.4.5 Point-masses

In this section we present the results of the runs of 2b when we treat the objects as point masses and thus excluding all outcomes which involves a merger. The distribution of outcomes is shown in figure 3.40 for 7 different runs: no regularization with default, high and low accuracy, KS regularization and default, high and low accuracy and ARChain with default accuracy. The default accuracy here is $A_{abs,rel} = 1e-9$, the high accuracy is $A_{abs,rel} = 1e-15$ and the low accuracy is $A_{abs,rel} = 1e-5$ where we always keep the absolute and relative accuracies equal for simplicity's sake.

For the two most common outcomes, flyby and exchange, all runs are quite similar with a few small differences. Since the velocity is set to 10 km/s in these runs (this is approximately $0.3v_c$) we should not expect any ionization, however, when using KS regularization and low accuracy we get a small fraction of ionization outcomes. Since this should not be possible we can relate this to the fact that the accuracy is too low for the integrator to return accurate and correct results. We also see an increase for bound triple for the same run as well as the no regularization run with low accuracy. Again we relate this to that the accuracy is too low for the integrator to accurately evolve the interaction.

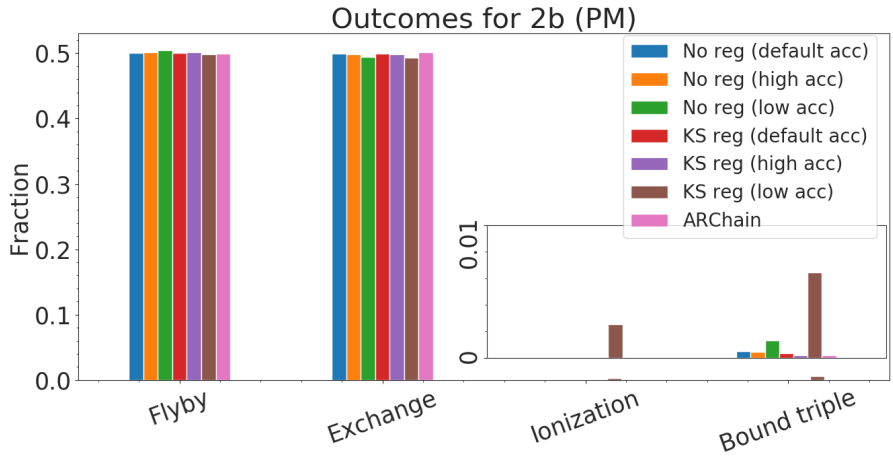

Figure 3.40: Distribution of outcomes for setup 2b where the objects are treated as point masses. Included in the plots are three runs with no regularization: default accuracy, high accuracy and low accuracy. For KS regularization the same accuracies are used and then the ARChain with default accuracy is also included.

We look at the impact parameter distribution for the different outcomes and accuracies with no regularization (figure 3.41) and KS regularization (figure 3.42). Here the outcomes are colour coded as: flyby in blue, exchange in orange, bound triple in green and ionization in red. The different accuracies are presented as different line styles where the high accuracy is a solid line, the default accuracy is a dashed line and the low accuracy is a dotted line. We can see that for both integration methods and all outcomes, all accuracies are very similar with insignificant differences. The largest difference is the existence of ionization for the low accuracy KS regularization run but, as previously discussed, this is most likely a result of too low accuracy leading to incorrect results.

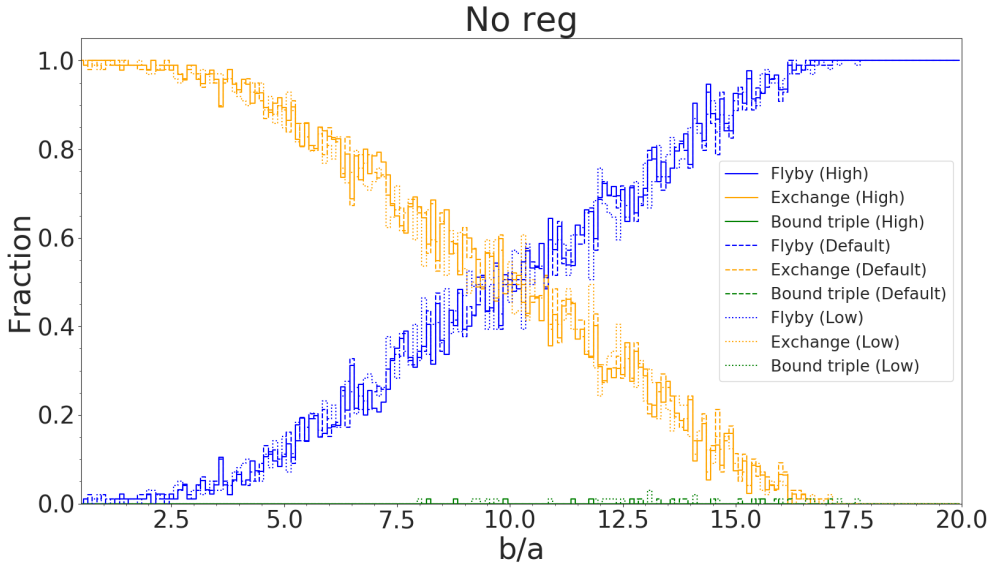

Figure 3.41: Distribution of the impact parameter for different outcomes and accuracies for the no regularization run.

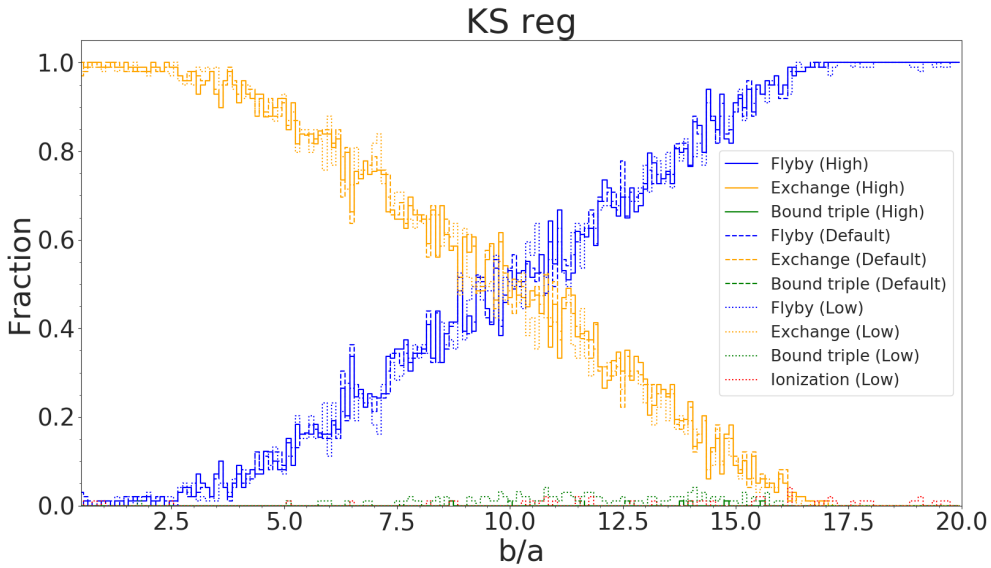

Figure 3.42: Distribution of the impact parameter for different outcomes and accuracies for the KS regularization run.

3.5 Interacting black holes

The 1 and 2 BH data sets extracted from MOCCA results (see section 2.5.3) are simulated in six different runs: No regularization, KS regularization, ARChain, PN terms, tides and PN terms + tides. The 3 BH set is simulated in four runs: No regularization, KS regularization, ARChain, PN terms since the addition of tides can lead to computational errors when dealing with tidal forces between 3 black holes. Section 3.5.3 contains the results from the 1 BH set, section 3.5.4 contains the results from the 2 BH set and section 3.5.5 contains the results from the 3 BH set.

3.5.1 Globular cluster simulation time of interaction

Since the cluster and the objects in the star changes over time we are interested in when in the evolution of the cluster our interactions involving black holes takes place. We plot the distribution of this interaction time in Myr in figure 3.43. We are more likely to have more interactions in the early life of the cluster since the most massive stars have evolved into black holes and segregated to the core where they dynamically interact with each other. As the cluster evolves, these dynamical interactions may eject black holes from the cluster which reduces their number with time and thus the number of interactions involving black holes decreases. This can be seen in the figure where we have a bias towards a higher number of interactions earlier in the lifetime of the clusters.

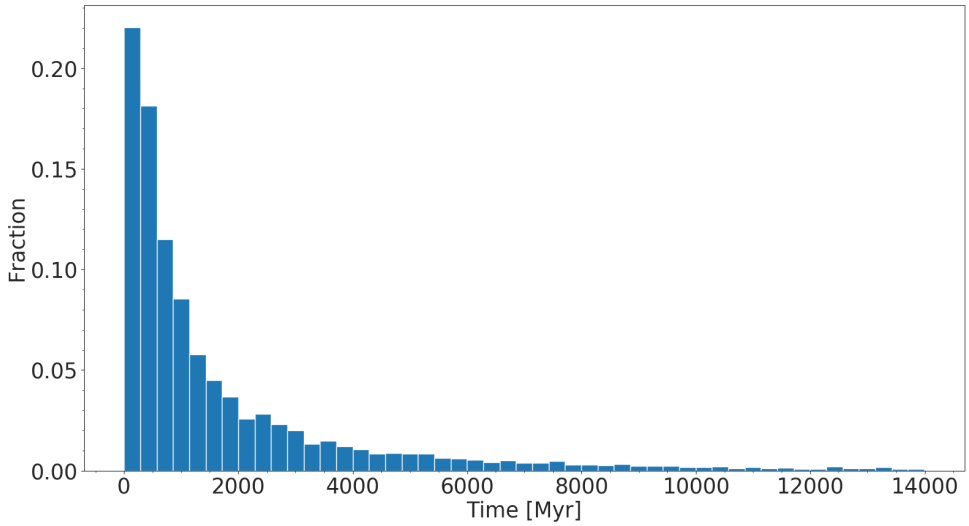

Figure 3.43: Distribution of GC simulation time when the interaction takes place.

3.5.2 Merger times

Two black holes in a isolated binary system may merge within a Hubble time if the semi-major axis is low and/or the eccentricity is high. If this is the case, the binary loses orbital energy through gravitational wave emission and may eventually merge. The merger time due to gravitational waves (t_{GW}) of a binary can be calculated with (Peters, 1964; Di Carlo et al., 2019):

$$t_{GW} = \frac{5}{256} \frac{c^5 a^4 (1-e^2)^{7/2}}{G^3 m_1 m_2 (m_1 + m_2)} \tag{3.6}$$

where c is the speed of light, a and e is the semi-major axis and eccentricity of the binary. G is the gravitational constant and m_1 and m_2 is the masses of the binary components. This merger time assumes that the binary does not interact with other objects which if we assume that the binary is ejected from the cluster after the interaction is a fair approximation. This merger time can be compared to the Hubble time ($t_H \approx 14$ Gyr) but we also compare it to four different times; 1 Myr, 100 Myrs, 1Gyr and 10 Gyrs. We assume that the binary components have equal mass ($m_1 = m_2 = 15$ M$_\odot$) and calculate the semi-major axis and eccentricity that corresponds to this binary merging within the previously mentioned timescales.

The following three sections present three different data sets from the MOCCA Survey Database I. They are split into three subsections according to the number of black holes in the interaction.

3.5.3 1 BH and 2 stars

The first set that is extracted from the MOCCA Survey Database I contains 100,000 interactions with 1 black hole and 2 stars. For the black holes the minimum mass is 20.5 $M_\odot$, the maximum mass is 100 $M_\odot$ and the average mass is 21 $M_\odot$, while for the stars the average is 0.9 $M_\odot$. The distribution of outcomes from this set is shown in figure 3.44. We see that for flybys all runs are very similar except for the ARChain run where we see approximately 2% less interactions, however, for exchanges we see approximately 2% more interactions for the ARChain run than for the No regularization, KS regularization run and the PN terms run and approximately 1% more than the Tides and PN + tides run. For ionization, all runs are quite similar and are within 1% of each other. For all outcomes involving a merger we see significant differences; the No regularization, KS regularization and PN terms runs see many more mergers than the other runs while the ARChain, Tides and PN + tides run return significantly more bound triples.

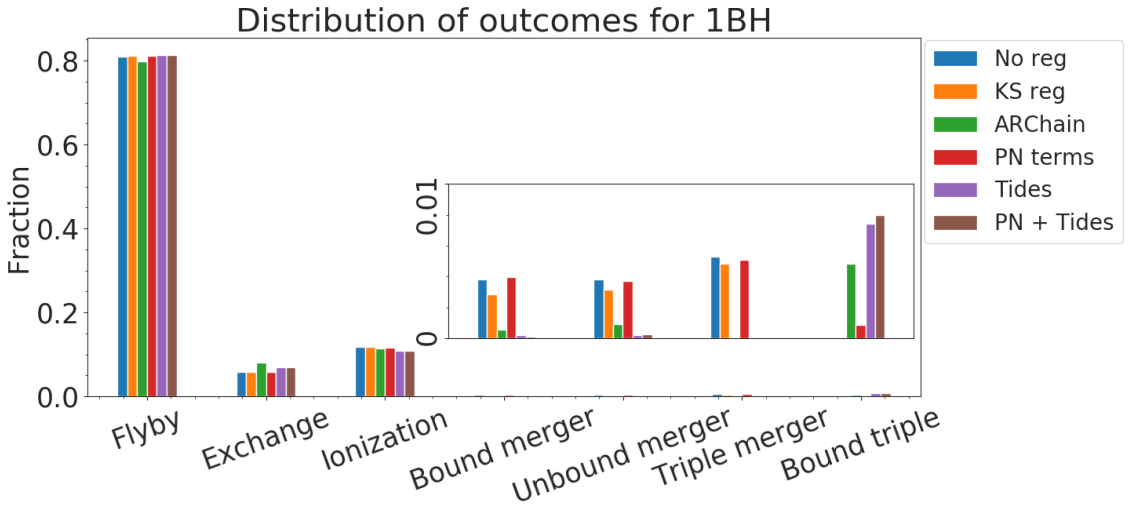

Figure 3.44: Distribution of outcomes for the 1 black hole data set extracted from star cluster simulations reported in MOCCA Survey Database I

3.5.4 2 BHs and 1 star

This subsection contains the results from the second set of 100,000 interactions that is extracted from the MOCCA Survey Database I which contains 2 black holes and 1 star in each interaction. The maximum mass of black holes we consider is 100 $M_\odot$ and the average mass is 20 $M_\odot$, while for the stars the average mass is 0.68 $M_\odot$. The distribution of outcomes for the these runs can be seen in 3.45. We find that for all runs are very similar for most outcomes with a few outliers: The ARChain run and the PN terms run see an increase of approximately 2.5% in exchanges compared to the other runs. The two runs involving tides see a significant decrease in bound mergers where the number of bound mergers are 2.5 times higher in the PN terms run than in the Tides run and 42 times higher in the PN terms run than in the PN + tides run. We also see an increase in bound triples for the two runs where tides are used and the PN + tides run have approximately 5 times the number of bound triples compared to the PN terms run. This seems to indicate that the addition of tides favour the formation of bound triple systems and disfavour the merging of objects.

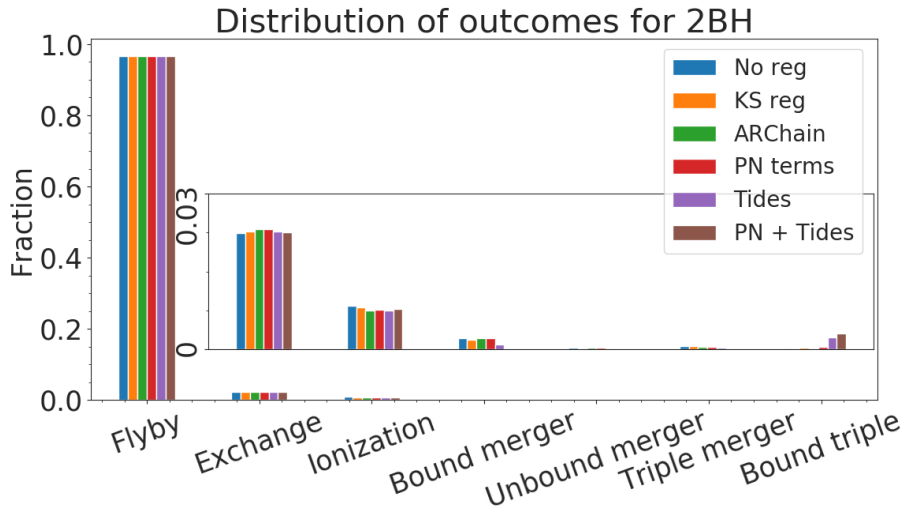

Figure 3.45: Distribution of outcomes for the 2 black hole data set extracted from star cluster simulations reported in MOCCA Survey Database I

3.5.4.1 Energy and angular momentum conservation (2 BHs)

The energy and angular momentum conservation is an indication of how well the integrator works. The energy conservation is plotted in figure 3.46 for all of our runs. We see that the ARChain run, Tides run and PN + tides run return the best average energy conservation while the addition of PN terms seems to make the energy conservation worse by 4 to 5 orders of magnitude compared to the ARChain run, however, if the PN terms and tides are used together the average energy conservation improves by 4 to 5 orders of magnitude and becomes very similar to the ARChain run. The worst average energy conservation is obtained from the No regularization run with almost 6 orders of magnitude worse than the ARChain run. The KS regularization run is slightly better than the No regularization run and the average energy conservation is approximately 1 order of magnitude better than the No regularization run.

The angular momentum conservation is plotted in figure 3.47. Similarly to the energy conservation, the ARChain run, Tides run and PN + tides run are very similar and indistinguishable. The PN terms run gives 3 to 4 orders of magnitude worse angular momentum conservation compared to the ARChain run and the average angular momentum is similar to the average angular momentum conservation of the No regularization and KS regularization runs. For both the energy

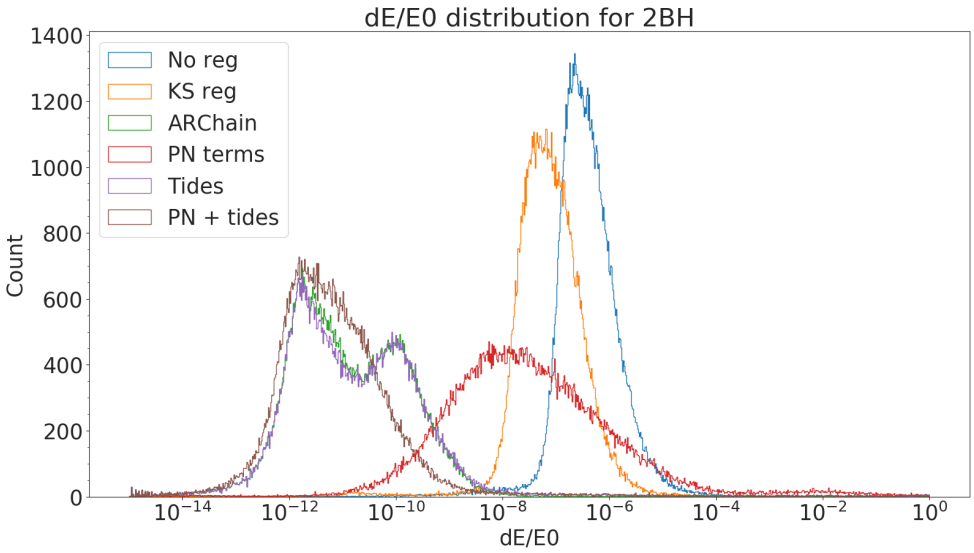

Figure 3.46: Distribution of the energy conservation for the 2 black hole data set extracted from star cluster simulations reported in MOCCA Survey Database I.

and angular momentum conservation we can see that the No regularization and KS regularization is significantly worse on conserving the parameters than the ARChain and the additional processes of the ARChain, with the exception when PN terms are used without tides. When PN terms is used without tides it seems like the energy and angular momentum is significantly worsened and comparable to the No regularization and KS regularization runs.

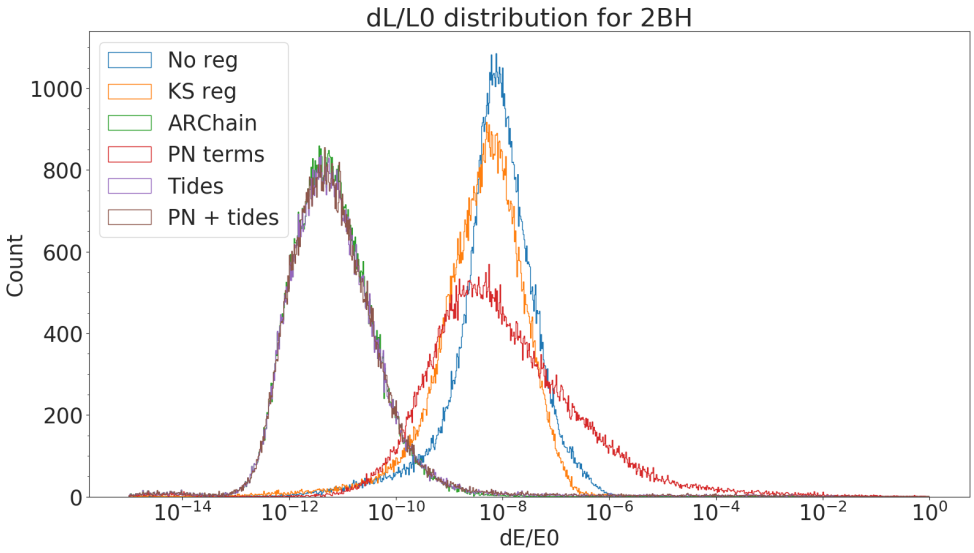

Figure 3.47: Distribution of the angular momentum conservation for the 2 black hole data set extracted from star cluster simulations reported in MOCCA Survey Database I.

3.5.4.2 Merger times of black hole binary (2 BHs)

The time is takes for a black hole binary to merge is dependent on the binary semi-major axis, eccentricity and component masses as discussed in section 3.5.2. Here we plot the semi-major axis distribution against the eccentricity both before and after the interaction and include lines which corresponds to the semi-major axis and eccentricity which would cause a black hole binary where each component has mass 15 $M_\odot$ within 1 Myr, 100 Myrs, 1 Gyr and 10 Gyrs according to equation 3.6. Figure 3.48 shows the semi-major axis and eccentricity before (blue dots) and after (orange dots) the interaction, interactions that lie beneath these lines would merger within the respective time. In table 3.3 we present the number of black hole binaries that merge within 1 Myr, between 1 Myr and 100 Myrs, between 100 Myrs and 1 Gyr and between 1 Gyr and 10 Gyrs. We find that the ARChain run, PN run and Tides run do not significantly alter the number of binaries in any of the bins, however, the PN + tides run decrease the number of mergers within 1 Myr by approximately 15 times, between 1 Myr and 100 Myr by approximately 4 times, between 100 Myr and 1 Gyr by approximately 2 times and between 1 Gyr and 10 Gyrs by approximately 1.5 times. This may be due to the additional terms circularising the binaries and thus increasing the pericenter distance. Since any non-negligible emission of gravitational waves require close passage between the binary components, a high eccentricity leads to a smaller pericenter distance and thus closer passages which in turn emit stronger gravitational waves and dissipate more orbital energy. If the combination of PN terms and tides circularise the binaries this may explain why we see this significant decrease in mergers for all time bins considered.

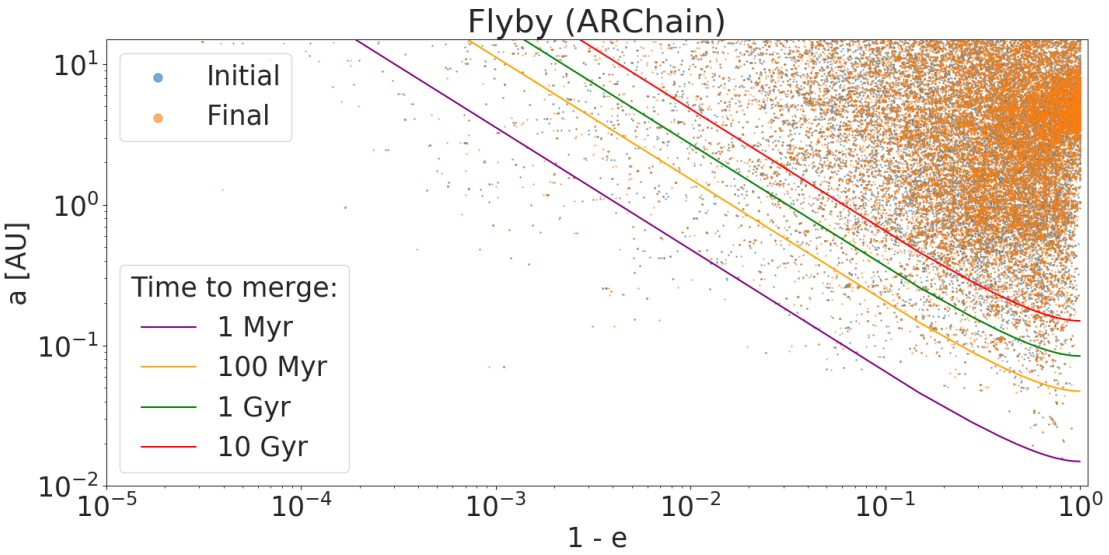

Figure 3.48: Distribution of semi-major axis and eccentricity, initially (blue dots) and after the interaction (orange dots) for flybys. The lines corresponds to different merger times of a black hole binary with masses 15 $M_\odot$.

BBH-star interactions

	<1 Myr	1 Myr - 100 Myr	100 Myr - 1 Gyr	1 Gyr - 10 Gyr
Initial	153	400	590	1078
ARChain	157	416	598	1082
PN	152	403	611	1089
Tides	154	398	567	1052
PN + Tides	151	413	569	1050

Table 3.3: Number of black hole binaries that merge within less than 1 Myr, between 1 Myr and 100 Myrs, between 100 Myrs and 1 Gyr and between 1 Gyr to 10 Gyrs due to emission of gravitation wave radiation. This table reports the cases where the binary encountered a star and the interactions resulted in a flyby.

3.5.5 3 BHs

The final data set extracted from the MOCCA Survey Database I contains 100,000 binary-single interactions where all objects are black holes. The minimum mass is 3 $M_\odot$, the maximum mass is 98 $M_\odot$ and the average mass is 16 $M_\odot$. Since tidal effects should not significantly affect black holes and the addition of tidal effects may lead to numerical errors when all objects in the interaction are compact objects, we do not include tidal effects in these runs. The distribution of outcomes from these runs are shown in figure 3.49 where we can see that flybys are the most likely outcome and here all runs are very similar. The number of exchanges differ slightly between the runs and the ARChain run and PN terms run where we get an approximately 1% increase over the No regularization run and KS regularization run. For ionizations we see that the No regularization run and KS regularization run are quite similar while the number of ionizations in the ARChain run and PN terms run are approximately 12% lower than than No regularization run and the KS regularization run. The PN terms run returns a peak in the number of bound triples where the number is approximately 40 times higher than for the other runs and the number of bound mergers are very low (1 for No regularization and ARChain and 0 for KS regularization and PN terms) but we include it in the figure for completion. From this distribution we can see that for binary-single interactions involving 3 black holes, the regularization method makes a small difference for exchanges and a fairly significant difference for ionizations which may indicate that the ARChain is better at conserving our binaries while the other two regularization methods dissolve them more frequently. The most significant difference is in the number of bound triples where the PN terms drastically increase the number of outcomes. Since a binary-single interaction needs to dissipate some energy to form a triple system this can be explained by the energy dissipation for gravitation wave emission included in the PN terms.

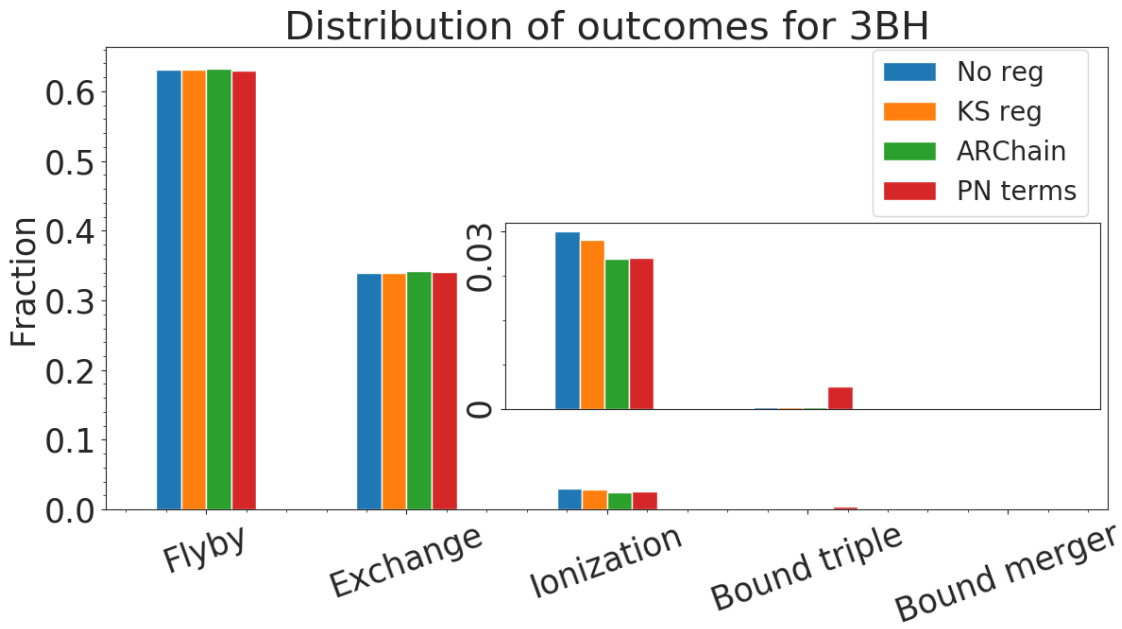

Figure 3.49: Distribution of outcomes for the 3 black hole data set extracted from star cluster simulations reported in MOCCA Survey Database I

3.5.5.1 Merger times of black hole binary (3 BHs)

We create two data sets out of our initial 3 BH data set where we set an upper limit of 0.95 on the eccentricity in one set and set an lower limit of 0.95 on the eccentricity in the other set. We also set an upper limit of 10 AU on the initial semi-major axis. Both sets contain 20,000 interactions that are simulated with 5 different randomised orientation angles for a total of 100,000 interactions. We plot the eccentricity versus the semi-major axis, initially and after the interaction, for flybys in figure 3.50 and 3.52 where figure 3.50 shows the set with high eccentricity and figure 3.52 shows the set with low eccentricity. In both figures the left panel shows the ARChain run and the right panel shows the PN terms run. The merger time of a isolated binary due to gravitational wave radiation can be estimated by equation 3.6. Using this equation we find the values of semi-major axis and eccentricity which makes a binary consisting of two black holes of 15 $M_{\odot}$ to merge within 1 Myr, 100 Myrs, 1 Gyr and 10 Gyrs and include these relations in figures 3.50, 3.50, 3.52 and 3.53 as solid, coloured lines. We see that due to the interaction, the eccentricities of the binaries are spread out. In figure 3.50 where we start with a high initial eccentricity and only consider flybys, approximately 65% of binaries decreases in eccentricity and circularise due the interaction while 35% increases in eccentricity. When considering exchanges in figure 3.51 approximately 94% of the final binaries have an eccentricity lower than the eccentricity of the initial binary and approximately 6% increase in eccentricity. All these fractions are the same down to the third decimal for both runs.

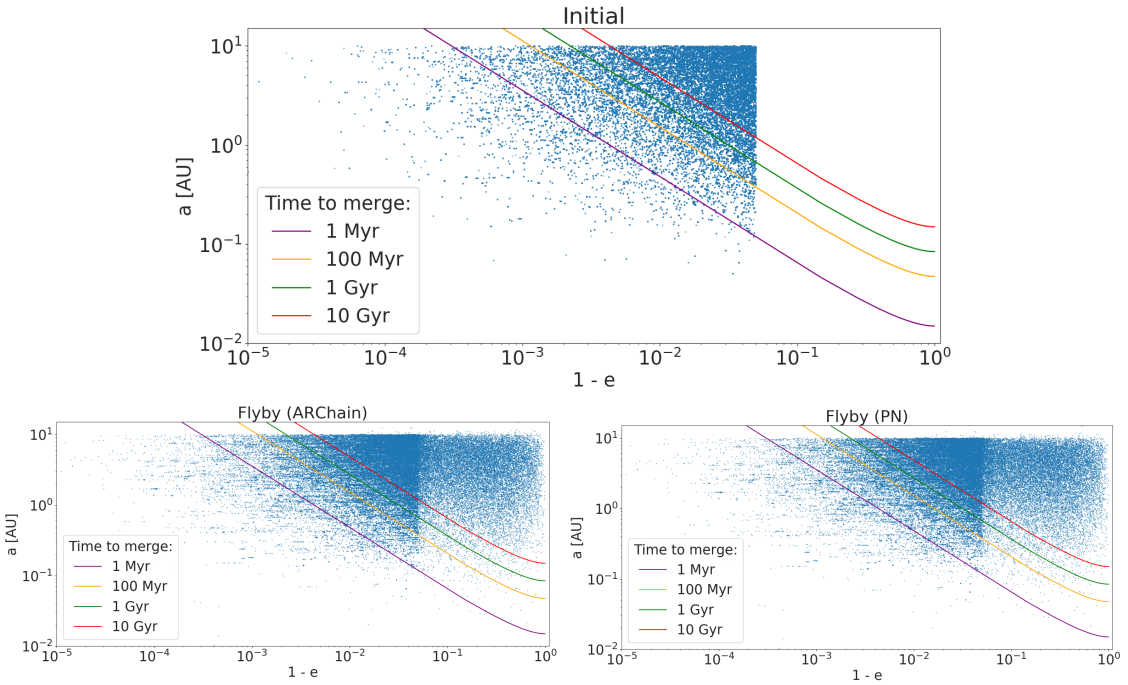

Figure 3.50: The eccentricity plotted against the semi-major axis of the binary. We include lines to represent four different merger times for a binary of two 15 $M_\odot$ black holes. These plots show interactions where the initial eccentricity is greater than 0.95 and the interaction resulted in a flyby. The top panel shows the initial parameters while the bottom panels shows the final parameters for the ARChain run (bottom left panel) and the PN terms run (bottom right panel).

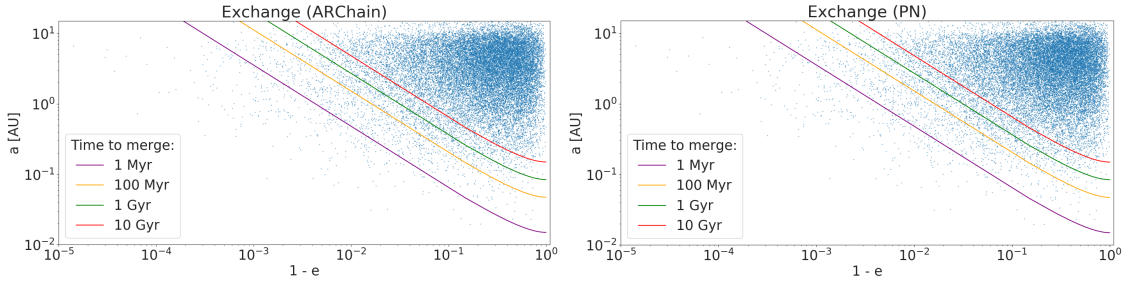

Figure 3.51: The eccentricity plotted against the semi-major axis of the binary. We include lines to represent four different merger times for a binary of two 15 $M_\odot$ black holes. These plots show interactions where the initial eccentricity is greater than 0.95 and the interaction resulted in an exchange. The top panel shows the initial parameters while the bottom panels shows the final parameters for the ARChain run (bottom left panel) and the PN terms run (bottom right panel).

For the runs with low initial eccentricity that results in a flyby (figure 3.52), we see an eccentricity increase in approximately 56% of the binaries and a decrease in 44%. For exchanges (figure 3.53) approximately 70% of the binaries after the interaction have an eccentricity higher than the initial binary and 30% interactions results in a binary with lower eccentricity than the initial binary. The differences between the runs are smaller than 1% and negligible.

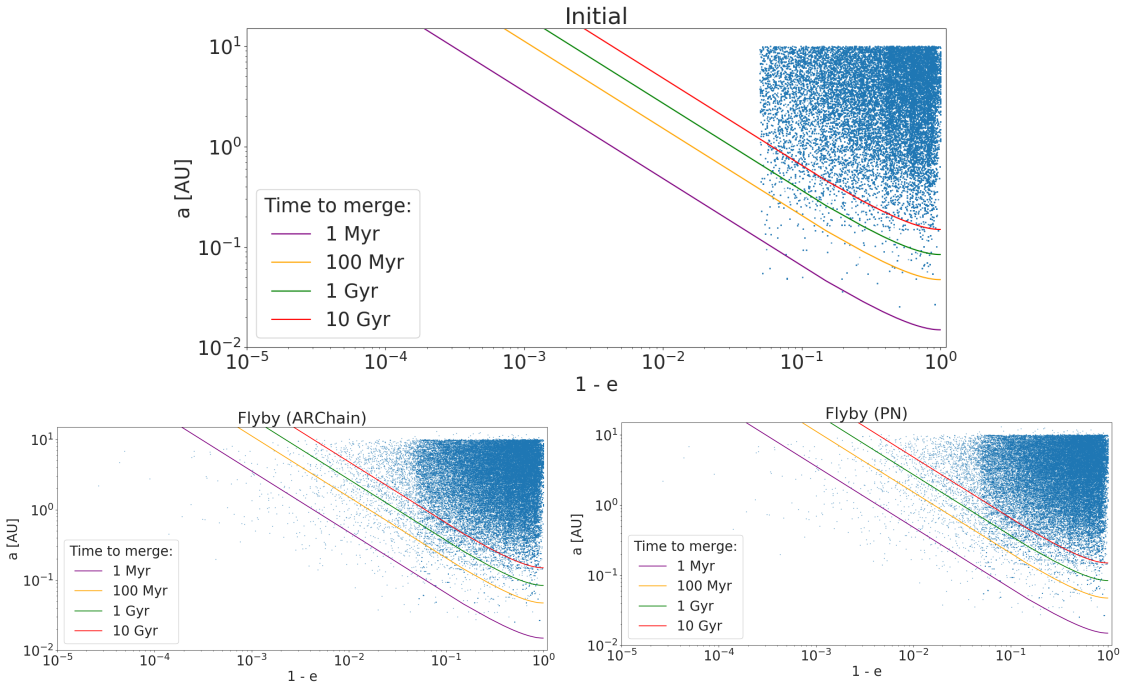

Figure 3.52: The eccentricity plotted against the semi-major axis of the binary. We include lines to represent four different merger times for a binary of two 15 $M_\odot$ black holes. These plots show interactions where the initial eccentricity is greater than 0.95 and the interaction resulted in a flyby. The top panel shows the initial parameters while the bottom panels shows the final parameters for the ARChain run (bottom left panel) and the PN terms run (bottom right panel).

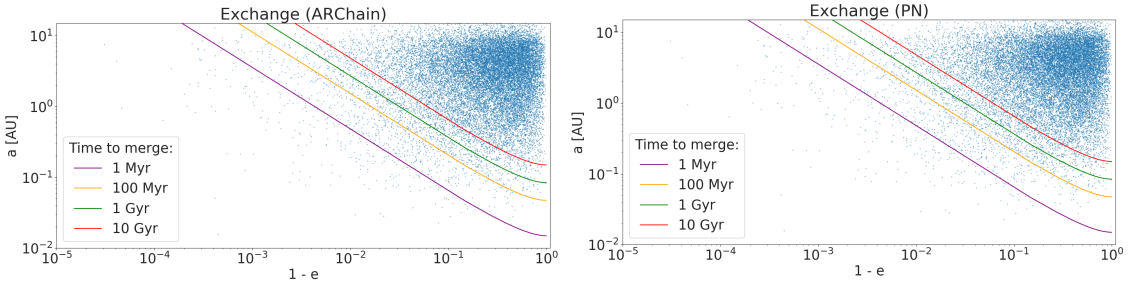

Figure 3.53: The eccentricity plotted against the semi-major axis of the binary. We include lines to represent four different merger times for a binary of two 15 $M_\odot$ black holes. These plots show interactions where the initial eccentricity is greater than 0.95 and the interaction resulted in an exchange. The left panel shows the results from the ARChain run while the left panel shows the results from the PN terms run.

We use equation 3.6 to calculate the initial and final merger times for all binaries where interaction resulted in a flyby and plot them in figure 3.54 where $e_{initial} > 0.95$ (left panel) and $e_{initial} < 0.95$ (right panel) and indicate the Hubble time (approximately 14 Gyr) as a black dashed line. For the set with high initial eccentricity we see a decrease of approximately 35% in the number of binaries that would merge within one Hubble time after the interaction compared to initially. However, for the set with low initial eccentricity we see an increase of 22.5%. The inclusion of PN terms did not significantly change these numbers and the differences between the ARChain run and the PN terms run are below 1% for both sets.

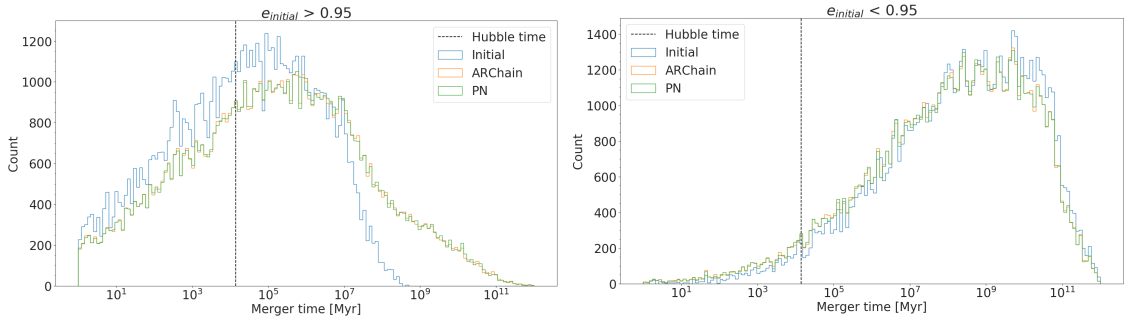

Figure 3.54: Distribution of black hole binary merger time due to gravitational wave emission. The left panel shows the interactions limited to $e_{initial} > 0.95$ and the right panel shows the interactions limited to $e_{initial} < 0.95$.

We create four time bins and count the number of binaries that merge within each bin. The bins are: less than 1 Myr, between 1 Myr and 100 Myrs, between 100 Myrs and 1 Gyr and between 1 Gyr to 10 Gyrs and we present the results in table 3.4 (high initial eccentricity) and table 3.5 (low initial eccentricity). For the high initial eccentricity case the ARChain run and PN terms run are very similar in all bins. The number of mergers decreases for both run after the interaction compared to the initial values for all time bins. In the first bin ($t_{GW} < 1$ Myr) there is approximately a 40% decrease, in the second bin (1 Myr $< t_{GW} <$ 100 Myr) there is a decrease of approximately 32%, in the third bin (100 Myr $< t_{GW} <$ 1 Gyr) there is approximately a 28% decrease and in the final bin (1 Gyr $< t_{GW} <$ 10 Gyr) there is approximately25 a % decrease.

3 BH interactions with $e > 0.95$ and $a < 10$ AU

	<1 Myr	1 Myr - 100 Myr	100 Myr - 1 Gyr	1 Gyr - 10 Gyr
Initial	5331	10252	9184	11141
ARChain	3798	7743	7176	8968
PN	3810	7740	7157	8939

Table 3.4: Number of binaries that merge within less than 1 Myr, between 1 Myr and 100 Myrs, between 100 Myrs and 1 Gyr and between 1 Gyr to 10 Gyrs due to emission of gravitation wave radiation. This table reports the cases where the binary encountered a black hole, the interactions resulted in a flyby, the initial eccentricity is higher than 0.95 and the semi-major axis is lower than 10 AU.

clearpage With the same time bins we count the number of mergers within each bin for the case with low initial eccentricity and present that in table 3.5. For the high initial eccentricity case we saw a decrease in the number of mergers within each time bin, however, when we start with a low initial eccentricity we see an increase in the number for each time bin. For the first bin ($t_{GW} < 1$ Myr) there is an increase of almost 8 times, in the second bin (1 Myr $< t_{GW} <$ 100 Myr) the increase is close to 2.5 times, in the third bin (100 Myr $< t_{GW} <$ 1 Gyr) there is an increase of almost 2 times and in the final bin (1 Gyr $< t_{GW} <$ 10 Gyr) there is approximately a 36%

increase. For all bins we have approximately the same number of mergers in both the ARChain run and PN terms run and the differences are negligible.

3 BH interactions with $e < 0.95$ and $a < 10$ AU

	<1 Myr	1 Myr - 100 Myr	100 Myr - 1 Gyr	1 Gyr - 10 Gyr
Initial	24	246	585	1332
ARChain	188	604	949	1819
PN	181	595	954	1781

Table 3.5: Number of binaries that merge within less than 1 Myr, between 1 Myr and 100 Myrs, between 100 Myrs and 1 Gyr and between 1 Gyr to 10 Gyrs due to emission of gravitation wave radiation. This table reports the cases where the binary encountered a black hole, the interactions resulted in a flyby, the initial eccentricity is lower than 0.95 and the semi-major axis is lower than 10 AU.

Chapter 4

Discussion

4.1 Regularization & Outcomes

The implementation of a regularization method is important in N-body codes when dealing with close encounters. In our runs we had No regularisation, KS regularisation and ARChain. We found that for certain initial setups the choice of regularization method does make a difference on a statistical scale, such as in figure 3.6 where we have 3 stars, the addition of KS regularization results in 3% more exchanges and less mergers. Fregeau et al. (2004) discussed that the use of KS regularization within fewbody requires extra effort to find instances of mergers during the interaction since the pericentre value is not neccessarily resolved by the integrator and they do not implement the appropriate technique needed for properly detecting collisions with their KS regularization option.

When including black holes in the interactions the effects of regularization seems to depend on the number of black holes in the interaction. For the case with 1 BH, figure 3.44, we see no significant difference between No regularization and KS regularization but we do see an increase in exchanges and a decrease in flybys for the ARChain run. In the interactions involving 1 BH, the masses of the interacting stars can be quite different and it has been shown in previous works that ARChain is better at handling interactions in which mass ratio of the interacting objects is large (Mikkola, 2008). For the 2 BH and 3 BH case, figures 3.45 and 3.49, we do not see any significant differences between the different regularization schemes. This indicates that the choice of regularization method is more important for the outcomes on a statistical scale when there are stars rather than compact objects in the interaction or when the mass ratio between interacting stars is large.

4.2 Influence of accuracy on results

The accuracy of the integrator can have an impact on the outcomes on the interactions as seen in figure 3.22 for setup 2a and figure 3.39 for setup 2b. We also found that a higher accuracy results in better energy and angular momentum conservation as expected. Choosing an accuracy value has to be done carefully since a too low value may lead to inaccurate results (see figure 3.39) but a too high value may lead to unnecessarily high computation times as we will see in section 4.2.1. The problem with accuracy has been investigated previously and in Boekholt et al. (2020), they found that for some interactions an accuracy smaller than the Plank length is required to reverse the interaction, i.e. take the final state vector, reverse time and perform the interaction again to obtain the initial state vector. However, Portegies Zwart & Boekholt (2014) claims that as long as the energy conservation of the interaction is better than 10% the accuracy does not make a difference on a statistical scale.

We investigated this in section 3.4.4 and figure 3.36 where we remove all interactions with energy conservation worse than 10% and plot the outcomes for the different accuracies. We find that even though we have removed the interactions with bad energy conservation, we still see non-negligible differences between the runs. To further investigate this, we plot the outcomes of the interactions with bad energy conservation (we set the limit on "bad" energy conservation to 10%) in figures 4.1 (for setup 2a) and 4.2 (for setup 2b). We find that for setup 2a, there are some interactions with bad energy conservation even for the high accuracy runs of No regularisation and KS regularisation. However, the number of bad energy conservation interactions are quite low for the high accuracy runs are low: 762 out of 119,000 for the no regularisation case where they mostly result in Flybys or Exchanges. For the KS regularisation run with high accuracy we find 140 out of 119,000 interactions with bad energy conservation and they mostly result in mergers. Since Fewbody uses a sticky star approximation during mergers (as soon as two stars overlap they merge instantly) this may lead to bad energy conservation. For setup 2b we only find interactions with bad energy conservation for the two runs with low accuracy. The most notable difference between the runs is that for 2a it is uniformly distributed within $0.1v_c$ and $1.2v_c$ while for for 2b the initial relative velocity is fixed to 10km/s (approximately $0.3v_c$). The average v_∞ in setup 2a is $0.65v_c$ while for the bad energy conservation cases of 2a the average v_∞ is $1.0v_c$. This indicates that a higher initial relative velocity is more probable to lead to bad energy conservation. Since we are more likely to have flybys for high relative velocity this is most likely the reason why we see more flybys for the bad energy conservation cases in 2a than 2b.

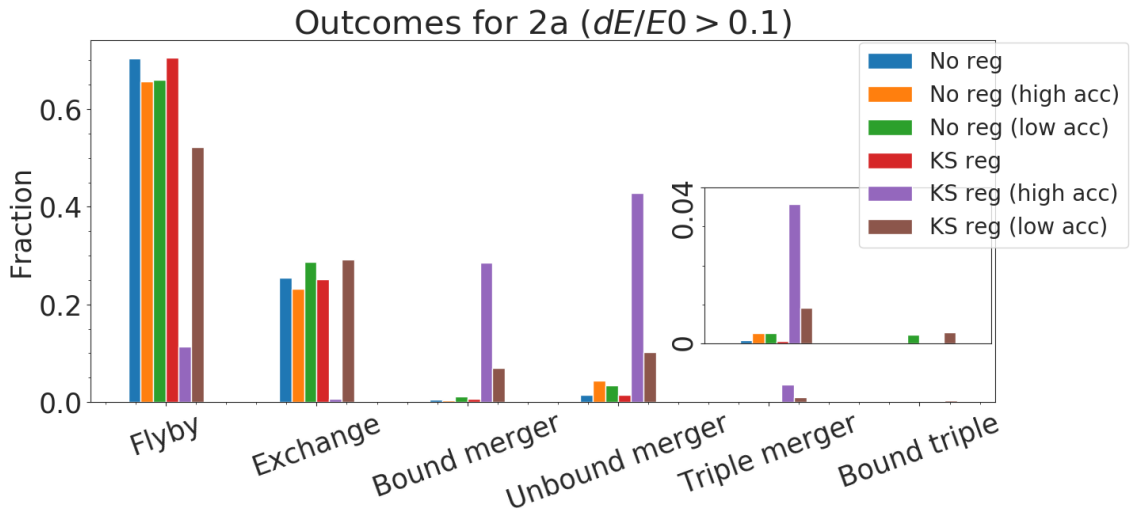

Figure 4.1: Distribution of outcomes for setup 2a where the energy conservation is worse than 10%.

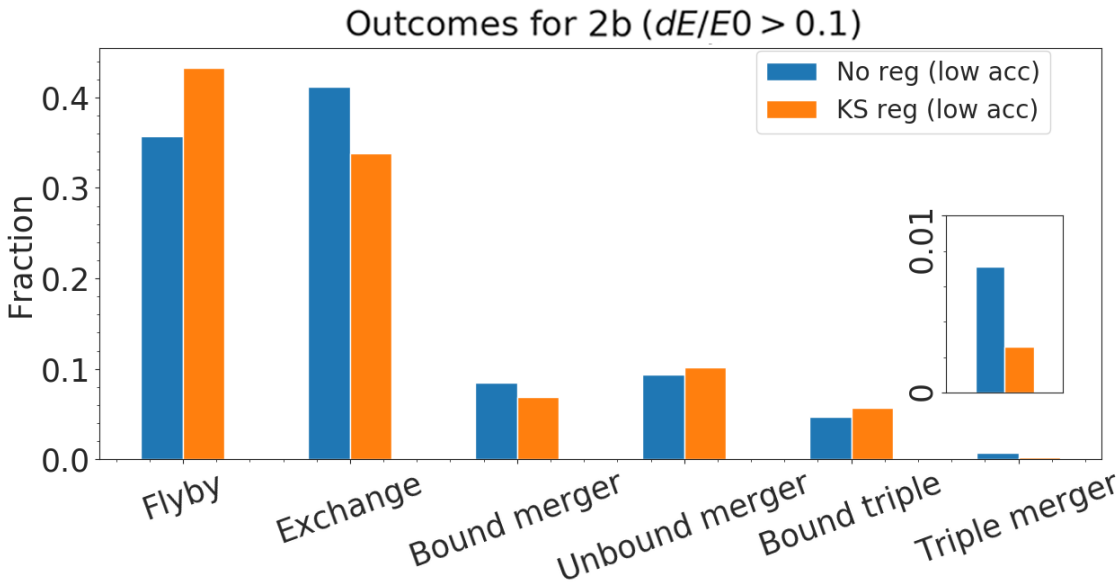

Figure 4.2: Distribution of outcomes for setup 2b where the energy conservation is worse than 10%.

4.2.1 Computation time

Ideally the accuracy setting of an integration would be set to an infinitely high precision but in practice this is not possible since the computation time increases for better accuracy. In figures 4.5 and 4.6 we plot the distribution times for different accuracies from the No regularization run and KS regularization of setup 2a. We see that a higher accuracy leads to, on average, higher computation time as expected. Comparing the low accuracy run with the high accuracy run with no regularization we find that the high accuracy run takes, on average, approximately 14 times longer to solve each interaction while for the KS regularization the high accuracy run takes approximately 11 times longer to solve each interaction. For large data sets this increase in computation time can be problematic and whether the increased accuracy is needed should be considered since according to Portegies Zwart & Boekholt (2014) as long as the energy conservation is better than 10%, the accuracy should not make a difference on a statistical scale.

In figures 4.5 and 4.6 we plot the distribution times for different accuracies from the No regularization run and KS regularization of setup 2b. We see that a higher accuracy leads to, on average, higher computation time as expected. Comparing the low accuracy run with the high accuracy run with no regularization we find that the high accuracy run takes, on average, approximately 9 times longer to solve each interaction while for the KS regularization the high accuracy run takes approximately 7.5 times longer to solve each interaction. For large data sets this increase in computation time can be problematic and whether the increased accuracy is really needed should be considered.

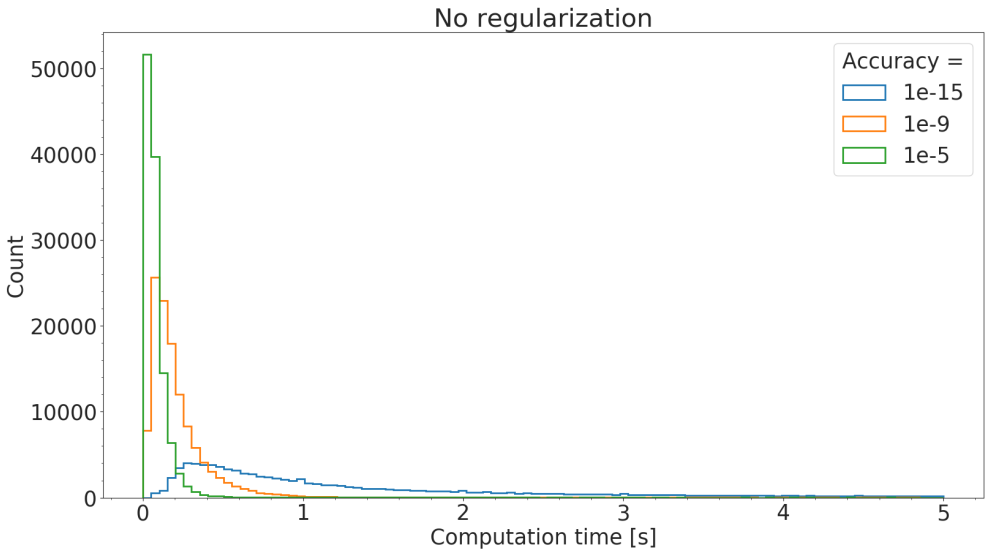

Figure 4.3: Distribution of computation time for different accuracies from the No regularization runs of setup 2a. On average, the high accuracy run takes 14 times longer to compute than the low accuracy run. The computation times go up to 90 seconds (the limit we set in the integrator) but we set a limit on 5 seconds in the plot to show the relevant differences.

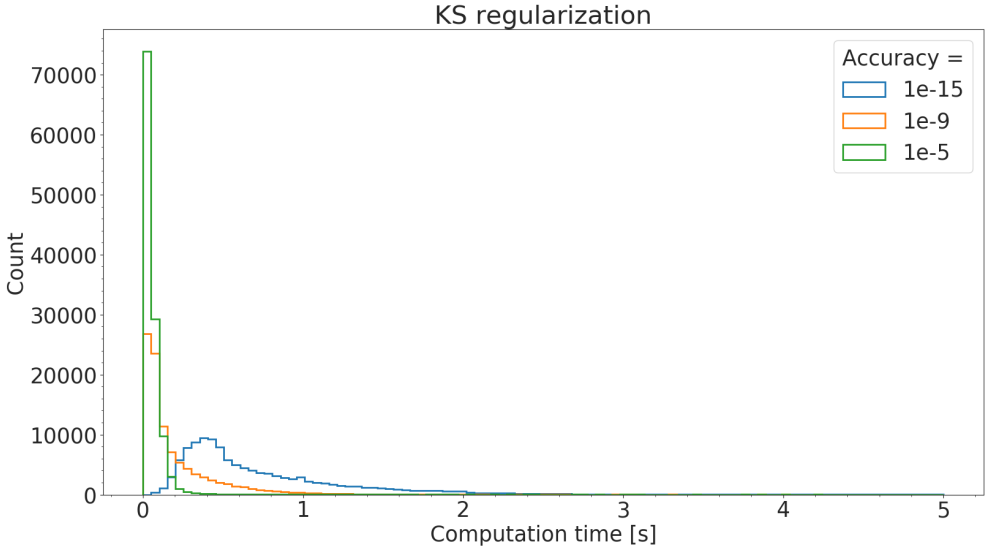

Figure 4.4: Distribution of computation time for different accuracies from the KS regularization runs of setup 2a. On average, the high accuracy run takes 11 times longer to compute than the low accuracy run. The computation times go up to 90 seconds (the limit we set in the integrator) but we set a limit on 5 seconds in the plot to show the relevant differences.

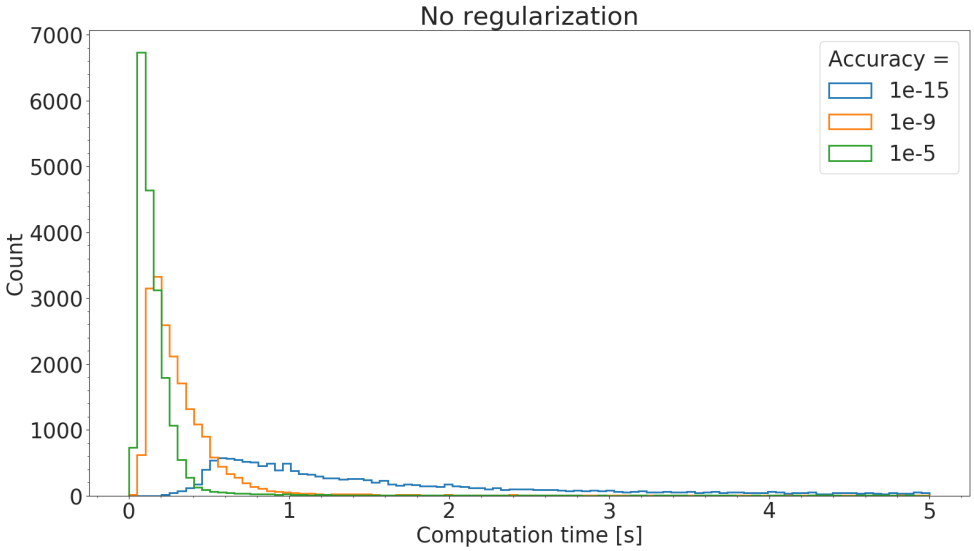

Figure 4.5: Distribution of computation time for different accuracies from the No regularization runs of setup 2b. On average, the high accuracy run takes 9 times longer to compute than the low accuracy run. The computation times go up to 90 seconds (the limit we set in the integrator) but we set a limit on 5 seconds in the plot to show the relevant differences. The number of interactions with $t_{cpu} > 5$s is: 24652 (high accuracy), 356 (default accuracy) and 148 (low accuracy).

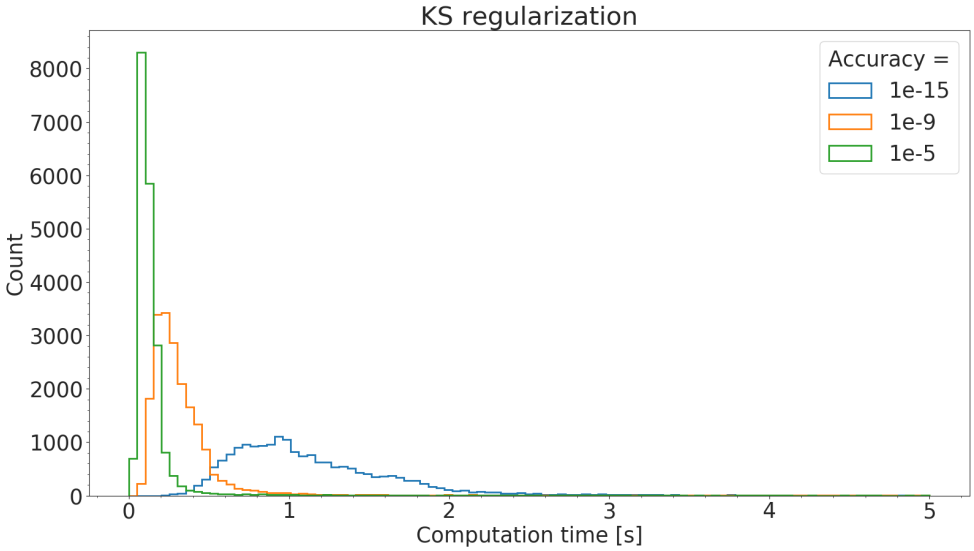

Figure 4.6: Distribution of computation time for different accuracies from the KS regularization runs of setup 2b. On average, the high accuracy run takes 7.5 times longer to compute than the low accuracy run. The computation times go up to 90 seconds (the limit we set in the integrator) but we set a limit on 5 seconds in the plot to show the relevant differences. The number of interactions with $t_{cpu} > 5$s is: 944 (high accuracy), 376 (default accuracy) and 179 (low accuracy).

4.2.2 Physical time

We investigate if changing the accuracy of a run changes the physical time it takes for an interaction to finish. This is shown in figures 4.7 and 4.8 where the two left panels shows the results from the No regularization runs and the right panels shows the results from the KS regularization runs. For the two plots from the 2a run we see a more distinct and sharp peak than for the 2b run. This is explained by the fact that most of the interactions in 2a have a higher initial relative velocity than those in 2b and such we will have more distant flybys. These distant flybys happen quickly and are most likely the cause of this peak. We find that for our runs, the accuracy does not have a significant statistical impact on the physical time of the interactions.

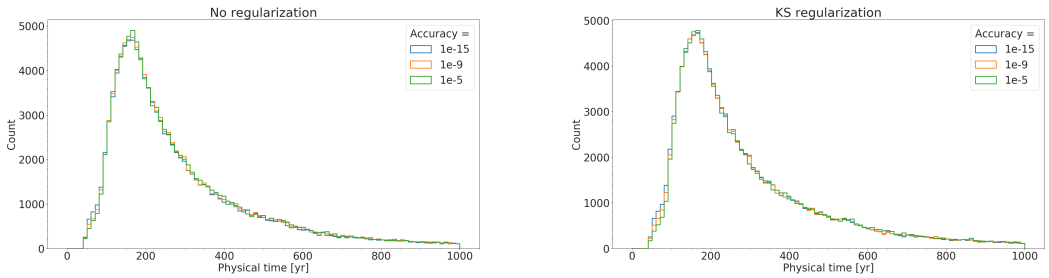

Figure 4.7: Distribution of physical time of the interactions for different accuracies of the No regularization run (left panel) and KS regularization run (right panel) of setup 2a.

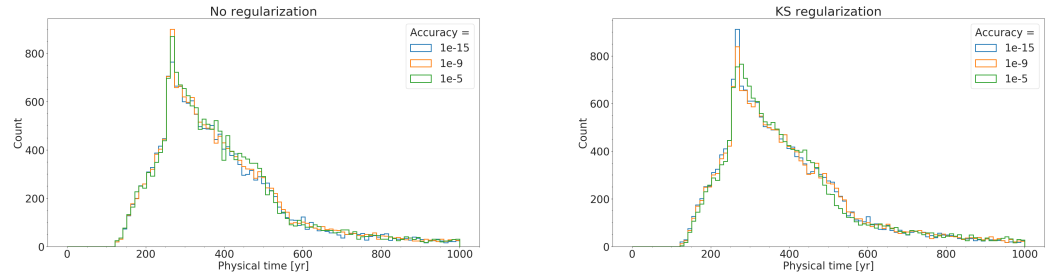

Figure 4.8: Distribution of physical time of the interactions for different accuracies of the No regularization run (left panel) and KS regularization run (right panel) of setup 2b.

4.3 Influence of additional processes

Dynamical interactions occur frequently in dense stellar environments compared to the field. How the interactions and their outcomes may affect the evolution of the environment they occur in can be investigated with simulations but the reliability of these simulations are hard to predict since we cannot compare the simulations to interactions in the real world. A problem with these interactions involves what to include in the integration. For example, if we have a set of binary-single interaction involving only black holes, can we use the Newtonian equation of motion and get correct results or do we need to include additional processes such as PN terms and tidal effects? How PN terms and tides affects the outcomes of binary-single interactions will be discussed here and we will also relate this to gravitational wave detections by detectors such as LIGO and Virgo.

4.3.1 Black hole interactions & PN terms

PN terms primarily affects BHs since they are very compact objects. Rodriguez et al. (2018) finds that the addition of PN terms increase the number of mergers, both during the interaction and

after the interaction due to GW emission. This is not something that we were able to reproduce with our set of interactions. In our runs we found that if we start with an initially eccentric binary we will, on average, circularise the binary following a flyby and increase the time to merge due to GW emission. However, if we start with a lower initial eccentricity we will most likely increase the eccentricity and reduce the merger time. In addition to this, we found that the inclusion of PN terms does not lead to a significant change in the number of mergers compared to the run without PN terms. The numbers for these claims are found in table 3.4 and 3.5.

4.3.2 Role of tides

BHs are not greatly affected by tidal effects since they are small, compact objects that cannot be stretched to like physically extended objects like main sequence or giant stars. We include tides in our 1 BH and 2 BH runs to see if the addition of this process statistically change the interactions. We find that for 1 BH, the addition of tides decreases the number of all merger cases while increasing the number of bound triples when compared to the other runs. The increase in bound triples can be expected since the tidal effects remove energy from the interaction which could allows for the formation of bound triple systems. However, this needs to be checked with more interactions. For the 2 BH case we find that the addition of tides does not significantly change the outcomes. We get slightly less bound mergers and slightly more bound triples. Since black holes are not affected by tidal effects to the same extent as stars are, this is expected since there are less objects in the interaction that are affected by tides.

When we initially included tides we saw a sharp and unexpected increase in the number of ionization outcomes when combining the PN terms with the tides. Upon investigating further we found that the binary dissolves on its own after the interaction takes place. This is very unexpected and nonphysical behaviour and such we made one of the authors of Tsunami aware of this and got an explanation for the behaviour: the way the tides are implemented in the code works in a way that the dissipated energy is dependent on the orbital elements of a pair of particles: the eccentricity and semi-major axis. The problem here is that when including PN terms these terms are not well defined because the energy used to compute them are not corrected for the PN acceleration. This was fixed in a later version of Tsunami and this story is an example that care has to be taken when implementing these effects, especially when they are implemented together with additional effects.

4.3.3 Implication for Gravitational Wave Detection

Gravitational waves (GWs) have been observed from merging compact objects by the LIGO and Virgo detectors. In the future, LISA will also detect GWs but the frequency at which black holes merge and where the gravitational wave sources originate from are still uncertain. Due to gravitational wave radiation every isolated black hole binary will merge eventually, however, we are not interested in black holes that will take more than a Hubble time to merge since we will not be able to detect those any time soon. Therefore, we look at the delay time (t_{delay}) which is age of the cluster when the interaction takes place ($t_{interaction}$) summed together with the merger time due to gravitational wave radiation (t_{GW}) that we can calculate with eq.3.6:

$$t_{delay} = t_{interaction} + t_{GW} \tag{4.1}$$

We are also interested in the chirp mass (Cutler & Flanagan, 1994), which we can calculate with

$$\mathcal{M} = \frac{(m_1 m_2)^{3/5}}{(m_1 + m_2)^{1/5}} \tag{4.2}$$

We use this to plot the delay time against the chirp mass in figure 4.9 for the binary black holes (BBHs) with a delay time lower than a Hubble time. Here we assume that the binary-single

encounter will eject the BBH from the cluster and it will evolve as an isolated binary following the ejection. We also show the distribution of delay time in figure 4.10, where we can see that for both runs, we have a peak at low delay time and a flat distribution from 6000 Myr up to a Hubble time which indicates that these BBHs could potentially be detected by GW detectors such as LIGO and Virgo.

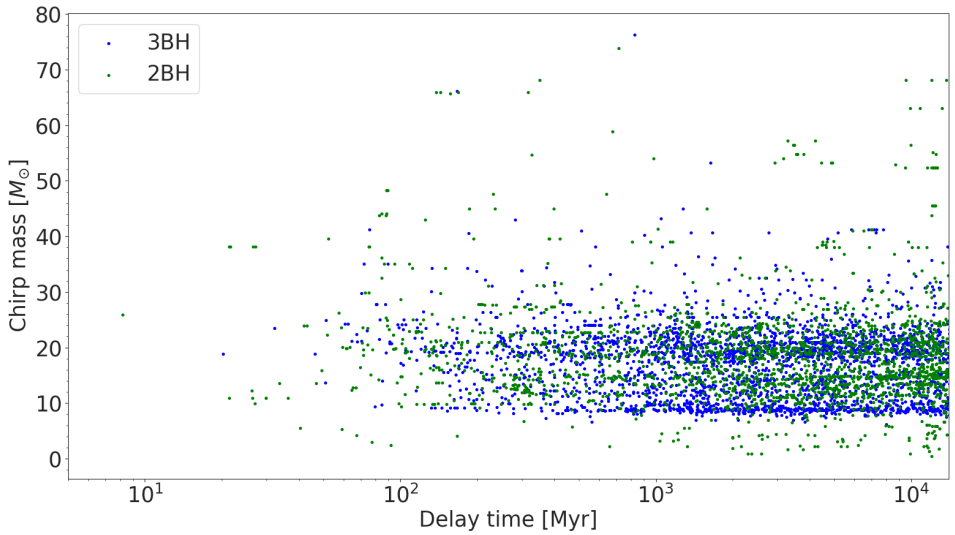

Figure 4.9: Interaction time plotted against chirp mass for all black hole binaries that merges within a Hubble time after the interaction from the 3 BH (blue dots) and 2 BH (green dots) data set. We find 2926 BBHs with a delay time less than for Hubble time for the 3 BH set and 2622 BBHs for the 2 BH set.

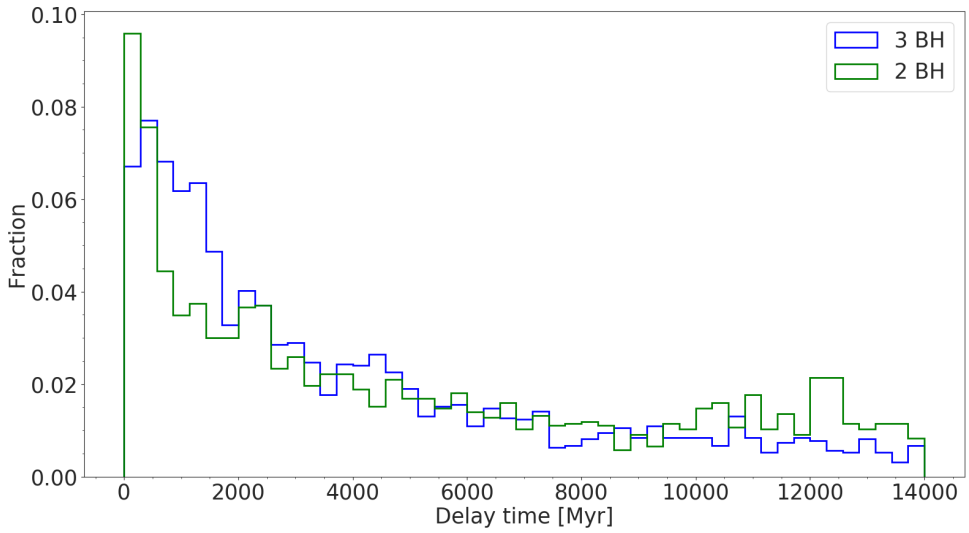

Figure 4.10: Distribution of delay time for black hole binaries that merge within a Hubble time from when the globular cluster formed. We find 2926 BBHs with a delay time less than a Hubble time for the 3 BH set and 2622 BBHs for the 2 BH set.

We investigate the mass ratio between the primary black hole (the black hole with highest mass in the binary) and the secondary black hole and show this as a scatter plot in figure 4.11 for our binaries obtained in the 2 and 3 BH set with a delay time lower than a Hubble time. We also include the primary and secondary black hole masses of 11 LIGO and Virgo detections in our scatter plot as red dots (data taken from Abbot et al. (2019, 2020)). We find that the LIGO and Virgo detections line up quite well with the merging BBHs that we find from our interactions even though this was only a small subsample of binary-single interactions involving 2 or more black holes that were taken from the MOCCA-Survey Database I results.

Nearly all of these simulated interactions came from MOCCA-Survey Database I models in which black hole natal kicks had been reduced due to the mass fallback prescription of (Belczynski et al., 2002) resulting in a higher retention of black holes. The masses of the black holes in the simulations depend on stellar evolution prescriptions for evolution of black hole progenitors (Hurley et al., 2000). The maximum mass of a black hole produced in these simulations through the evolution of a single massive star is about 30 $M_{\odot}$. In figure 4.11, there are few black holes which are more massive than this value. In these cases, the black hole progenitors were initially in binary systems where binary evolution can have an influence on the final black hole mass or these black holes grew in mass by merging with other stars and black holes. Nevertheless, these results show that dynamical interactions within stellar clusters can produce merging BBHs with different mass ratios.

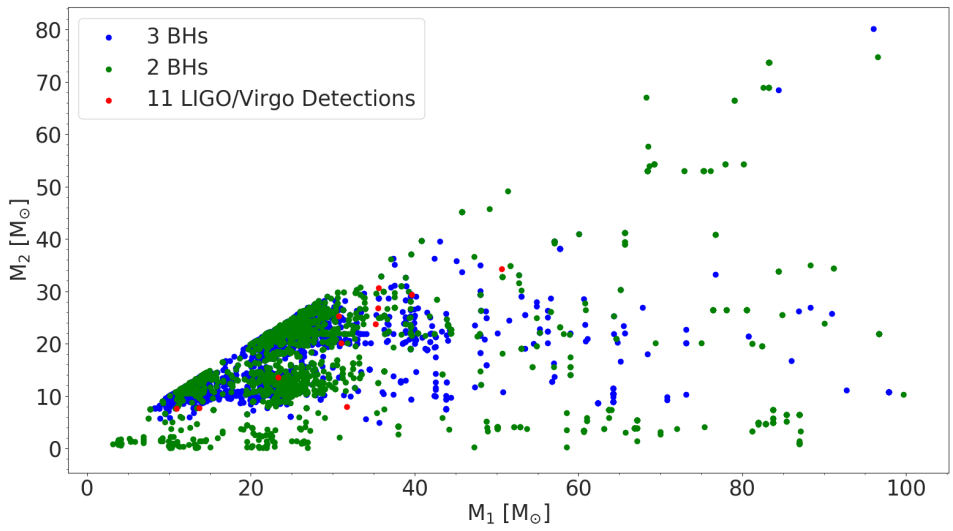

Figure 4.11: Primary against secondary masses for black holes that merge within a Hubble time for the 3 BH set (blue dots) and 2 BH set (green dots). Also included are the primary and secondary masses that LIGO and Virgo has measured from gravitational waves as red dots. We find 2926 BBHs with a delay time less than for Hubble time for the 3 BH set and 2622 BBHS for the 2 BH set.

4.3.3.1 Eccentric BH mergers

Interactions between a binary and a single may increase the eccentricity of the binary to the point where the objects merge during the interaction (Samsing, 2018; Samsing et al., 2014, 2018a). We present an example of such an interaction here from our 3 BH set with the parameters: mass of the single $m_0 = 22.04$ $M_\odot$, mass of the binary components $m_{11} = 21.27$ $M_\odot$ and $m_{12} = 18.53$ $M_\odot$. The initial binary parameters are: semi-major axis $a = 0.72$ AU and $e = 0.899$ and the interaction parameters are $v_\infty = 0.048 v_c$ and $b = 34.06$ AU. When the objects come close they form a temporary triple system with multiple exchanges such that the components of the inner binary changes over time. At the end of the interaction a binary with the initial binary components form with eccentricity 0.971, over 0.5 years this eccentricity increases up to $e = 0.999999$ before the two initial binary components merge. The trajectory of this interaction is shown in figure 3.4.

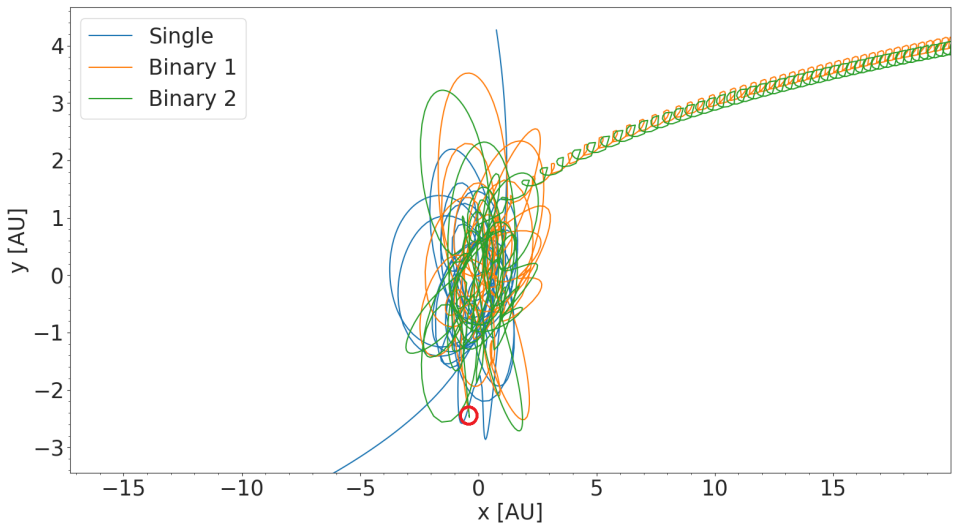

Figure 4.12: Trajectory of bound merger in 3 BH set. The red circle shows the point at which the two black holes merge.

4.3.4 Bound triples without PN/tides

The formation of bound triple systems can be formed from binary-single interactions if there is some process to remove energy from the interaction, such as GW emissions from PN terms or tidal effects. However, we see bound triples without these processes. This might be due to the way the integrator terminates the calculation. A few of the bound triples we investigated were all very weakly bound and the close passages between the inner binary and the outer object occurs every $> 10^5$ years. Within a globular cluster this triple will most likely be broken up by interactions with other objects before the next close passage. We investigated the triple mergers that we find in our 2 BH set and find 3 triple mergers where the 2 black holes merge followed by the resulting black hole merging with the star. This might lead to a merger that could be detected by gravitational waves followed by a luminous transient or a tidal disruption event (Samsing et al., 2019; Fragione et al., 2019). However, these outcomes are rare in our runs and require further investigation.

Chapter 5

Conclusions

In this study, we systematically carried out a large number of numerical binary-single scattering experiments for different initial setups with different regularization schemes, additional processes and changes in the numerical accuracy of the integrator in order to statistically compare the differences in the results. In order to do this, we use the N-body codes Fewbody by Fregeau et al. (2004) and Tsunami by Trani et al. (2016). We create our own set of initial conditions for interactions involving solar-like stars and extract data from the MOCCA Survey Database I where the interactions involve at least one black hole. These sets are simulated with different regularization methods and the inclusion of additional processes.

Binary-single interactions are astrophysically important since they can support a globular cluster against core collapse, form exotic objects and may be a formation channel for gravitational wave source. However, it is not possible to solve these three-body encounters analytically and the interactions are very chaotic, i.e a small change in initial parameters may lead to a large difference in the outcome of the interaction. Because of this we need to use numerical integrators to solve these kinds of interactions. The main findings of this study are:

- For the runs involving 3 stars we find that the KS regularization slightly reduces the number of mergers while increasing the number of exchanges. The reason for this is explained in Fregeau et al. (2004) to be that the KS regularization requires extra effort to find mergers and this is not implemented in their current code.
- For the run with 1 BH we find that the ARChain differs from the other regularization methods by reducing the number of all merger cases while increasing the number of temporarily bound triples.
- For 2 and 3 BHs we find that the choice of regularization method does not make a significant difference to the statistical distribution of outcomes.
- We find that increasing or decreasing the accuracy setting of the interaction do change the statistical distribution of outcomes, even when all interactions with energy conservation worse than 10% are removed. Typically it is estimated that as long as the energy conservation is better than 10%, the outcome of interactions should not make a difference on a statistical scale (Portegies Zwart & Boekholt, 2014). Our runs seems to indicate that a energy conservation better than 10% is required for making the accuracy irrelevant.
- Our runs indicates that the KS regularization is more affected by the choice of accuracy than when no regularization is used. We also find that decreasing the accuracy affects the results more than increasing it.

- For the interactions involving black holes, we find that the inclusion of post-Newtonian terms does not significantly increase the number of mergers between black holes. This includes both mergers during the interaction and the formation of binaries that merge due to gravitational wave radiation within a Hubble time. We also find that if an interaction will, on average, decrease or increase the merger time due to gravitational wave radiation depends on the initial parameters of the binary and the interaction.
- The inclusion of tidal effects reduces the number of mergers and increases the number of bound triples. This is seen in both the 1 BH and 2 BH run, however, it is most notable when we have 1 black hole and 2 stars in the interaction since stars are more affected by tides.
- We compared the masses and mass ratio distribution for merging binary black holes from our runs with the 11 binary black hole mergers detected so far by the LIGO/Virgo detectors. We find that the mass ratio distribution of our merging black hole binaries agrees well with the observed values. These results indicate that such gravitational wave sources can potentially form due to the binary-single encounters in dense environments.

Bibliography

Aarseth, S. J. 1971, Ap&SS, 13, 324

Abbot, B. P. et al. 2019, Physical Review X, 9, 031040

Abbot, B. P. et al. 2020, arXiv e-prints, arXiv:2004.08342

Abbott, B. P., Abbott, R., Abbott, T. D., et al. 2016a, Phys. Rev. Lett., 116, 061102

Abbott, B. P., Abbott, R., Abbott, T. D., et al. 2016b, Phys. Rev. Lett., 116, 131102

Abbott, B. P., Abbott, R., Abbott, T. D., et al. 2019, Physical Review X, 9, 031040

Adams, S. M., Kochanek, C. S., Gerke, J. R., Stanek, K. Z., & Dai, X. 2017, MNRAS, 468, 4968

Aharon, D. & Perets, H. B. 2015, The Astrophysical Journal, 799, 185

Amaro-Seoane, P., Aoudia, S., Babak, S., et al. 2013, GW Notes, 6, 4

Antonini, F. 2013, The Astrophysical Journal, 763, 62

Antonini, F., Capuzzo-Dolcetta, R., Mastrobuono-Battisti, A., & Merritt, D. 2012, The Astrophysical Journal, 750, 111

Arca Sedda, M., Askar, A., & Giersz, M. 2018, MNRAS, 479, 4652

Askar, A., Arca Sedda, M., & Giersz, M. 2018, MNRAS, 478, 1844

Askar, A., Szkudlarek, M., Gondek-Rosińska, D., Giersz, M., & Bulik, T. 2017, MNRAS, 464, L36

Belczynski, K., Heger, A., Gladysz, W., et al. 2016, A&A, 594, A97

Belczynski, K., Kalogera, V., & Bulik, T. 2002, ApJ, 572, 407

Benacquista, M. 2013, Dynamical Evolution of Binaries (New York, NY: Springer New York), 213–221

Benacquista, M. J. & Downing, J. M. B. 2013, Living Reviews in Relativity, 16, 4

Binney, J. & Tremaine, S. 1987, Galactic dynamics (Princeton University Press)

Blanchet, L. 2014, Living Reviews in Relativity, 17, 2

Boekholt, T. & Portegies Zwart, S. 2014, On the Reliability of N-body Simulations

Boekholt, T. C. N., Portegies Zwart, S. F., & Valtonen, M. 2020, MNRAS, 493, 3932

Breen, P. G. & Heggie, D. C. 2013a, MNRAS, 432, 2779

Breen, P. G. & Heggie, D. C. 2013b, MNRAS, 436, 584

Chaisson, E. & McMillan, S. (Stephen), . 2011, Astronomy today, 7th edn. (Boston Addison-Wesley), includes bibliographical references and index

Chan, C., Müller, B., Heger, A., Pakmor, R., & Springel, V. 2018, ApJ, 852, L19

Cordes, J. M., Romani, R. W., & Lundgren, S. C. 1993, Nature, 362, 133

Cutler, C. & Flanagan, É. E. 1994, Phys. Rev. D, 49, 2658

Davies, M. B. 2002, in Astronomical Society of the Pacific Conference Series, Vol. 265, Omega Centauri, A Unique Window into Astrophysics, ed. F. van Leeuwen, J. D. Hughes, & G. Piotto, 215

Davies, M. B. 2013, Globular Cluster Dynamical Evolution, Vol. 5 (Springer, Dordrecht), 879

Di Carlo, U. N., Giacobbo, N., Mapelli, M., et al. 2019, MNRAS, 487, 2947

Djorgovski, G. 2004, Star Clusters and Stellar Dynamics, URL: http://www.astro.caltech.edu/~george/ay20/Ay20-Lec15x.pdf

Downing, J. M. B., Benacquista, M. J., Giersz, M., & Spurzem, R. 2010, MNRAS, 407, 1946

Fackerell, E. D. 1968, ApJ, 153, 643

Faucher-Giguere, C.-A. & Kaspi, V. M. 2006, Astrophys. J., 643, 332

Fragione, G., Leigh, N. W. C., Perna, R., & Kocsis, B. 2019, MNRAS, 489, 727

Fregeau, J. M., Cheung, P., Portegies Zwart, S. F., & Rasio, F. A. 2004, MNRAS, 352, 1

Fryer, C. L. 1999, ApJ, 522, 413

Fryer, C. L., Belczynski, K., Wiktorowicz, G., et al. 2012, ApJ, 749, 91

Geller, A. M., Leigh, N. W. C., Giersz, M., Kremer, K., & Rasio, F. A. 2019, ApJ, 872, 165

Giersz, M. 1985, Acta Astron., 35, 401

Giersz, M., Heggie, D. C., Hurley, J. R., & Hypki, A. 2013, MNRAS, 431, 2184

Giesers, B., Dreizler, S., Husser, T.-O., et al. 2018, Monthly Notices of the Royal Astronomical Society: Letters, 475, L15

Hansen, B. M. S. & Phinney, E. S. 1997, MNRAS, 291, 569

Harris, W. E. 1996, AJ, 112, 1487

Heggie, D. & Hut, P. 2003, The Gravitational Million–Body Problem: A Multidisciplinary Approach to Star Cluster Dynamics (Cambridge University Press)

Heggie, D. C. 1974, Celestial Mechanics, 10, 217

Heggie, D. C. 1975, MNRAS, 173, 729

Hénon, M. 1971a, Ap&SS, 13, 284

Hénon, M. H. 1971b, Ap&SS, 14, 151

Hills, J. G. 1975, AJ, 80, 809

Hobbs, G., Lorimer, D. R., Lyne, A. G., & Kramer, M. 2005, MNRAS, 360, 974

Hong, J., Vesperini, E., Askar, A., et al. 2018, MNRAS, 480, 5645

Hurley, J. R., Pols, O. R., & Tout, C. A. 2000, MNRAS, 315, 543

Hut, P. & Bahcall, J. N. 1983, ApJ, 268, 319

Hypki, A. & Giersz, M. 2013, MNRAS, 429, 1221

Janka, H.-T. 2013, MNRAS, 434, 1355

Janka, H.-T. 2017, ApJ, 837, 84

Jeans, J. H. 1919, MNRAS, 79, 408

Krauss, L. M. & Chaboyer, B. 2003, Science, 299, 65

Kremer, K., Chatterjee, S., Ye, C. S., Rodriguez, C. L., & Rasio, F. A. 2019, ApJ, 871, 38

Kulkarni, S. R., Hut, P., & McMillan, S. 1993, Nature, 364, 421

Kustaanheimo, P. & Stiefel, E. 1965, J. Reine Angew. Math., 218, 204

Kutta, W. 1901, Beitrag zur näherungsweisen Integration totaler Differentialgleichungen (Teubner)

Lamers, H. J. G. L. M., Baumgardt, H., & Gieles, M. 2010, MNRAS, 409, 305

Lee, H. M. & Ostriker, J. P. 1993, ApJ, 409, 617

Lombardi, J. C., Thrall, A. P., Deneva, J. S., Fleming, S. W., & Grabowski, P. E. 2003, MNRAS, 345, 762

Loose, H. H., Kruegel, E., & Tutukov, A. 1982, A&A, 105, 342

Mapelli, M. 2017a, Binaries and 3-body Encounters, URL: `http://web.pd.astro.it/mapelli/2017dynamics3.pdf`

Mapelli, M. 2017b, Regularization, URL: `http://web.pd.astro.it/mapelli/2017dynamics6.pdf`

Mapelli, M. 2017c, Regularization, URL: `http://web.pd.astro.it/mapelli/Regularization.pdf`

Merritt, D. 1996, The Astronomical Journal, 111, 2462

Mikkola, S. 2008, Regular Algorithms for the Few-Body Problem (Dordrecht: Springer Netherlands), 31–58

Mikkola, S. & Aarseth, S. J. 1993, Celestial Mechanics and Dynamical Astronomy, 57, 439

Mikkola, S. & Tanikawa, K. 1999, Monthly Notices of the Royal Astronomical Society, 310, 745

Morscher, M., Umbreit, S., Farr, W. M., & Rasio, F. A. 2013, ApJ, 763, L15

Neumayer, N., Seth, A., & Boeker, T. 2020, arXiv e-prints, arXiv:2001.03626

Pattabiraman, B., Umbreit, S., Liao, W.-k., et al. 2013, ApJS, 204, 15

Perets, H. B., Li, Z., Lombardi, J. C., & Milcarek, S. R. 2016, The Astrophysical Journal, 823, 113

Peters, P. C. 1964, Phys. Rev., 136, B1224

Pooley, D. 2010, Proceedings of the National Academy of Sciences, 107, 7164

Portegies Zwart, S. & Boekholt, T. 2014, The Astrophysical Journal, 785, L3

Portegies Zwart, S. F. & McMillan, S. L. W. 2000, ApJ, 528, L17

Portegies Zwart, S. F. & Meinen, A. T. 1993, A&A, 280, 174

Press, W. H. & Teukolsky, S. A. 1977, ApJ, 213, 183

Ransom, S. M. 2008, in IAU Symposium, Vol. 246, Dynamical Evolution of Dense Stellar Systems, ed. E. Vesperini, M. Giersz, & A. Sills, 291–300

Rasskazov, A. & Merritt, D. 2017, ApJ, 837, 135

Repetto, S., Davies, M. B., & Sigurdsson, S. 2012, MNRAS, 425, 2799

Rodriguez, C. L., Amaro-Seoane, P., Chatterjee, S., et al. 2018, Phys. Rev. D, 98, 123005

Rodriguez, C. L., Chatterjee, S., & Rasio, F. A. 2016, Phys. Rev. D, 93, 084029

Runge, C. 1895, Mathematische Annalen, 46, 167

Saha, P. 2009, Monthly Notices of the Royal Astronomical Society, 400, 228–231

Samsing, J. 2018, Phys. Rev. D, 97, 103014

Samsing, J., Askar, A., & Giersz, M. 2018a, ApJ, 855, 124

Samsing, J., D'Orazio, D. J., Askar, A., & Giersz, M. 2018b, arXiv e-prints, arXiv:1802.08654

Samsing, J., Leigh, N. W. C., & Trani, A. A. 2018, Monthly Notices of the Royal Astronomical Society, 481, 5436–5444

Samsing, J., MacLeod, M., & Ramirez-Ruiz, E. 2014, ApJ, 784, 71

Samsing, J., Venumadhav, T., Dai, L., et al. 2019, Phys. Rev. D, 100, 043009

Schödel, R., Merritt, D., & Eckart, A. 2008, in Journal of Physics Conference Series, Vol. 131, Journal of Physics Conference Series, 012044

Schödel, R., Merritt, D., & Eckart, A. 2009, A&A, 502, 91

Sesana, A. 2016, Phys. Rev. Lett., 116, 231102

Sesana, A., Lamberts, A., & Petiteau, A. 2019, arXiv e-prints, arXiv:1912.07627

Shahzamanian, B., Schödel, R., Nogueras-Lara, F., et al. 2019, arXiv e-prints, arXiv:1910.07940

Sigurdsson, S. & Hernquist, L. 1993, Nature, 364, 423

Spitzer, L. 1987, Dynamical evolution of globular clusters (Princeton, N.J. : Princeton University Press)

Spitzer, L. S. 1987, Dynamical Evolution of Globular Clusters (Princeton University Press)

Spurzem, R. 2007, Relativistic Dynamics and Gravitational Waves from Dense Stellar Systems, URL: https://astro.uni-bonn.de/~modest8/talks/modest8_spurzem.pdf

Strader, J., Chomiuk, L., Maccarone, T. J., Miller-Jones, J. C. A., & Seth, A. C. 2012, Nature, 490, 71

Trani, A., Mapelli, M., Spera, M., & Bressan, A. 2016, Dynamics of tidally captured planets in the Galactic Center

Trani, A. A., Fujii, M. S., & Spera, M. 2019, ApJ, 875, 42

Tremaine, S. D., Ostriker, J. P., & Spitzer, L., J. 1975, ApJ, 196, 407

Vinkó, J., Yuan, F., Quimby, R. M., et al. 2014, The Astrophysical Journal, 798, 12

Wang, L., Spurzem, R., Aarseth, S., et al. 2016, MNRAS, 458, 1450

Wongwathanarat, A., Janka, H. T., & Müller, E. 2013, A&A, 552, A126

Yoshida, H. 1990, Physics Letters A, 150, 262